Radar Micro-Doppler Patterns for Drone's Characterisation

Yefeng Cai
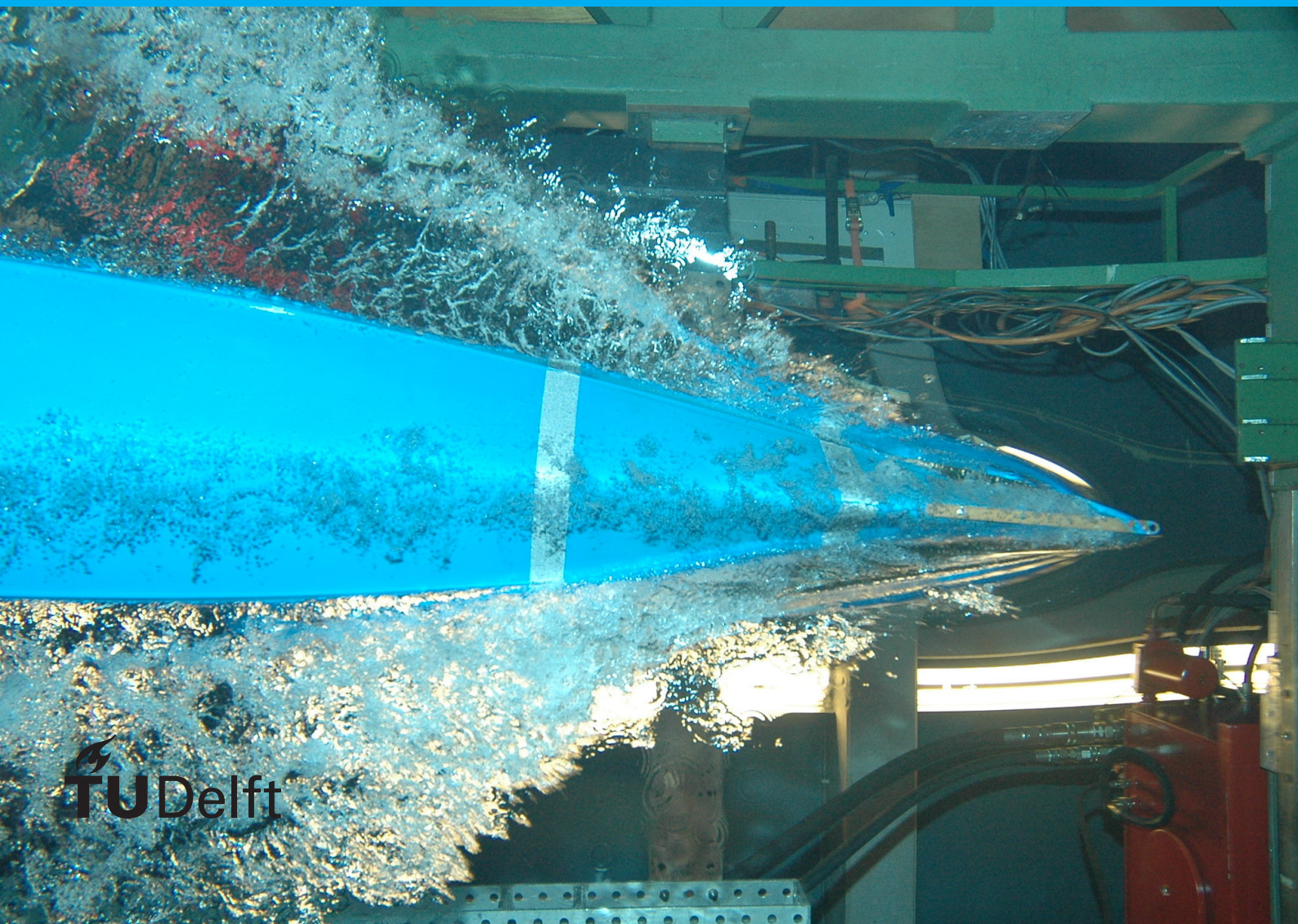
Radar Micro-Doppler Patterns for Drone's Characterisation

by

Yefeng Cai

to obtain the degree of Master of Science

at the Delft University of Technology,

to be defended publicly on Wednesday May 29, 2019 at 11:00 AM.

An electronic version of this thesis is available at `http://repository.tudelft.nl/`.

TUDelft

Abstract

Micro-Doppler patterns of multi-propeller drones measured by radar systems are widely used in the classification of different drones, since the micro-Doppler patterns illustrate the velocity and motion properties of the drones. However, on this topic, there are a few issues the current researches have not tackled yet. First of them is the the lack of mathematical description of the micro-Doppler patterns. and most research works are based on real measured data so far. As a result, features are proposed to characterise the micro-Doppler patterns for each individual measured data set without a general guideline. Second, most current researches focus on the micro-Doppler patterns achieved in short CPI cases that are valid for radar systems with PRI much shorter than the rotation period of the drone's propellers. As a result, some existing radar systems with long PRI do not benefit from the research outcome and stay excluded from micro-Doppler-based drone classification tasks. Third, most researches at present are carried out in short range for static or stable hovering drones. From a practical point of view, it is also of great interest to investigate the drone micro-Doppler patterns in long range and dynamic scenarios.

In this thesis, an EM backscattering model in HH plane of drone propeller is developed, simplifying the propeller's geometry structure as a few cylinder thin wires. Radar signal model and micro-Doppler model are subsequently developed for the thin-wire propeller model when it is rotating. The thin-wire model-based backscattered signal and micro-Doppler pattern are validated by measurements in anechoic chamber and simulations in software at X-band and S-band. These models are expanded to multi-propeller drones and validated with measurements of drones in the open air by real radar systems. This gives a possibility to describe the drone micro-Doppler pattern mathematically as a function of a few variables corresponding to drone properties and radar setups.

The drone micro-Doppler patterns in long CPI circumstances are investigated. The drone micro-Doppler spectrum simulated from the thin-wire in this circumstance is the combination of a few harmonic components. For given radar setup parameters, the amplitude of the harmonic components and the frequency difference between neighbouring harmonic components are influenced by the geometry structure of the propeller and the drone, the rotation period of the propeller and the synchronisation of propellers. Features are proposed to characterise the amplitude and frequency distribution of the harmonic components in the simulated micro-Doppler spectrum. The proposed features well characterise the micro-Doppler spectrum simulated from the thin-wire model, and applying these features to SVM gives good classification accuracy for the simulated micro-Doppler data. This gives a possible solution of general feature selection schemes to characterise drone micro-Doppler patterns in long CPI circumstance.

The micro-Doppler patterns of different drones at a distance of 9 kilometres are achieved by S-band radar in long CPI circumstance. Applying the proposed features to the real data of micro-Doppler spectra to SVM

gives good classification accuracy for drones in hovering and manoeuvring flight modes. The application to real data reconfirms the thin-wire simplification model and the characteristic feature proposal scheme. This shows the feasibility to perform further micro-Doppler investigation in long CPI, km-level range and dynamic flight mode circumstances.

Acknowledgements

I would like to give my gratitude to my thesis supervisor, Dr. Oleg Krasnov. During the time of my thesis work, he supported me very much in carrying out the project. He was always patiently offering me informative hints in each phase of the project, whenever I got confused on any issue. His intuitive explanation and small handy models saved me more than once from struggling to tackle the problems. Even when he was recovering from the heart attack, he still cared about my project progress and gave me many suggestions when we met up. Apart from the technical aspect in my thesis work, he also helped me very much to improve relevant academic skills. For so many times he had spent hours and days editing my writing draft, teaching me to write in the appropriate way and to make clear illustrations. I feel very grateful for his help and guidance that will be continuously valuable in my future career.

I also would like to give my gratitude to my thesis supervisor, Prof. Alexander Yarovoy. During my study and thesis work within the Group of Microwave Sensing, Signals and System, he was always encouraging me and ready to offer support. Every time meeting with him, I would get inspired by him in both the academic expertise and research philosophy aspects. I learnt much from him about making clear and practical research schemes, making deep analysis on research results, delivering self-contained presentations and so on. Since I had problems failing to follow up with study just before starting my thesis project, it is his enthusiastic attitude that has been encouraging me all the way along till today – If there is a problem, it is better to face the problem than to hide it. This comment by him will always encourage me to solve problems in future.

Moreover, I would like to thank Mr. Pascal Aubry and Mr. Fred van der Zwan for their support in the experimental measurements in my thesis project. I would have not collected data of high quality without their experience and help in anechoic chamber measurement, radar system operation and drone flight.

Besides, I would like to thank many people within Group MS3 and from external; Specifically, to Dr. David Tax, Dr. Jianping Wang, PhD student Mr. Shengzhi Xu and PhD student Mr. Nikita Petrov for their generous help and valuable suggestions in my work.

Last but not least, I would like to give many thanks to my family and friends, especially to my parents, for their consistent encouragement, understanding and support during all these years, which I could not have finished my study without.

Yefeng Cai
Delft, May 2019

Contents

Glossary

3D 3-dimension. 56–58, 64

ADC analogue-to-digital converter. 63

CNN convolutional neural network. 11

CPI Coherent Processing Interval. xiv, 2, 4–6, 21, 24, 25, 33–40, 43, 45–49, 59, 60, 63–67, 71, 73, 75

DFT Discrete Fourier Transform. 33, 36, 43

DUCAT Delft University chamber for antenna tests. 14, 19, 21, 36, 38

EM electromagnetic. 4, 8, 9, 11, 13–15, 17–19, 26–30, 32, 37, 40, 44, 71, 73, 74

FEM finite element method. 18

FFT fast Fourier transform. 16, 58

FMCW frequency modulated continuous wave. 22, 61

FPGA field-programmable gate array. 22

GPU graphics processing unit. 22

HH horizontal-horizontal. 22, 73, 74

HV horizontal-vertical. 22

IFFT Inverse fast Fourier transform. 16

LOS line of sight. xiii, 1, 9, 13, 16–18, 25, 28–30, 37, 39, 53, 62, 63, 66, 74

MSE mean squared error. 66

PARSAX polarimetric agile radar in S- and X- band. 60, 61, 63, 71, 75

PCA principal component analysis. 10, 11, 55–58, 60

PDF probability density function. 66, 67, 75

PRF pulse repetition frequency. xiv, 4–6, 21, 23, 24, 28, 35, 37, 39, 44–49, 55, 59–61

PRI pulse repetition interval. 44, 63, 64, 75

RCS radar cross section. viii, xiii, 6, 13–19, 21, 25, 26, 36, 37, 39, 40

RF radio frequency. 14

SNR signal to noise ratio. 2, 5, 9

STFT short-time Fourier transform. 4, 9, 11, 13, 21, 24, 27, 32, 37, 39, 40, 50

SVD singular value decompostion. 10, 55

SVM support vector machine. 10, 11, 58–60, 63, 69, 74, 75

VH vertical-horizontal. 22

VNA vector network analyser. 14, 21

VV vertical-vertical. 22

List of Figures

List of Tables

1

Introduction

1.1. Motivation and Goals

In the last few years, the usage of multi-propeller drones, due to its advantage in low price and easy operation, has increased dramatically in many domains, such as aerial photography, land mapping, logistic, disaster rescue, etc. The growing number of drones and their improper deployment raise concerns of risk in flight safety, air security and privacy issues. Drones of different number of propellers, size and load capacity, introduce threat of different levels in various domains. To evaluate and eliminate the threat, given a drone appearing in the area of interest, identification, tracking and prediction are necessary. All these operations rely on the recognition and classification of the model type of the drone, so drone recognition and classification is of great importance.

Radar micro-Doppler analysis is widely used in drone recognition and classification[12]. Doppler frequency shift is introduced by the displacement of target relative to the observation point, thus illustrates the target's motion. As Mark Richards et al. introduced in [26], "If a radar and scatterer are not at rest with respect to one another, the frequency, f_r, of the received echo will differ from the transmitted frequency, f, due to the Doppler effect". By applying Fourier transform to a series of complex value signals in time domain, the spectra of the signal series can be represented in frequency domain. In the spectra, the radial motion or radial velocity of the target object reflecting the signal along the line of sight (LOS) introduces Doppler shift, a frequency component shifting away from zero frequency. Apart from the Doppler shift corresponding to the radial motion and velocity of the target object as a whole body, rotation around a centre in a specific distance from the observation point and its angular velocity introduce further micro-Doppler frequency patterns. For a flying multi-propeller drone, its propellers, the rotation part, introduce micro-Doppler patterns. These micro-Doppler components contains much information about the model type of the drone, such as

the number of propeller in the drone, the number of blades in each propeller, the length of the blade, and angular velocity of the propeller, the synchronisation of the propellers, etc. Making an analysis on these radar micro-Doppler data is a natural choice to perform drone recognition or classification.

Collecting the micro-Doppler data for different drones with various measurement setups is necessary and offers materials for the following analysis. Traditionally, the data collection is performed by either experimental measurements or software simulations. Experimental measurements of drones flying in the open air are objects dependent. In each measurement, the result data is determined by the model type of the specific drone target, radar setups and signal processing schemes. Measuring micro-Doppler data of different drones and different setup parameters is impractical. Besides, good SNR of the measured data is not always available, requiring extra efforts extracting clear micro-Doppler patterns before making an analysis of these patterns. Software simulations are flexible and able to take various parameters of drones and radars. But software simulations are heavily time and computation consuming, especially simulating multi-propeller drones of complex geometry design and relative motion of different parts in the drone. So developing a method of flexibility and efficiency to collect the micro-Doppler data for different drones with various measurement setups is desirable.

Investigating the micro-Doppler patterns of multi-propeller drones reveals the influence on the final micro-Doppler patterns of the factors of drone properties, radar setups and signal processing schemes. Nowadays, drone recognition and classification based on its micro-Doppler pattern are most performed by deep learning techniques, for patterns in short coherent processing interval (CPI) circumstances. Within a short period of CPI, the velocity of the drone propeller is assumed to be constant corresponding to a frequency shift component in spectra domain, while over several CPIs, the velocity of the propeller may change. Based on this assumption, using a CPI much shorter than the drone propeller rotation period, the propeller radial velocity at each time point corresponding to a single CPI is clearly recorded, forming a sinusoidal pattern over time. Deep learning methods take such periodic drone micro-Doppler patterns as images, thus include much redundancy in terms of the complex algorithm structure and large quantity of parameters. Deep learning methods extract abstract features of the image data automatically, and so the physical meaning of each processing step and the final results is unclear. However, in the original micro-Doppler images, the patterns have specific physical meaning and directly reflect the parameters and variables of drone and radar, and thus can be used to perform drone recognition and classification. So the understanding of the influence gives the possibility to extract a few features characterising the micro-Doppler patterns and reflecting the drone and radar factors, based on which drone recognition and classification can be performed without bothering resource-consuming algorithms.

Overall, the goals of this study are to generate micro-Doppler patterns of multi-propeller drones in an efficient and flexible way, to investigate the influence of drone and radar parameters on these patterns and to propose suitable features characterising the patterns.

1.2. Problem Definition

There are several problems to discuss in drone classification based on micro-Doppler patterns[23]. In this work, three main problems are investigated, a) the lack of a method to collect drone micro-Doppler data for different drones in various scenarios, b) the proposal of meaningful features to characterise the drone micro-Doppler pattern, c) the application of drone classification algorithms in non-ideal scenarios. These problems are defined and described in following subsections.

1.2.1. Drones and Flight Attitudes

There are types of multi-rotor drones in terms of different numbers of propellers, such as helicopter, quadcopter and so on. Quadcopters, hexacopters and octocopters are the most common multi-rotor drones on commercial and civil markets. Though each model type of multi-propeller drone has its own property variables or specs, such as the geometry design of blade, the geometry design of drone, the rotating speed of propellers, the first property of a multi-propeller drone is its number of propellers, which is most informative to identify the drone. Figure 1.1 gives examples of quadcopter, hexacopter and octocopter producted by DJI[2].

(a)	(b)	(c)
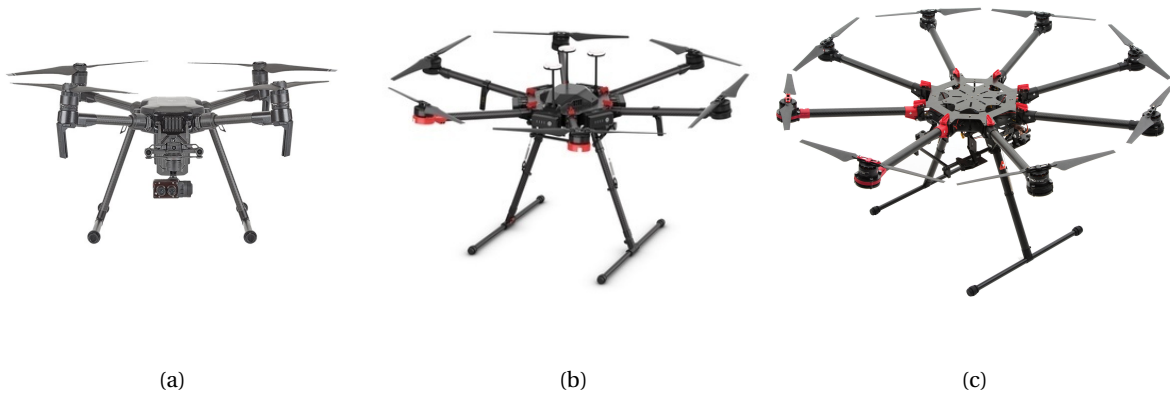
Figure 1.1: Examples of multi-rotor drones: (a)Quadcopter dji matrice 200, (b)Hexacopter dji matrice 600, (c)Octocopter dji s1000

The flight attitude of a flying multi-propeller drone is either hovering or maneuvering. The drone may hover at a specific place in the sky, go up and down vertically, rotate at the same place or move horizontally. For a multi-propeller drone, its flight attitude is determined by fundamental flight principles through the velocity synchronisation of the propellers. To introduce basic flight attitudes and principles, a quadcopter is given in Figure 1.2 for example . The multi-rotor drone takes off on the lift force of rotor-driving propellers. When the lift force of all the propellers equals to the gravity of the drone, the drone hovers in the air, otherwise with all the propellers accelerating or decelerating simultaneously, lift increases or decreases making the drone rise up or go down. The rotating propeller applies an anti-torque to the rotor, which drives the rotor to rotate reversely. To prevent the drone rotating due to the anti-torque, each pair of two adjacent propellers rotate reversely. Take quadcopter for example, Propeller M1 and M3 rotate counter-clockwise, while M2 and

M4 clockwise (see Figure 1.2a). The clockwise anti-torque by Propeller M1 and M3 is offset by the counter-clockwise anti-torque by Propeller M2 and M4, and thus the drone keeps steady and hovers. By controlling the rotation speed of each propeller, the drone is able to rotate or move forward, backward, to the left or right. With Propeller M2 and M4 accelerating, Propeller M1 and M3 decelerating, due to the total anti-torque, the drone rotates counter-clockwise (see Figure 1.2b). With Propeller M3 and M4 accelerating, Propeller M1 and M2 decelerating, due to the difference between the lift at front part and back part, the total lift is forward and upward, and thus the drone tilts and moves forward (see Figure 1.2c).
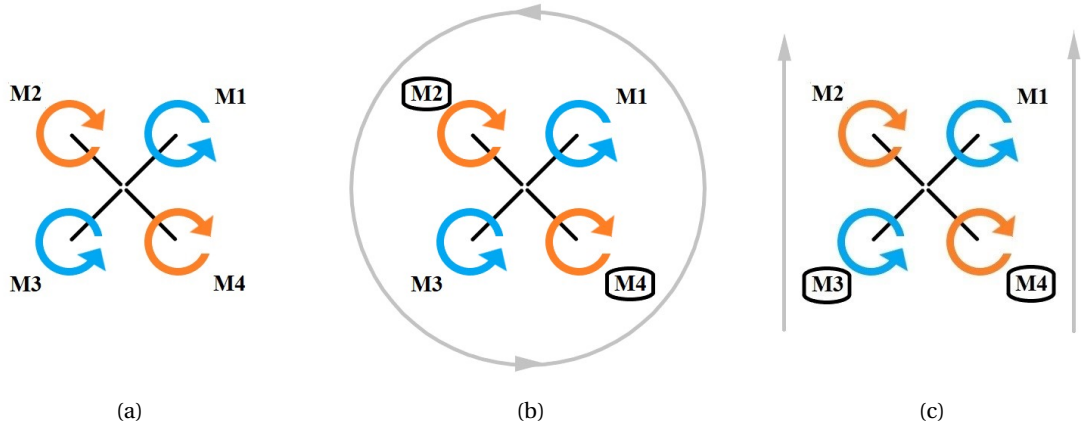
Figure 1.2: Flight attitudes of multi-rotor drone: (a) Hovering ,(b) Rotating,(c) Moving

1.2.2. Radar System and Doppler Processing

A radar system is defined by several parameters, such as carrier centre frequency f_c, bandwidth BW, pulse repetition frequency PRF, etc. In this study, the carrier frequency from several to tens of GHz is focused on, due to the fact that such frequencies are widely used in air traffic control (ATC), target tracking and weather radar systems. This carrier centre frequency offers the ability to observe targets in distance. The bandwidth of radar systems determines the range resolution that distinguishes targets at difference distance to the radar Tx/Rx antennas. This study starts from a single frequency of zero or very narrow bandwidth around the carrier centre frequency. This enables observing the motion and velocity of the drone target and its rotation parts. Pulse repetition frequency is the frequency at which the Tx antenna transmits EM signal pulses. For the single frequency discussed in this study, radar PRF can be seen as the sampling frequency of the antennas. For radar systems work in X-band, an PRF of several kHz is most common.

In this study, the recorded signal series is supposed to be a list of complex values. By applying Doppler processing to the complex value list, an image illustrating the motion or velocity of the target is achieved. The time interval of signal series, or the length of the complex value list, which is occupied in the Doppler processing gives CPI. In each CPI, the target is assumed of a range and velocity. Over several CPI, the change of target velocity is given. Short-time Fourier transform (STFT) is a standard operation of Doppler processing. In STFT, the window length for each Fourier transform corresponds to the CPI. If the velocity changes rapidly in a single CPI, the velocity cannot be accurately estimated. The radar setup parameters and Doppler processing

parameters together determine the micro-Doppler image of a specific drone target.

1.2.3. Acquisition of Drone Micro-Doppler Pattern

One of the issues discussed in this study is flexibly and efficiently acquiring drone micro-Doppler patterns. A simulation model generating the micro-Doppler patterns of multi-propeller drones is preferred over experimental measurement from the flexibility point of view. The simulation model should take several parameters into consideration. First, the radar setup parameters of f_c, PRF and the Doppler processing parameters of CPI should be included. A short CPI together with high PRF offers clear tracking of the radial velocity of the rotation propeller. With such a combination of variables, the thin-wire model can be validated in terms of the generated micro-Doppler patterns of propeller velocity changing over time in detail. Besides, parameters related to drone property and flight attitudes should be considered, such as the geometry design of the drone, the design of the drone properties and blades, the synchronisation of the propellers, etc. A simplified computational model is preferred over software simulation using fine in detail CAD models of multi-propeller drones. The simplification decreases the computation burden, in order to improve the efficiency, as long as the simplifies model achieves results accurate enough resembling the results given by the software simulations, in the same circumstances of variable and parameter setups.

1.2.4. Analysis and Feature Proposal of Drone Micro-Doppler Patterns

After collecting micro-Doppler patterns for multi-propeller drones in different circumstances, making an analysis of these micro-Doppler data is of much interest. Since the simplified simulation model generates micro-Doppler patterns using variables and parameters of drone property and radar setups, investigating the influence of these factors on the final drone micro-Doppler patterns shows the links and causality between them. Understanding influence, suitable features can be proposed characterising the micro-Doppler patterns, in order to describe and define the patterns with only a few feature values. This operation compresses the pattern images containing many pixel values into a relatively small feature space from which the property of the micro-Doppler image the drone and radar variables can be derived. Favoured features are of small feature dimensions and clear physical meanings.

A special attention is to be paid to long CPI circumstances (see Figure 1.3 [21] [13] [30] [31]). The micro-Doppler patterns are determined by the centre/carrier frequency, PRF and CPI. To achieve acceptable SNRs, there is a lower limit of the number of pulses in the coherent processing. In high PRF and short CPI circumstances, enough signal pulses can be achieved even within a short CPI. The radial velocity of the propeller is assumed to stay constant in each short CPI, and thus the rotation velocity is accurately estimated at each time point corresponding to a single CPI. As a result, over several CPIs, the change of the rotation velocity is clearly tracked, and the periodic quasi-sinusoidal micro-Doppler pattern is recorded. The situation is different in the low PRF and long CPI circumstances. Since the PRF is low, in order to gather enough signal pulses for a good SNR, a long CPI is necessary. Within such a long CPI, the propeller may have been rotating for many periods. In this circumstance, the exact radial velocity or the propeller at each angle and the tracking of the

periodic velocity change are unavailable anymore. This is a most common situation in radar systems of low PRF, such as weather radar systems. So in this work, the data collected with low PRF radar systems of long CPI is specially further investigated.
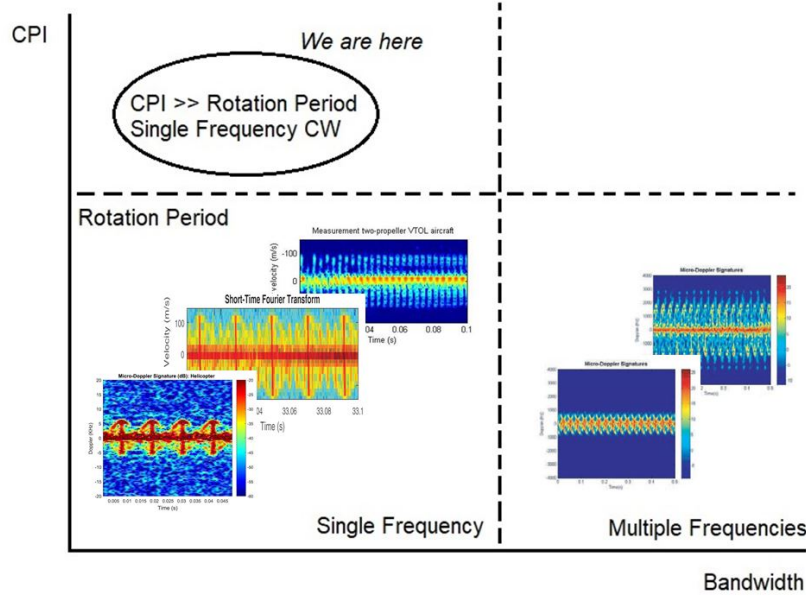
Figure 1.3: Long CPI circumstance of drone micro-Doppler pattern by radar systems

1.2.5. Drone Classification Based on Micro-Doppler Patterns

The classification and recognition of multi-propeller drones are reasonable methods to validate the proposed pattern features and highlight the potential use in real radar systems. The classification methods should recognise different model types of multi-propeller drones, according to the differences in their micro-Doppler patterns characterised by the proposed features. Clear straight structure is expected for the classification or recognition algorithm. Complex structure designs may be good for particular problems of specific data sets, but do not necessarily have advantages to draw general conclusions on the validation of the proposed features. The computational complexity of the algorithm, or the number of parameters of the algorithm model, should suit the feature dimension. Schemes of simplicity and efficiency overwhelm extreme performance of accuracy.

1.3. State of the Art

1.3.1. Collection of Micro-Doppler Patterns

Several methods were used to collect drone micro-Doppler pattern, most of which were based on EM simulation and real experiments. In these works, some issues should be noticed: a) Efficiency of EM simulation, b) Flexibility of real measurements, c) Influence of observation angle, propeller synchronisation and other factors.

The RCS of multi-propeller drones have been performed in numerous papers, either experimentally or in

simulation. In [24], the authors simulated and measured the mono-static RCS of a commercial quadcopter. The simulation was performed in CST, accurately modelling the geometry design and material complex permittivity. The measurement took place in an anechoic chamber with a network analyser and a horn antenna. The RCS was simulated/measured from 1 GHz to 10 GHz, with LOS in front of the drone, and four propellers together of 0, 45, 90 and 135 degrees to LOS. In this work, only drone RCS was investigated, while micro-Doppler pattern illustrates the drone's motion and other properties. The RCS of the whole drone was considered, combining backscattered signals from both the drone body and drone propellers, while the signals scattered from propellers contribute most to the micro-Doppler pattern reflecting propeller property, rotation and drone flight attitude. The LOS was set in front of the drone, while in practice, the drone could be observed at any angle horizontally. Propellers were set only at 4 angles in horizontal plane, which is enough neither to investigate the propeller RCS at different angles, nor to generate micro-Doppler pattern of rotating propellers. The synchronisation of propellers in angle is not discussed.

In [29], the authors simulated the RCS of quad-, hexa- and octocopters in X-band (10 GHz). The simulations were performed using FEM and MoM methods with fine and simplified CAD models of drones at [0, 360] degrees in horizontal plane, and corresponding micro-Doppler patterns were computed using STFT for fine and simplified CAD models. It was demonstrated that the simplified model gave similar micro-Doppler patterns as the fine model did. In this work, the angle shifts between neighbouring propellers were 90 degrees. However, in practice, the propeller angle shifts are random from 0 to 360 degrees, and the angle shifts may vary over time if the propellers are of various rotation velocities for a moving drone.

In [27], the authors simulated the RCS of a fine CAD model of two-balde propeller in both horizontal and vertical planes using FDTD method, from 1 GHz to 10 GHz, for 72 angles in rotation plane. This simulation illustrated the RCS of a specific propeller in detail, but it was very time consuming, taking 36 hours on a regular PC – For another propeller, another tens of hours are required. Micro-Doppler of a single drone may be further computed from the RCS results.

In [10], the author introduced real measurement data of helicopter drone, fixed-wing drone, quadcopter drone and Harris's Hawk at X-band (9.7GHz). The micro-Doppler data of quadcopter was of "the sampling frequency ... sufficiently high to avoid aliasing in Doppler", offering good SNR within short CPI, clearly showing the periodic pattern. In practice, especially for radar systems with low PRF, clear periodic quasi-sinusoidal patterns are not always available. Besides, the real measurement data was highly dependent on object and measurement setup – It is challenging to collect stable pattern of moving drones, and it requires new measurements for different drones.

In [31], the authors measured the micro-Doppler patterns of quad-, heli- and hexacopter at X-band (9.8 GHz) and K-band (24 GHz). The drones were set indoor at specific location. In this work, neither the radar observation angle nor the synchronisation of propellers in angle and velocity was considered as a factor influencing the micro-Doppler patterns. Besides, the measured micro-Doppler patterns were again periodic quasi-sinusoidal of good SNR.

1.3.2. Drone Classification Using Micro-Doppler Patterns

Several methods were used to extract suitable features for micro-Doppler patterns and perform classifications. These methods gave many good results, but also raise concerns in following aspects: a) Most works focused on periodic micro-Doppler pattern, b) Some methods required large size data sets, c) The influence of drone variables on micro-Doppler patterns and drone classification results.

In [31], after measuring indoors the micro-Doppler patterns of different drones at X-band and K-band, the authors applied Principal Components Analysis (PCA) to the pattern images directly and selected the first three features in each bandwidth. The six features together were further used in Support Vector Machine. Using dual-band radar data improved the performance than single band radar data. By this means, the micro-Doppler images of drones were seen as just images, without using the knowledge of drone property, radar system and EM scattering.

In [17], the authors proposed physical features for micro-Doppler patterns of human activity, such as base velocity, Doppler bandwidth and cadence frequency. Support Vector Machine using these features led to good results classifying different human activities, such as running, walking and crawling. In [10], similar physical features were extracted from drone micro-Doppler patterns (i.e. TVD, Time Velocity Diagram), and then poured into Boosting classifiers. These features had clear physical meanings, but they were proposed for periodic patterns – For linear patterns, these features do not exist anymore.

In [11], the authors transformed the measured micro-Doppler images of human activity into Cadence Velocity Diagram (CVD) and proposed features for the CVD, such as cadence frequency and velocity interval. Support Vector Machine was employed in this work to perform activity classification. This method was proposed for clear periodic patterns. Besides, for periodic micro-Doppler patterns of drones, this method would generate much redundancy, due to the symmetry of the drone micro-Doppler pattern which differs from the pattern of human activity. In [13], the authors made analysis of the influence of different factors on micro-Doppler patterns for periodic quasi-sinusoidal patterns. By performing Singular Vector Decomposition (SVD), features were extracted from the first several singular vectors. These features were shown working well for indoor measured periodic patterns. The authors also mentioned linear micro-Doppler patterns, but further investigation is needed.

In [16], the authors applied Convolutional Neural Networks (CNN) to the merged images of micro-Doppler patterns, measured in anechoic chamber and outdoors, and their CVDs. This method gave good classification accuracy of two types of drones. Since CNN was occupied in this work, it required large data sets in order to train the CNN. Besides, the CNN structure of GoogLeNet was selected, while this structure was not initiated for radar micro-Doppler pattern classification. The influence of drone property and other measurement parameters was not directly revealed in this work, which were possible reasons for the large data sets and complex network structure.

In [25], the authors applied multilayer perceptron artificial neural networks to the real and imaginary parts of drones's EM reflection signals in the time and frequency domains, in order to classify the number of propellers and blades, and to estimate the blade length and propeller rotation speed. In this work, the full

information of the drone reflection in both time and frequency domains is imported to the artificial neural network, and no specific features are extracted, thus the physical interpretation of the method and result is not directly given. Besides, the geometry structure design of the drone is not considered in the work.

In above researches, micro-Doppler patterns were most achieved by applying STFT to simulation or measurement radar signals. In [21], the authors proposed another way to compute micro-Doppler pattern – Empirical Mode Decomposition (EMD). The radar echo signal was first decomposed into a set of oscillating waveforms by EMD. Several statistical and geometrical features of the first oscillating waveforms were then extracted as features characterising the decomposed radar signal. The features were then introduced to a nonlinear Support Vector Machine for drone classification. This method gave drone classification results comparable to other methods based on STFT micro-Doppler patterns, while the results of EMD did not have specific meanings corresponding to drone properties or measurement parameters.

1.4. Research Approaches

1.4.1. Drone Modelling

Mathematical modelling is an important approach in this study. A model is developed in the mathematical way, simplifying the propellers of the drone as thin wires using EM scattering theories, generating the backscattered signals. First, a model of a propeller is introduced, taking the variables of propeller property as input values, such as the number of blades, the length of blade, the geometry design of propeller, etc. In this model, the angle of propeller blade relative to the LOS is set as a function of time, the initial angle and the rotation angular velocity of the propeller. Then the model of a single propeller is expanded to a drone of multiple propellers, giving the synthetic backscattered signals of all the propellers. For a multi-propeller drone, the geometry design of the drone is also considered, since the geometry design has an influence on the scattered signals. Applying STFT to the signal series gives the micro-Doppler pattern of the multi-propeller drone.

Experiments play an important role in this study. Experimental measurements of the backscattered EM signals of a drone propeller is performed in anechoic chamber. The anechoic chamber offers clear scattered signal results of good SNR. By applying STFT to the measured signal series, the micro-Doppler pattern of the propeller is achieved. Given the same setup parameters of the measurement and Doppler processing, the previously proposed model is validated by the experimental measurement results, if the simplified model gives the same micro-Doppler pattern as in the measurement.

In this study, software simulations gives extra information. Simulation results of the backscattered signals of a drone propeller is also achieved, using EM simulation software FEKO. The scheme and strategy in the FEKO simulation is almost the same as in anechoic chamber experiments, but the software simulation is able to consider full wave situation. The backscattered signals and the micro-Doppler patterns can be achieved and investigated in not only the propeller rotation plane, i.e. HH plane, but also in other polarimetric channels. The micro-Dopller patterns from FEKO simulations is another way to validate the patterns generated by the simplified model.

1.4.2. Micro-Doppler Pattern Analysis

Analysis on the micro-Doppler pattern images is necessary in this study. As the simplified model is validated, micro-Doppler patterns for multi-propeller drones in different circumstances can be generated. The micro-Doppler patterns of drones of different number of propellers, different propeller properties and different geometry designs are simulated from the thin-wire model. The radar setup parameters and the Doppler processing parameters are additional variables in each model-based simulation. By analysing the micro-Doppler patterns in different circumstances of input variables, the influence of these variables and factors on the final micro-Doppler patterns are investigated.

Observation and heuristic methods play an important role in this study to propose suitable features in order to characterise the micro-Doppler patterns. The ideal features should contain clear physical meaning illustrating specific properties of the micro-Doppler image, such as the image's statistic and geometrical properties. The feature should also relate to the variables and parameters of the drone and radar system used in the simplified model, and reflect their influence on the final pattern. After feature proposal, a selection of features is necessary, eliminating redundant features, in order to characterise more information about the micro-Doppler pattern with lower feature dimensions.

PCA is a suitable feature selection algorithm in this work. The statistic and geometrical features extracted from micro-Doppler images have clear physical meaning and contain more than enough information about the model type and flight attitudes of multi-propeller drones. By applying PCA, these features are projected to new feature space of lower dimensions. In such feature space, the original proposed features of major importance are mapped to principal feature basis, while the not so important original proposed features are eliminated and the redundant features are compressed. Singular Value Decomposition SVD is a possible method to perform PCA, while the size of the dimension of the new feature space is determined by the trend of the singular values. As long as the selected principal features contain enough information for further classification, a smaller size of feature dimensions is preferred for its computation efficiency. After determining the size of the feature dimension, the data of micro-Doppler patterns is to be shown in the feature space, in order to preliminarily evaluate the selected principal features.

1.4.3. Drone Classification

Classical methods and algorithms for classification problems are reviewed and introduced to this study. The aim of the classification step is to validate the proposed features, evaluate the features and initially highlights the possibility to expand these feature to real drone and radar data. The classifiers are chosen according to the property of the micro-Doppler pattern data and the size of the proposed feature dimension. The classification accuracy is the main criteria to evaluate the classifiers and the features. Other criteria to assess the performance of this part of the study is the complexity of the chosen scheme in time and computation, and the potential to be applied to real data.

Due to the aim of validation and inspiration, a clear structure and intuitive explanation is a priority of the classification algorithm, while the extreme performance of classification accuracy is unnecessary. SVM

classifiers are suitable for this classification problem and will be implemented in following chapters. An SVM classifier is to be trained in standard fashion with the PCA-selected features of thin-wire model-based data of micro-Doppler patterns, and then tested with more data randomly generated by the model. In the implementation of SVM classifiers, the schemes of binary and multi-class classification are to be considered, and the scaling parameter of the kernel function is to be tuned. In order to evaluate and improve the performance of the SVM classifier, the learning curves will be tested. So the appropriate feature dimension, training data set and classifier parameters in different multi-propeller drone scenarios will be investigated.

Other classifiers, like deep learning algorithms, such as CNN, have been used in other researches and will be reviewed, but not discussed in detail in this work. These techniques rely on large data set and usually offer extremely good performance, but are in the lack of clear explanation of the link between input data and classification results. If the proposed SVM classifiers work well achieving a satisfactory performance, the implementation of deep learning algorithms may not be a necessity, because these schemes take much effort in time and computation resource and do not gain much in classification performance improvement.

1.5. Thesis Structure

The research approaches and results are shown and analysed in detail from Chapter 2 to Chapter 6. The chapters are organised as follow:

- Chapter 2 introduces an simplified thin-wire model to estimate the backscattered radar signals from a multi-propeller drone. The micro-Doppler pattern of the multi-propeller drone is also given by applying STFT to the signal series.

- Chapter 3 validates the simplified EM model proposed in previous chapters with experimental and simulation results achieved in anechoic chamber and EM simulation software in different circumstances of input variable combinations. As the model validated, an analysis on the model-generated micro-Doppler patterns generated in different circumstances is presented.

- Chapter 4 proposes features for the micro-Doppler patterns under long integration time circumstances, based on understanding the influence of variables on micro-Doppler patterns. This chapter also performs the classification/recognition of the multi-propeller drones based on their model-based micro-Doppler patterns.

- Chapter 5 applies the classification method/classifier obtained in previous chapters to real data measured by radar system and analyses the performance of the classifiers.

- Chapter 6 draws the conclusion of the this study with discussion on the results and offers recommendations for future research.

2

Electromagnetic Wave Scattering and Micro-Doppler Pattern from Propellers and Drones

2.1. Investigation Approaches and Steps

In order to investigate the EM reflection signal and micro-Doppler pattern of multi-propeller drones, the RCS of a single propeller and of a multi-propeller drone is collected in measurements and simulations.

First, the backscattered EM signal of a single propeller is achieved. Two approaches are employed here, measurement of a real drone propeller in EM anechoic chamber and simulation of a 3-D structure model of drone propeller using EM simulation software. Performing STFT to the backscattered signal or RCS achieved from either of these means gives the micro-Doppler pattern of a single drone propeller.

The second stage is about the micro-Doppler pattern of a drone containing multiple propellers. EM anechoic chamber measurement and software simulation may not be the most appropriate methods here, since the synchronisations of propellers correspond to many combinations in terms of the angles relative to LOS and rotation velocity and burden the measurements and simulations. Measurements of the micro-Doppler patterns of multi-propeller drones in open air by real radar systems is a suitable solution. For a multi-propeller drone hovering in the sky, the rotating propellers are the only sources introducing micro-Doppler patterns.

2.2. Investigation of Single Propeller

2.2.1. EM Chamber Measurement Setup

DUCAT is a 6m*3m*3m EM anechoic chamber. It is furbished with absorbers on the wall, ceiling and floor to eliminate RF reflection. The mechanical subsystem consists of several stepping motors providing 3-D sweep measurement in different azimuth and elevation angle. A horizontal rotatable platform which supports the object under test sits at one remote end of the chamber. A pair of bistatic antennas sit at the other remote end of the chamber transmitting and receiving EM signals (Figure 2.1 [1]). The transmitter and receiver antennas are set at the same position in DUCAT and thus the bistatic radar system can exactly be seen as a monostatic radar system. The antennas are linked to the ports of a VNA which triggers and records the signal.
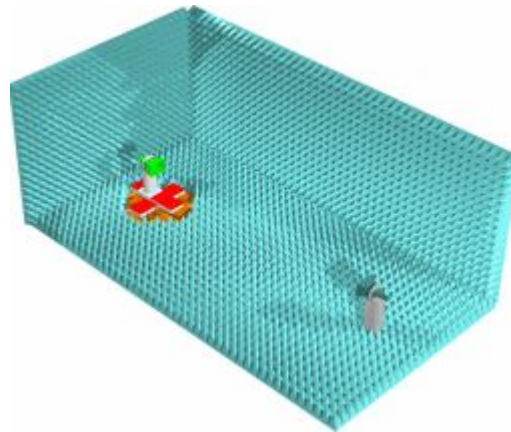
Figure 2.1: EM anechoic chamber f DUCAT

The propeller used in this measurement is R2170 Folding Propeller CW produced by DJI (Figure 2.2 [6]). This propeller is selected as a representative of most popular on market two-blade propellers. In each blade, there are two main fringes in front and end shifted in angle, and the length of the main fringe is 0.2665 m, just the propeller radius. The minor fringe is 0.0533 m and 15° shifted from the main fringe in the horizontal plane. The propeller is mounted on the horizontal rotatable platform in DUCAT EM anechoic chamber, placed at 3.3 m distance from the Tx/Rx antennas (Figure 2.3). In the measurements, the propeller rotates in 450 seconds from -180° to 180° with a step of 0.036°. For every angular position a vector network analyser (VNA) recorded 21 samples of reflection coefficient sweeping from 2 GHz (S-band) to 12 GHz (X-band). This frequency interval from S-band to X-band is selected because it is most used in radar systems of air traffic control, weather monitoring and target tracking.

During the measurement campaign, three measurements are performed in total of the RCS of the propeller, the RCS of a 0.2 m by 0.2 m reference metal plate and the DUCAT background without any object under test. The backscattered EM signal from the empty anechoic chamber is measured for calibration, while the backscattered EM signal from the standard metal plate is used for the calculation of the propeller's RCS. In each measurement, the range from the antennas to the object under test is 3.3 m, and the object is illuminated by the antennas scanning from 2 GHz to 12 GHz. The reflection coefficient S_{11} is measured and recorded by VNA in each measurement. Again, only HH polarisation is considered in the measurements,
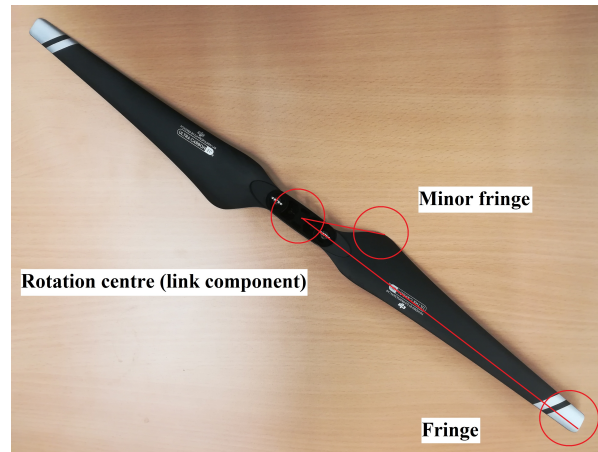
Figure 2.2: Propeller DJI 2170 under measurement
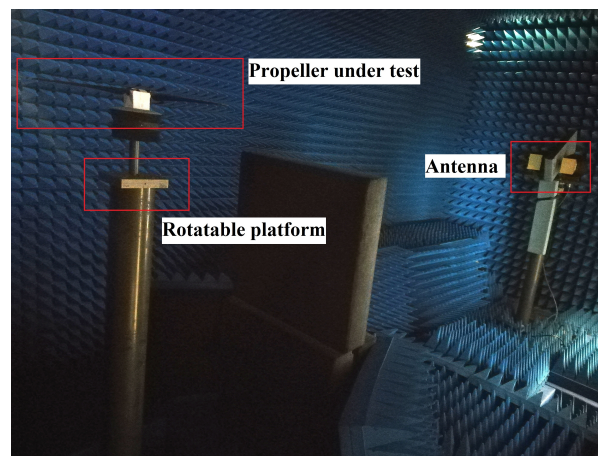
Figure 2.3: Measurement layout in DUCAT

since both the geometry and rotation of the propeller are most in horizontal plane.

2.2.2. Propeller RCS Measured in DUCAT

The calibration of the power of the EM signal backscattered from the propeller is performed by subtracting the background backscattered signal power measured in the empty anechoic chamber from the original received backscattered signal power from the propeller. The calibration is also performed to the backscattered signal from the standard metal plate. The RCS of the propeller after calibration is evaluated using equation as follows

$$\sigma_{prop} = \sigma_{mp} \cdot \frac{P_{r,prop}}{P_{t,prop}} \cdot \frac{P_{t,mp}}{P_{r,mp}} \tag{2.1}$$

where σ_{mp} is the RCS of the metal plate, $P_{r,mp}$ and $P_{t,mp}$ are the received and transmitted power of metal plate, and $P_{r,prop}$ and $P_{t,prop}$ are the received and transmitted power of propeller.

In the experimental measurements, the RCS of the metal plate is calculated as[14]

$$\sigma_{mp} = \frac{R^4 (4\pi)^3}{G_t G_r \lambda^2} \frac{P_{re}}{P_{tr}} \tag{2.2}$$

where R is the range from the antennas to the object under test, G_t and G_r is respectively the transmitter and receiver antenna gain, λ is the wavelength of the incident wave, and P_r and P_t is respective the transmitted and received power. The accurate RCS of a 0.2 m by 0.2 m metal plate can be can be calculated in theory as

$$\sigma_{mp} = \frac{4\pi a^2 b^2}{\lambda^2} \tag{2.3}$$

where a and b are denoted as half of the two sides of the rectangular flat plate[20]. The RCS of the metal plate measured in DUCAT chamber may slightly differ from the accurate value calculated in theory, due to the experimental environment and the accuracy of the instruments, and this difference should also be calibrated from the measured data.
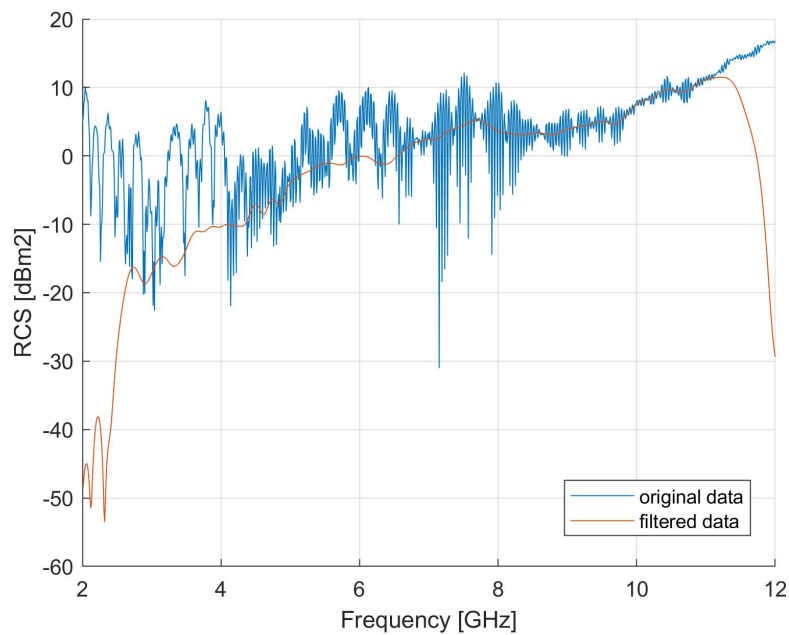
Figure 2.4: Measured RCS of 0.2 m by 0.2 m metal plate

The original measured RCS of the metal plate is shown as the blue curve in Figure 2.4. It is noticed that there is oscillation at different frequencies over the bandwidth from 2 GHz to 12 GHz. This oscillation is introduced by multi-path propagation in the anechoic chamber. In order to eliminate the oscillation, the measured data of the RCS of the metal plate is processed as follows. The power ratio of the received and transmitted power in frequency domain is performed IFFT to get signal in time domain (or range domain). A filter is applied to the signal series in time domain, in order to cut off the signal values which arrive later than a specific time threshold corresponding to the range between the target under test and the Tx/Rx antennas. After the filtering in time domain, only the signal values directly propagate and reflect from the object under test is kept in time domain. Applying FFT to the filtered signal series in time domain generates smooth curve of RCS in frequency domain over the bandwidth from 2 GHz to 12 GHz. Using Equation 2.1, the RCS curves of the metal plate perpendicular to LOS after the filtering in time domain is calculated and shown in frequency domain over the bandwidth from 2 GHz to 12 GHz as the red curve (Figure 2.4). The comparison between the

blue and red curves in Figure 2.4 illustrates that from 3 GHz to 11 GHz, the filtered data resembles the original one, but without the oscillations. Below 3GHz or above 11 GHz, the filtered data differs from the original one, because of the time window employed in the filtering processing.

Using Equation 2.1, the RCS (only the magnitude of the power) of the propeller at different frequencies and azimuth angles is shown in Figure 2.5. Along the angle axis, the maximum RCS of the propeller appears at $\pm 90°$ when the propeller is perpendicular to LOS, and this corresponds to the fact that the cut area of the propeller achieves its maximum when the propeller diameter is perpendicular to the LOS. It is also shown that the RCS of the propeller varies at different frequencies. At higher frequency near 12 GHz, the strong reflection appears exactly at $\pm 90°$. As the frequency decreases getting closer to 2 GHz, the strong reflection does not gather around $\pm 90°$ anymore, and even around $\pm 90°$ the maximum reflection starts to fluctuates along the frequency axis. This can be explained by the theory of EM scattering[28]. At 12 GHz, the radius of the propeller is large compared with the wavelength ($2\pi r/\lambda = 66$), and thus the scattering phenomenon stands in the optical region, while at 2 GHz, the radius of the propeller is comparable with the wavelength ($2\pi r/\lambda = 11$), and the scattering almost happens in the Mie region.
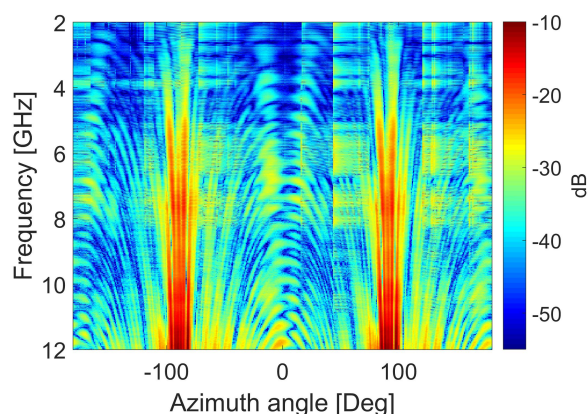
Figure 2.5: Measured RCS of DJI 2170 propeller in DUCAT chamber

Specially, Figure 2.6 shows the RCS of the propeller at X-band (10 GHz) and S-band (3 GHz). It should be noticed that the largest RCS value is -18 dBm^2 or -23 dBm^2 at 10 GHz or 3 GHz, and this should be considered to estimate the maximum detection range in real X-band or S-band radar system, beyond which the propeller as well as its micro-Doppler pattern is invisible. The RCS achieves several maxima as the propeller rotates. Corresponding to the angular between the propeller and the LOS at X-band and S-band, and Figure 2.7 shows these angles to LOS when the RCS achieves its maxima. The maximal RCS appears at around 90° and 100° correspond to the two long edges at X-band and S-band, while the local maxima at about 35° and 165° only appear obviously strong at S-band, which may be the result of constructive interference.

2.2.3. Propeller RCS Simulated in FEKO

In previous sections, in order to collect the RCS of the propeller from which the micro-Doppler pattern of the rotating propeller is calculated, anechoic chamber measurements are performed, while another way to
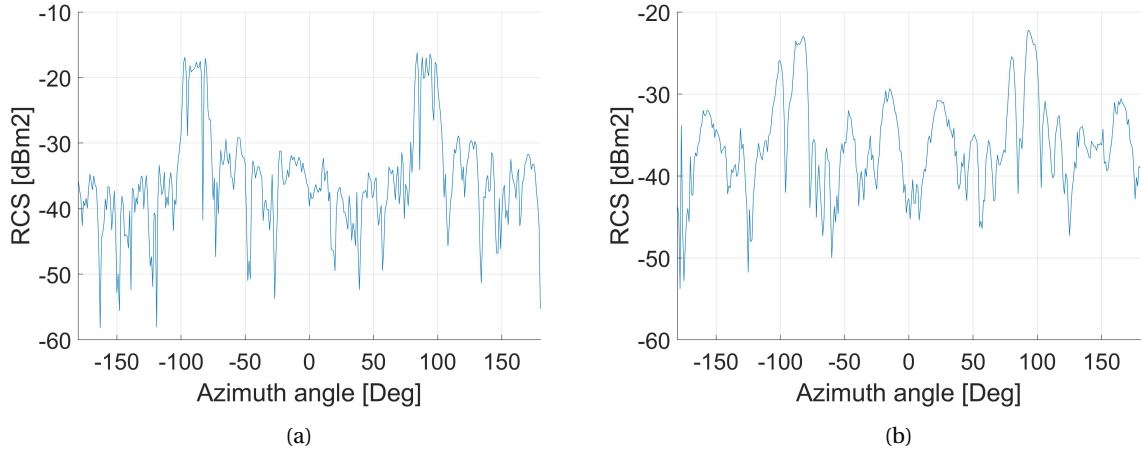
Figure 2.6: Measured RCS of DJI 2170 propeller in DUCAT chamber at specific frequencies: (a) 10 GHz, (b) 3 GHz
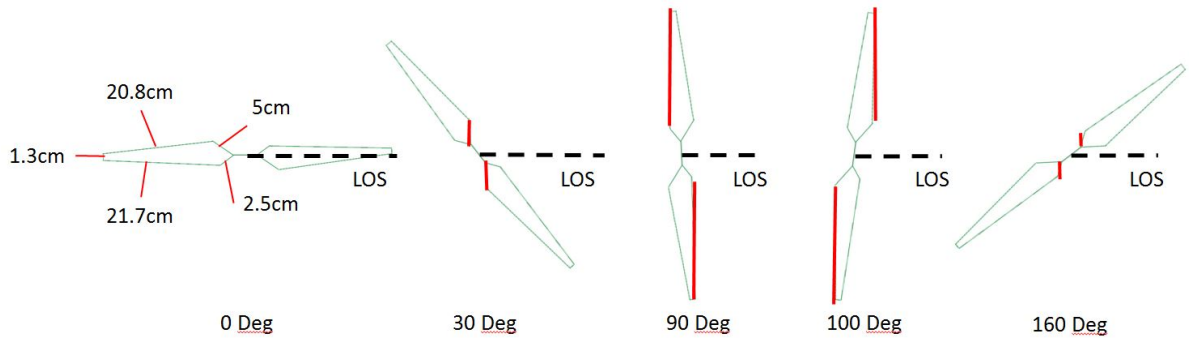
Figure 2.7: Angle to LOS of DJI 2170 propeller in DUCAT chamber when the RCS achieves the maxima

achieve the propeller RCS is software EM simulation. In this section, FEKO is introduced to simulate the RCS or basckscattered EM signals of the two-blade propeller.

A 3-D CAD model illustrating the fine geometry design of a two-blade propeller is introduced here [7]. This is a geometry model of the propeller DJI E1200 which is almost the same as the DJI R2170 propeller employed in the anechoic chamber experiments and thin-wire model simulations, but slightly different in the length of the blade. In each blade of the propeller, the length of the main fringe is 0.2159 m, and the length of the minor fringe is 0.0432 m. This difference in the size of the propeller blade is easily converted into the same scale in terms of the wavelength of the incident EM signal or the radar centre frequency.

Figure 2.8 illustrates the 3-D CAD model of the propeller DJI E1200. The rotation centre of the propeller is set at the origin point of the FEKO simulation coordinate system in the far field of the EM signal source and the observation point. The EM scattering simulations are performed over the bandwidth from 3 GHz to 12 GHz with the frequency step of 0.5 GHz, in the horizontal plane with the azimuth angle step of 1°. In each azimuth angle step, the incident EM wave is set in line with LOS monostatically. In the simulations, the material of the propeller blades are set as carbide fibre material with $\epsilon_r = 1$ and $\sigma = 66.67e^3$ [24], and the finite element method FEM solver is occupied.

The RCS (only the magnitude of the power) of the propeller at different frequencies and azimuth angles
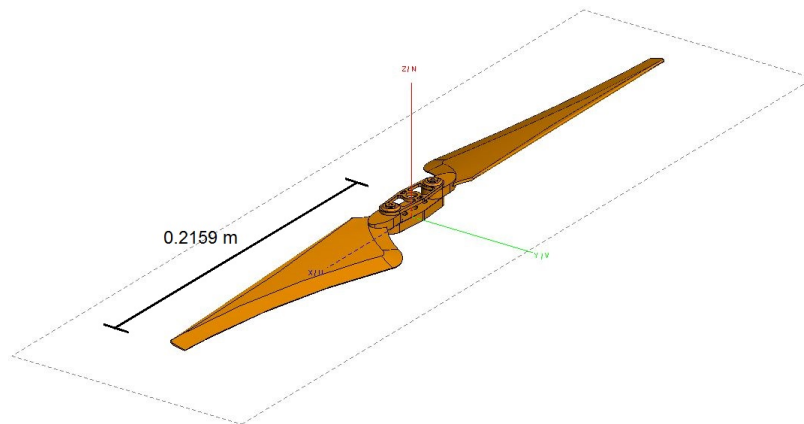
Figure 2.8: The 3-D CAD Model of DJI E1200 propeller that has been used for the FEKO simulation

is shown in Figure 2.9. Specially, Figure 2.10 shows the RCS of the propeller at X-band (12GHz) and S-band (4 GHz). It is shown that the RCS of the two-blade propeller simulated in FEKO is very similar to the RCS measured in the DUCAT chamber experiments, and so they illustrate the same EM phenomena. Specially, in Figure 2.10a, the simulated shape and magnitude of the propeller RCS distributed over azimuth angles is almost the same as in Figure 2.6a measured in DUCAT chamber. In Figure 2.10b, the shape of the propeller RCS distributed over azimuth angles is similar to its counterpart in Figure 2.6b, while the magnitude of the RCS curve is several dB stronger, because of the very good dynamic range of the FEKO simulations free from environment noise. Again the local maxima at about 30° and 160° appear again in the RCS curve at S-band.
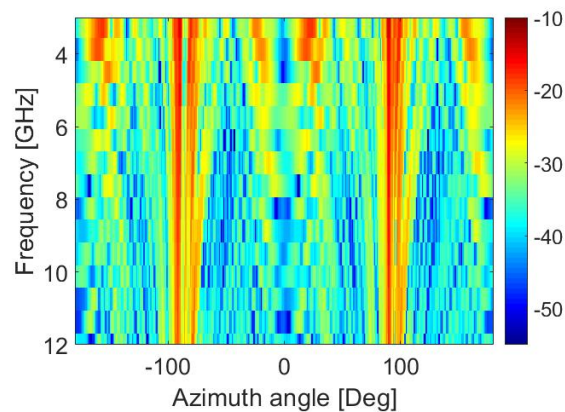
Figure 2.9: Simulated RCS of DJI E1200 propeller in FEKO

2.2.4. Propeller RCS Simulated in FEKO: A Single Blade

In order to understand the RCS local maxima at about 35° and 165° at S-band in both the DUCAT measurements and FEKO simulation, the RCS of a single blade of the propeller is simulated in FEKO. Figure 2.11 illustrates the 3-D CAD model of a single blade of the propeller DJI E1200.

Figure 2.12 shows the RCS of a single blade at X-band and S-band. At X-band, the global maximal appear at about -90° and 90° correspond to the curving long edge and the straight long edge. At S-band, the straight
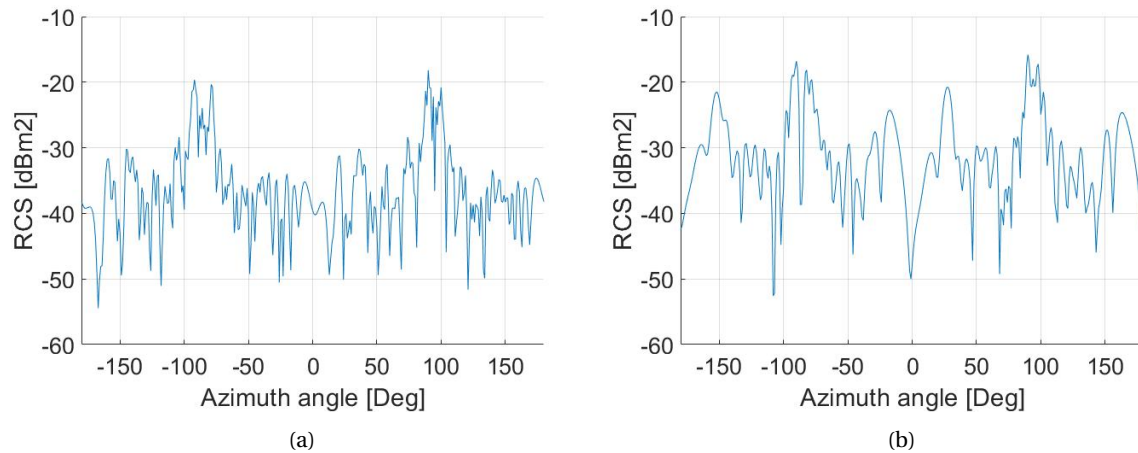
Figure 2.10: FEKO simulated RCS of DJI E1200 propeller in FEKO at specific frequencies: (a) 12 GHz, (b) 4 GHz
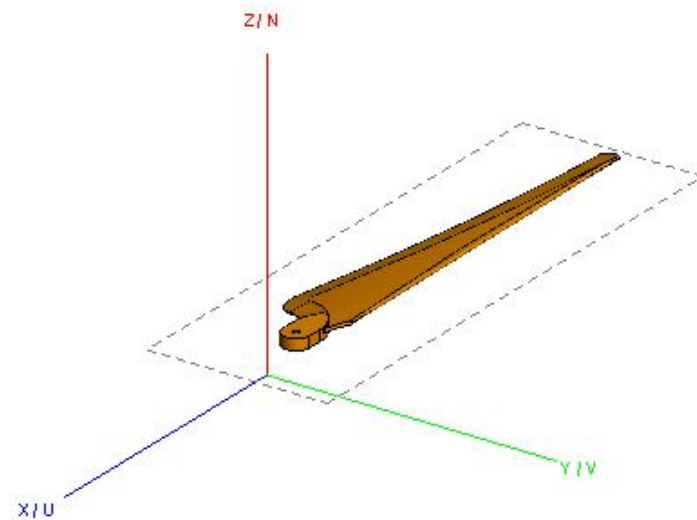
Figure 2.11: The 3-D CAD Model of a single blade of DJI E1200 propeller that has been used for the FEKO simulation

long edge of the blade introduces the global maximum at exactly 90°, while the curving long edge introduces weaker but wider maxima at around -90°. Strong peaks appear at about 30° and 150°, agreeing with that in the two-blade propeller simulation (see Figure 2.10), meaning the strong local maxima in Figure 2.10 is most contributed by the constructive interference due to the geometry structure of the blade – The distance of most strong reflection points on the blade is just $\lambda/2$ at 30° and 150° in S-band, thus introducing strong reflection.

2.2.5. Micro-Doppler Pattern of Propeller Measured in DUCAT

Since the results from anechoic chamber measurements and FEKO simulations resemble each others, the following sections focus on the anechoic chamber results, and the micro-Doppler patterns are mainly achieved from the data measured in anechoic chamber experiments.
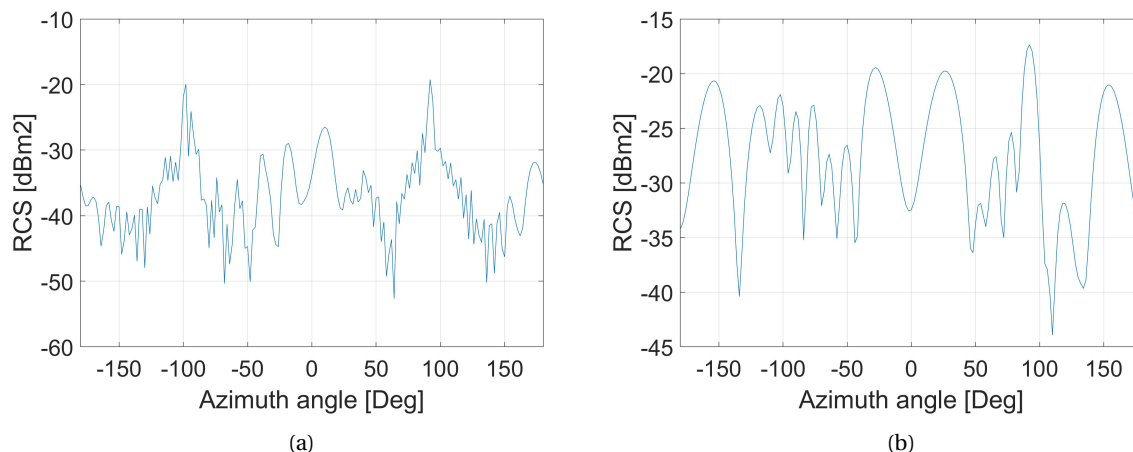
Figure 2.12: FEKO simulated RCS of a single blade of DJI E1200 propeller in FEKO at specific frequencies: (a) 12 GHz, (b) 4 GHz

Micro-Doppler pattern of propeller can be achieved by performing STFT on the measured RCS of a rotating propeller. The layout and setup of the measurement is similar to that of RCS measurement mentioned in previous sections. For the estimation of micro-Doppler pattern, four measurements are performed in total, at 3.315 GHz and 10 GHz, of propeller scenario and background scenario. In each measurement, the platform rotates clockwise from 0° to 180° in 450 seconds, and 10,000 sample points of complex value are recorded in "*.s2p" file format by VNA. Applying 1,024-point Short-Time Fourier transform (STFT) with 896 overlapped points to the complex reflection coefficient data measured on specific frequency simulates the micro-Doppler patterns of the slowly rotating propeller with angular velocity $\Omega = 0.13$ rpm which is observed by a radar with the centre frequency of 3.315 GHz and 10 GHz, PRF = 22 Hz and CPI = 46.08 s.

The micro-Doppler pattern of the rotating propeller over half of rotation period is presented in Figure 2.13. There are two pairs of curves of strong reflection in the figures. The major envelope curves of the micro-Doppler components correspond to the larger radial velocity introduced by the main fringes of the blades. The minor envelope curves of the micro-Doppler components which are better presented in Figure 2.13a correspond to the smaller radial velocity introduced by the minor fringes of the blades. The radial speed of the two-blade propeller in half a rotation periodicity is clearly indicated in the figure. In either X-band (10 GHz) and S-band (3.315 GHz) measurements, the maximum micro-Doppler frequency of a propeller of 53.3 cm in diameter and 450 seconds of rotation period is approximately 0.25 Hz and 0.08 Hz, which correspond to the main envelope curves in the figure. The 0 Hz Doppler component in the figure is introduced by the rotation centre (link component) of the propeller.

In previous example, the CPI is much longer than the propeller rotation period, and the rotation detail is recorded well. Figure 2.14 gives the micro-Doppler pattern of the rotating propeller based on the DUCAT measurements at X-band and S-band. In this example, the propeller rotation period is about 0.9 ms, while the CPI is 1.024 s. In this circumstance, the rotation detail in the propeller micro-Doppler pattern is lost, and the micro-Doppler patterns are not quasi-sinusoidal periodic but linear. In the long CPI circumstance, the linear micro-Doppler patterns distribute at the same frequency over the bandwidth, and the detail of the geometry
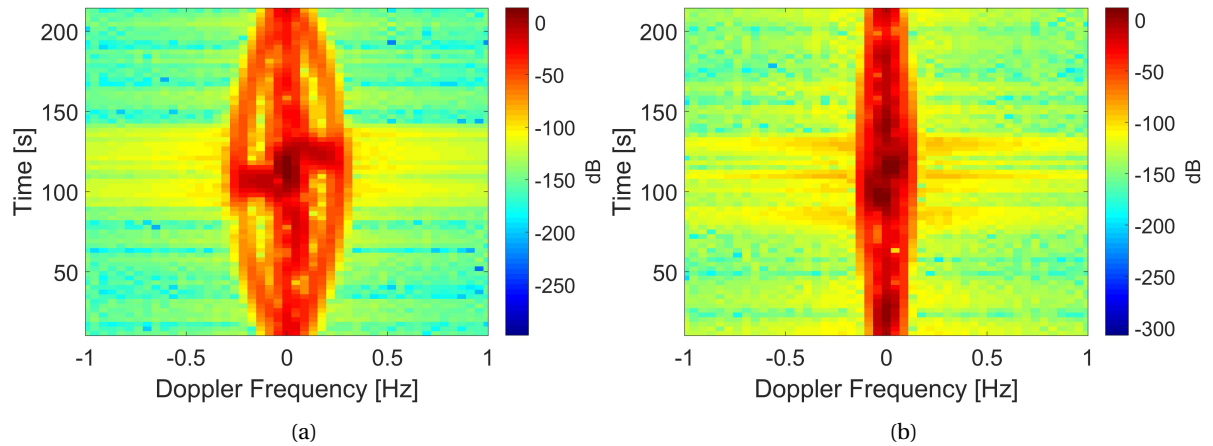
Figure 2.13: Micro-Doppler patterns of DJI 2170 propeller based on DUCAT measurement in short CPI circumstance: (a) 10 GHz, (b) 3.315 GHz

structure of the propeller does not influence the micro-Doppler pattern much.
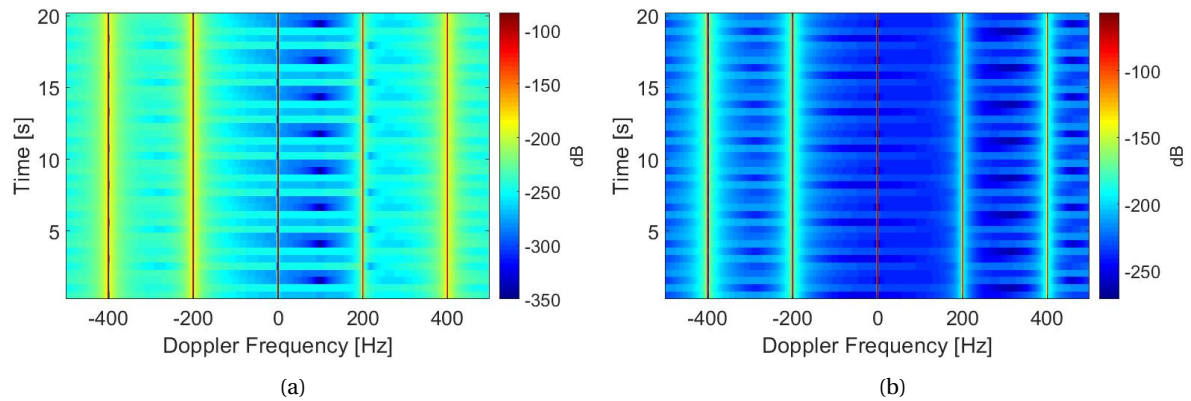
Figure 2.14: Micro-Doppler patterns of DJI 2170 propeller based on DUCAT measurement in long CPI circumstance: (a) 10 GHz, (b) 3.315 GHz

2.3. Investigation of Multi-Propeller Drone

2.3.1. Open Air Measurement Setup

PARSAX is an S-band polarimetric Doppler radar system (Figure 2.15) [5]. This is a highly reconfigurable research FMCW radar mounted on the roof of EWI building on TU Delft campus [19]. Full polarimetric measurements in the channels of HH, HV, VH and VV can be implemented by independent polarimetric horizontal and vertical channels in both in transmitter and receiver. The radar bandwidth can be set up to 100 MHz corresponding to the best range resolution of 1.5 m. For each single channel the transmit power can be set up to +50 dBm, while the noise floor of the receivers is around -93 dBm, which offers a very good dynamic range of recorded data. In this radar system, the Doppler processing of the received signal series of complex values up to 5,100 complex samples can be performed in real-time using the FPGA-based digital receiver together with the GPU Doppler processor in coherent range profile.

Figure 2.15: PARSAX radar on the roof of EWI Building, TU Delft campus

The multi-propeller drone used in the measurements is M600 produced by DJI (Figure 2.16 [4]). This propeller is selected as a representative of hexacopters. There are quadcopters, hexacopters and octocopters most common on multi-propeller drone market, and usually the latter two types are of larger size in drone diameter and larger size of drone propellers, while the smaller propellers of quadcopters usually have faster rotation speed in general. In the M600 employed in the open air measurements, there are six arms distributed symmetrically around the centre of the drone, of 0.567 m in length, i.e. the diameter of the drone, and 60° shifted away from each other in the horizontal plane. A two-blade propeller of the same model introduced above DJI R2170 is attached at the far end of each drone arm.
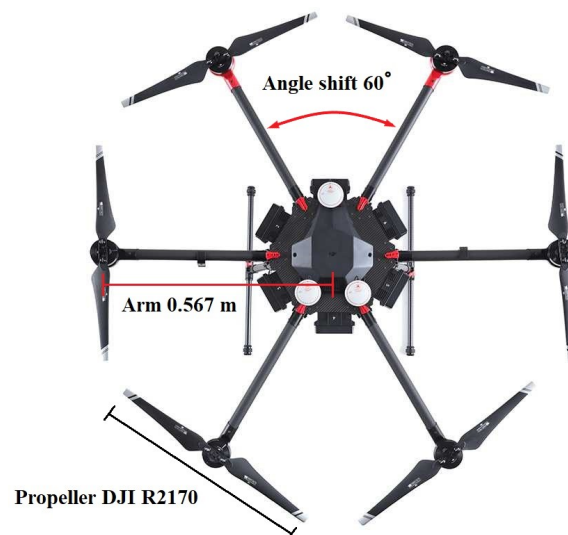
Figure 2.16: Hexacopter DJI M600 (top view)

In the open air measurements, the radar is configured to take full polarimetric measurements simultaneously at the single centre frequency f_c = 3.315 GHz with pulse repetition frequency PRF = 1 kHz. The dish

antennas with a beamwidth of 1.8° is elevated for 0.9° to avoid ground clutter. The drone is set 9 km away from the radar antennas, hovering steadily within the beamwidth (Figure 2.17 [8]), vertically above an empty field.

Figure 2.17: Location of PARSAX and drone

2.3.2. Micro-Doppler Pattern of Multi-Propeller Drone Measured by PARSAX

The signals measured by the PARSAX radar system are series of complex values in time domain[19]. At a given centre frequency of f_c = 3.315 GHz, the phase change of the complex signal series is due to the motion of the propeller target. In this experiment, the signal series is cut into sections of about 2 seconds in time containing about 2000 sampled signal values according to the PRF. Applying 256-point STFT to a piece of the signal section of complex values with 128 points overlapped gives the micro-Doppler pattern of the drone target in 2 seconds. Figure 2.18 gives the micro-Doppler pattern achieved by PARSAX over 2 seconds for example. In the figure, the achieved micro-Doppler pattern is first mapped into dB scale and rescaled between [0, 1] (Figures and images of drone micro-Doppler patterns in following chapters are shown in normalised dB scale in the same fashion).

In this circumstance, the micro-Doppler pattern of the multi-propeller drone is linear along the time axis, distributed over the Doppler frequency bandwidth, instead of periodic quasi-sinusoidal, because the CPI is 256 ms, corresponding to 256 sample points – given the relatively low radar PRF of 1 kHz – much longer than propeller rotation period, approximately 20 ms (several thousands of rotations per minute), and thus the periodic rotation details of the propellers are lost.

The multi-propeller drone of M600 hovering in the sky does not introduce a main Doppler frequency component other than zero frequency, and thus only the six rotating propellers contribute to the final micro-Doppler pattern. This is shown in the figure that the strong pattern at zero frequency is introduced by the drone main body and other stationary clutters, while the medium strong patterns distributed over the whole Doppler bandwidth from -500 Hz to 500 Hz correspond to the radial velocity components of the rotating
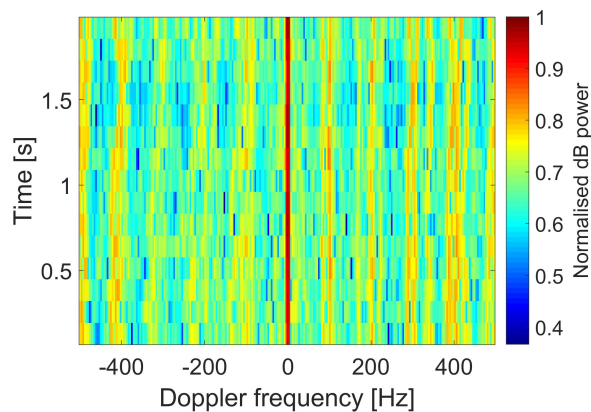
Figure 2.18: Micro-Doppler pattern of DJI M600 hexacopter measured by PARSAX

propellers. Besides, in the rescaled dB image of micro-Doppler pattern, the noise floor is about 0.7.

If the drone is manuevering instead of hovering stably, the micro-Doppler pattern should be different from the one shown in Figure 2.18. For a drone maneuvering radially along the LOS, the drone as a whole introduces a main Doppler frequency shift away from the zero frequency to the positive or negative direction. Besides, the patterns distributed over the Doppler frequency bandwidth should be more complicated, due to the fact that the asynchronous propeller rotation velocities which moves the drone introduce more velocity components than in the hovering circumstance. For a drone maneuvering tangentially towards the LOS, the main Doppler frequency shift would not be obvious, but the complication of Doppler patterns remain. If the drone has an acceleration, the micro-Doppler patterns do not appear vertical linear anymore, but with the slope corresponding to the change of velocity in a short time interval. However, the acceleration only lasts for a very short time when the drone starts migration, and thus is not of main interest in this work.

2.4. Conclusions

In this chapter, the RCS and micro-Doppler patterns of a single propeller and a multi-propeller drone are investigated. The RCS of a single propeller are achieved from DUCAT anechoic chamber and FEKO simulation. At S-band, apart from the global maxima at $\pm90°$, the RCS of propeller has local maxima, due to the constructive interference introduced by the geometry structure of the blade within the propeller. At S-band, the geometry size of the blades are much bigger than 1/2 wavelength, and thus only the global maxima at $\pm90°$.

Based on the RCS achieved in DUCAT measurements and FEKO simulation, the micro-Doppler pattern of a single propeller is calculated. In short CPI circumstance, the detail of the geometry structure of the propeller blade is clearly illustrated in the micro-Doppler pattern. In long CPI circumstance, the distribution of the linear micro-Doppler pattern does not reflect the geometry structure detail of the propeller blade.

The micro-Doppler pattern of multi-propeller drone is achieved from real radar measurement in the open air. In long CPI circumstance, the linear micro-Doppler pattern of the drone is the synthesis of that of the propellers', and for the drone hovering at the same place in the sky, the distribution of the micro-Doppler

pattern of the drone is the same as that of a single propeller, since all the propellers rotate synchronously in terms of rotation period.

The understanding of the EM reflection of the propeller and drone is used in the next chapter to develop a simple model in terms of RCS and micro-Doppler pattern.

3

Electromagnetic Wave Scattering Model and Radar Signal Model

3.1. Drone Structure and EM scattering

In commercial or recreational aerial field, quadcopter, hexacopter and octocopter are most widely used multi-propeller drones. All these types of drones consist of two main parts, body and propellers. Both body and propellers scatter radar signals. Perrforming STFT to the received by radar signal backscattered from the drone gives the Doppler pattern of the drone, describing the properties of the drone's motion, including the motion of the whole drone radially to the Tx/Rx antennas and the rotation of the propellers. For a drone that moves radially towards or away from radar, Doppler effect appears in EM signals scattered by the whole drone body, while micro-Doppler effect appears in EM signals scattered by the rotating propellers. For a drone that hovers in a specific place in the air, there exists only the micro-Doppler pattern introduced by the rotating propellers. For a drone that maneuvers in the horizontal plane, or rolls, yaws or pitches in a specific place in the air, due to the observation angles and the different rotation velocity of propellers, extra micro-Doppler components appear.

3.2. Simplified EM Model of Drone

In order to simulate and analyse the spectral, temporal and angular dependency of radar signals scattered from drone, we assume that the simplified EM model of drone is a combination of multiple propellers, each of which consists of several blades. The propellers are placed in specific positions according to the geometry size and structure of drone body.

Without loss of generality, we start with a drone that hovers in the same place in the air in the *XOY* hor-

izontal plane of radar. This model focuses on the phase of reflected signal and omits the magnitude factor, because phase factor contains propeller rotation information influencing final micro-Doppler patterns. Only horizontal-horizontal (HH) polarisation is considered in the model, since both the geometry and rotation of the propeller are most in horizontal plane.

In this case, there exists only micro-Doppler effect by rotating propellers, and elevation observation angle is 0 (see Figure 3.1). A simplified EM model illustrating the signal reflected from a single drone propellers is developed first in this chapter. A simplified EM model illustrating the signal reflected from a multi-propeller drone is proposed as the synthetic signal of the propeller reflected signals from multiple propellers. The EM models also include the factors of the centre frequency of the EM wave f_c and sampling frequency or radar PRF.
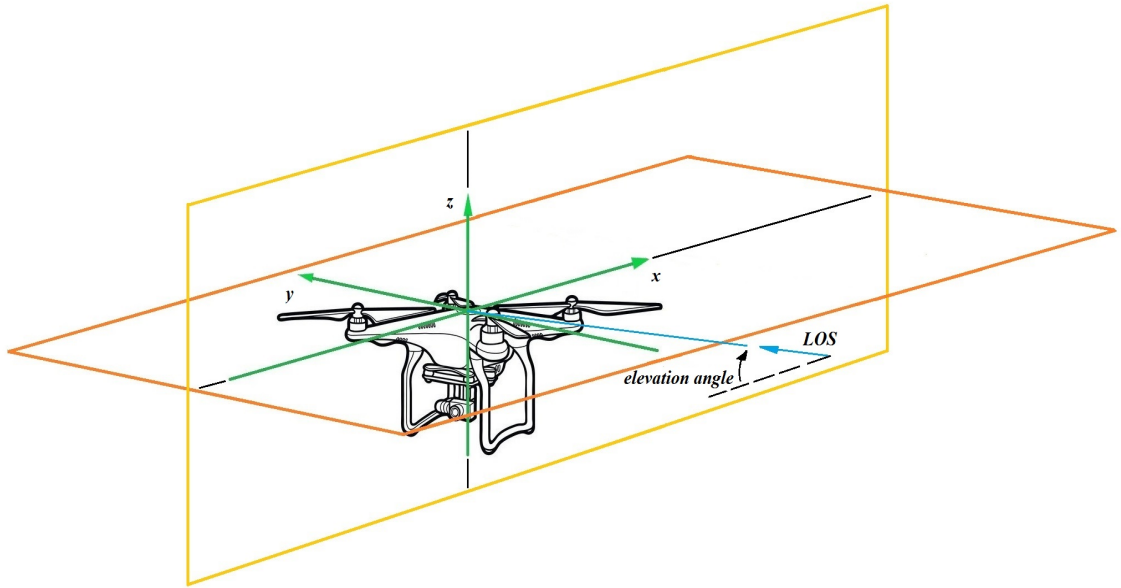
Figure 3.1: Geometry (3-D) of hovering drone in horizontal observation

3.2.1. Propeller Blade of Thin Wires

The basic approach to estimate the EM field scattered by a rotating blade is to assume that the blade can be modelled using very thin ($\varnothing \ll \lambda$) finite length linear wire [18]. In the spherical coordinate system, the electric field component scattered backwards by an infinitesimal dipole of length dy' positioned along the y-axis at y' (see Figure 3.2 [9]) in the far field is given as

$$dE^{infinitesimal}(\theta, y') \sim j\eta \frac{ke^{-jkr}}{4\pi r} E^{in}(r) \cdot \sin^2\theta \cdot e^{+j2ky'\cos\theta} dy' \tag{3.1}$$

where symbol $\sim$ indicates proportionality, paramteter θ is the observation angle in horizontal plane relative to the LOS or the observation point, $\eta = 120\pi$ is the intrinsic impedance of propagation medium in the air, $k = 2\pi/\lambda$ is wavenumber, and r is the distance from the centre of coordinates to the observation point. As the distance r is much greater than the geometry size of the blade, we assume observation angle θ stays the same

over the length of blade.

As the linear thin wire representing the propeller blade rotates around one of the endpoints, i.e. rotation centre, its angle relative to LOS is a function of time t. At any time point, the observation angle is given as

$$\theta(t) = \theta_w + \Omega t \tag{3.2}$$

where θ_w is original angle of blade wire with respect to LOS at zero time, and Ω is the rotation velocity of the blade thin wire.

Substituting Equation 3.2 into Equation 3.1 and integrating over y-axis, the electric field component scattered backwards by blade simplified as a single wire model at time t is given as

$$E^{wire}(t, r_w, \theta_w, l_w) \sim \int_0^{l_w} j\eta \frac{k e^{-jkr_w}}{4\pi r_w} E^{in}(r_w) \cdot \sin^2(\theta_w + \Omega t) \cdot e^{+j2ky' \cos(\theta_w + \Omega t)} dy' \tag{3.3}$$

where l_w is the length of the blade thin wire, and r_w is the rotation centre of the thin wire.
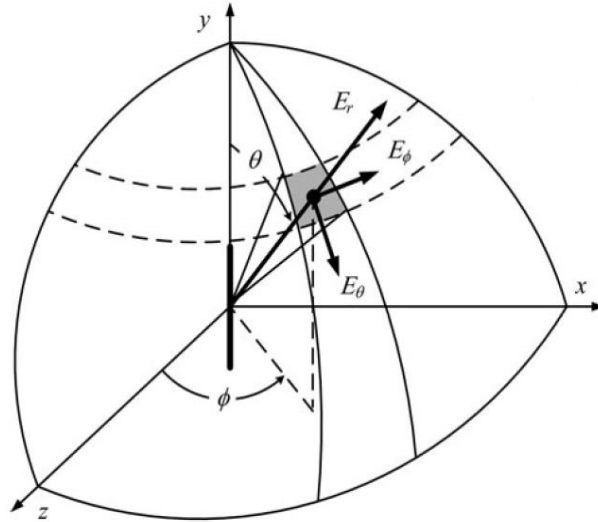
Figure 3.2: Coordinate of (3-D) of the electric field components scattered by infinitesimal dipole

In order to describe the geometry design of the blade structure more precisely, Krasnov et al. proposed to simplify the blade as a bunch of thin wires of decreasing length with some angle shift, instead of a single thin wire [18]. The backscattered EM field of a blade using multi-thin wire model is given as

$$
\begin{aligned}
E^{balde}(t, r_b, \theta_w, l_w) &\sim \sum_{w=1}^{W} E_w^{wire}(t, r_b, \theta_w, l_w) \\
&= \sum_{w=1}^{W} \int_0^{l_w} j\eta \frac{k e^{-jkr_b}}{4\pi r_b} \\
&\times E_{r_b}^{in}(t) \sin^2(\theta_{b,w} + \Omega t) \\
&\times e^{j2ky'_{b,w} \cos(\theta_{b,w} + \Omega t)} dy'_w
\end{aligned}
\tag{3.4}
$$

where r_b is the distance from the blade rotation centre to an observation point. W is the number of thin wires per blade in the simplified model, dy'_w is the length of infinitesimal dipole along the y-axis at the distance y'_w along the wth wire in the rotation plane. l_w is the length of the wth wire. In the same way as in Equation 3.2, the propeller rotates with the angular velocity Ω and all the angles of thin wires change in time linearly: $\theta(t) = \theta_w + \Omega t$, where θ_w is the initial angle of the wth wire relatively to the LOS at time $t = 0$. W, θ_w and l_w depend on the geometry design of blade.

3.2.2. Single Drone Propeller

A propeller is a combination of several blades which are progressively shifted by specific angle with respect to each other in the rotation plane. In the similar way as above, we assume the propeller can be modelled as a combination of multiple blades of several thin wires. In the spherical coordinate system, the electric field component scattered backwards by a propeller (see Figure 3.3. This propeller is a representative of most popular two-blade propellers, with each blade contains two thin wires.) in the far field at time t is given as

$$
\begin{aligned}
E^{prop}(t, r_p, \theta_{b,w}, l_{b,w}) &\sim \sum_{b=1}^{B} E_b^{blade}(t, r_p, \theta_{b,w}, l_{b,w}) \\
&= \sum_{b=1}^{B} \sum_{w=1}^{W} E_{b,w}^{wire}(t, r_p, \theta_{b,w}, l_{b,w}) \\
&= \sum_{b=1}^{B} \sum_{w=1}^{W} \int_0^{l_{b,w}} j\eta \frac{ke^{-jkr_p}}{4\pi r_p} \\
&\quad \times E_{r_p}^{in}(t) \sin^2(\theta_{b,w} + \Omega t) \\
&\quad \times e^{j2ky'_{b,w} cos(\theta_{b,w} + \Omega t)} dy'_{b,w}
\end{aligned}
\tag{3.5}
$$

where r_p is the distance from propeller rotation centre to an observation point. B is the number of blades per propeller, W is the number of thin wires per blade in the simplified model, $dy'_{b,w}$ is the length of infinitesimal dipole along the y-axis at the distance $y'_{b,w}$ along the wth wire of the bth blade in the rotation plane. $l_{b,w}$ is the length of the wth wire of the bth blade, $\theta_{b,w}$ is the initial angle of the wth wire of the bth blade relatively to the LOS at time $t = 0$. W, $\theta_{b,w}$ and $l_{b,w}$ depend on the geometry design of the propeller.

3.2.3. Drone of Multiple Propellers and Azimuth Observation Angle

The EM model of drone is a combination of EM models of several propellers. As the drone hovers in the horizontal plane of radar, the drone body does not introduce Doppler effect, and thus only electric signals scattered by propellers should be modelled. However the geometry size of drone body determines the positions of propellers respect to each other. The electric field component scattered by a drone of multiple
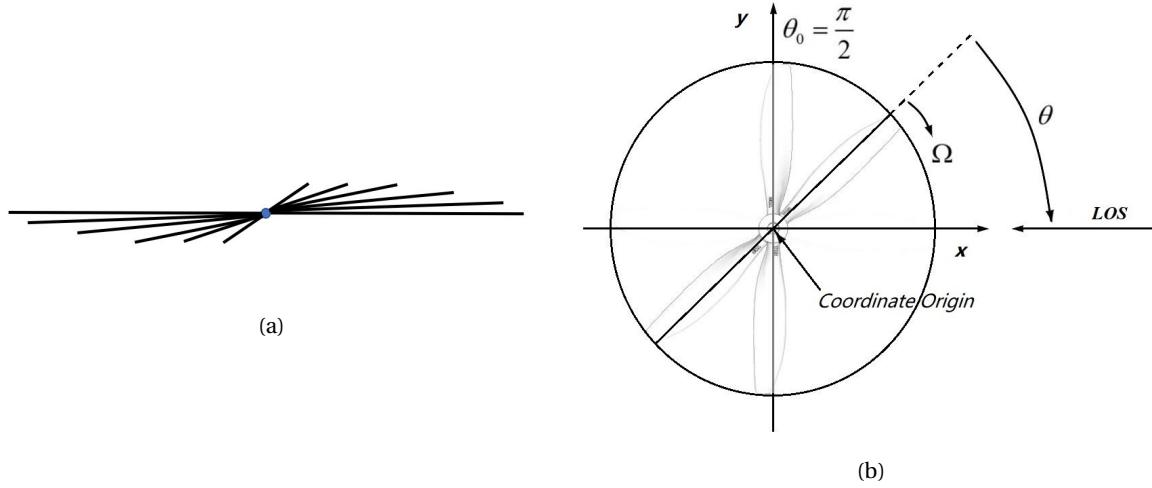
Figure 3.3: Coordinate (in horizontal plane) of the electric field components scattered by propeller: (a) geometry detail of propeller thin-wire model, (b)coordinate of propeller model

rotating propellers (see Figure 3.4. A drone of four propellers is shown as example.) in the far field is given as

$$
\begin{aligned}
E^{drone}(t,r_0) &\sim \sum_{p=1}^{P} E_p^{prop}(t,r_p,\theta_{p,b,w},l_{p,b,w}) \\
&= \sum_{p=1}^{P}\sum_{b=1}^{B}\sum_{w=1}^{W} E_{p,b,w}^{wire}(t,r_p,\theta_{p,b,w},l_{p,b,w}) \\
&= \sum_{p=1}^{P}\sum_{b=1}^{B}\sum_{w=1}^{W} \int_0^{l_{p,b,w}} j\eta \frac{ke^{-jkr_p}}{4\pi r_p} \\
&\quad \times E_{r_0}^{in}(t)\sin^2(\theta_{p,b,w}+\Omega_p t) \\
&\quad \times e^{j2ky'_{p,b,w}cos(\theta_{p,b,w}+\Omega_p t)} dy'_{p,b,w} \\
&= \sum_{p=1}^{P} j\eta \frac{ke^{-jkr_p}}{4\pi r_p} \cdot E^{propeller}
\end{aligned}
\tag{3.6}
$$

where most symbols and variables are defined the same as in Eq. (3.5). In this equation $dy'_{p,b,w}$, $l_{p,b,w}$ and $\theta_{p,b,w}$ are specified for each of P propellers. The last equality step indicates that the backscattered signal from the propeller is the synthesis of that from multiple propellers, but with an extra phase shift and a slight difference in amplitude dues to the radial distance between the drone's geometry centre and the propellers' rotation centres.

Indexed parameters Ω_p and r_p make Eq. (3.6) different from Eq. (3.5). Parameter Ω_p is the rotation velocity of pth propeller. When the drone makes any maneuver, propellers become asynchronous in velocity, and Ω_ps of the propellers are not the same anymore. r_p is the radial range from the pth propeller rotation centre to observation point. If we define within drone's geometry design some centre point O with the distance r_0 to the remote observation point and some reference axis (see Fig.3.4), we can relate the radial distances r_p to the drone distance r_0, the drone observation angle α_0 in horizontal plane and the geometrical structure of multi-propeller drone

$$
r_p = r_0 - d_p \cdot cos(\alpha_p - \alpha_0).
\tag{3.7}
$$
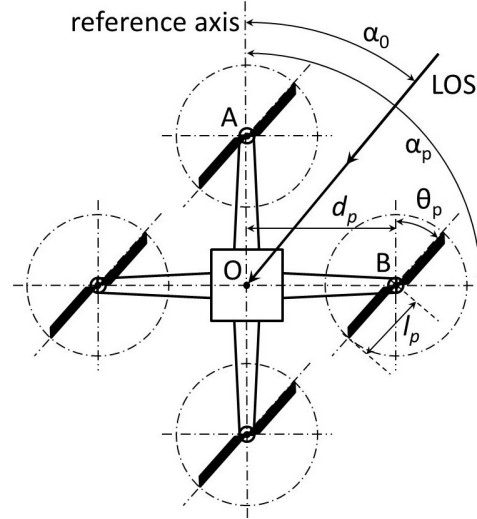
Figure 3.4: Geometrical design and coordinate (in horizontal plane) of a quadcopter as an example of multi-propeller drone

Here d_p is the length from the rotation centre of the pth propeller to drone centre determined by the geometry design of the drone, α_0 is the angle between drone's reference axis and LOS, and α_p is the angle between the pth propeller arm OB and reference axis. Reference axis is set at the first propeller arm OA in this example. The distance between drone centre and propeller centre is considered in this model, because it introduces additional phase shift to scattered EM signal. Besides, to make the figure clear, in Fig.3.4, only the start angle and length of the major wire of the pth propeller's first blade are shown as θ_p and l_p. Details of each simplified propeller are the same as in Eq.(3.5).

3.3. Radar Signal Model and Micro-Doppler Spectrum

3.3.1. A Single Rotating Thin Wire

The micro-Doppler pattern of the model-based simulated drone can be achieved by applying sliding-windowed STFT to a generated EM signal time series of several seconds with some points overlapped. This performance of Fourier transform [22] processes a signal series of real or complex values in time domain and results in the signal series' spectrum in frequency domain. In this spectrum, the frequency components introduced by the target motion appear as peaks. For a multiple propeller model proposed above in this chapter, the frequency components correspond to the rotation of the propellers.

The electric field component scattered backwards by a single thin wire at time t is given in previous sections as Equation 3.3. This equation as a function of time t can be rewritten after integration as

$$E^{wire}(t) \sim j\eta \frac{ke^{-jkr_w}}{4\pi r_w} E^{in}(r_w) \cdot \sin^2(\theta_w + \Omega t) \cdot \frac{e^{+j2kl_w \cos(\theta_w + \Omega t)} - 1}{j2k\cos(\theta_w + \Omega t)}. \tag{3.8}$$

In real radar system, the baseband discrete electric backscattered signal as a function of sampling point n

is given as

$$s^{wire}[n] \sim \frac{\eta e^{-j\frac{2\pi}{\lambda}r_w}}{8\pi r_w} \cdot \frac{\sin^2(\theta_w + \Omega t_s n)}{\cos(\theta_w + \Omega t_s n)} \cdot (e^{+j2\frac{2\pi}{\lambda}l_w \cos(\theta_w + \Omega t_s n)} - 1) \tag{3.9}$$

where n is the index of the sampled signal point. Parameter t_s is the time sampling period.

Replacing the exponential as the sum of a bunch of Bessel functions (see Equations (12)-(13) in [18]), the Equation 3.9 can be rewritten as

$$s^{wire}[n] \sim \frac{\eta e^{-j\frac{2\pi}{\lambda}r_w}}{8\pi r_w} \cdot \frac{\sin^2(\theta_w + \Omega t_s n)}{\cos(\theta_w + \Omega t_s n)} \cdot \left(\sum_{q=-\infty}^{\infty} e^{j\frac{\pi q}{2}} J_q(2\frac{2\pi}{\lambda}l_w) e^{j(\theta_w + \Omega t_s n)q} - 1\right) \tag{3.10}$$

where symbol J_q indicates the qth order Bessel function, and parameter q is integer over $(-\infty, \infty)$, also known as the harmonic's order. In this form, the signal $s^{wire}[n]$ at each sampled time is the superimposition of the harmonic components with frequencies that are proportional to the propeller's angular rotation frequency of $q\Omega$. The amplitude of each harmonic component is determined by the corresponding Bessel function J_q. An extra amplitude modulation is applied to the 1st harmonic component at the angular frequency of Ω by the second term of $\frac{\sin^2(\theta_w + \Omega t_s n)}{\cos(\theta_w + \Omega t_s n)}$.

Figure 3.5 gives an example of the amplitude of the harmonic component determined by the Bessel function $J_q(Z)$. This figure gives an intuitive illustration of the harmonic amplitude modulation. In this example, given the input values of the Bessel functions $Z = 1$, the values of the Bessel functions decreases, as the harmonic order increases, while in reality, the values of the Bessel functions are determined by the variable of $2\frac{2\pi}{\lambda}l_w$.

By applying Discrete Fourier Transform (DFT) to a section of the signal over the time of a single CPI given in Equation 3.9, the micro-Doppler spectrum of the signal section as a function of CPI is given as

$$\begin{aligned} S^{wire}[m] &= \mathscr{F}\{s^{wire}[n]\} \\ &\sim \sum_{n=0}^{N-1} s^{wire}[n] \cdot e^{-j\frac{2\pi}{N}nm} \\ &= \sum_{n=0}^{N-1} \frac{\eta e^{-j\frac{2\pi}{\lambda}r_w}}{8\pi r_w} \cdot \frac{\sin^2(\theta_w + \Omega t_s n)}{\cos(\theta_w + \Omega t_s n)} \cdot \left(\sum_{q=-\infty}^{\infty} e^{j\frac{\pi q}{2}} J_q(2\frac{2\pi}{\lambda}l_w) e^{j(\theta_w + \Omega t_s n)q} - 1\right) \cdot e^{-j\frac{2\pi}{N}nm} \\ &= \sum_{n=0}^{N-1} \frac{\eta e^{-j\frac{2\pi}{\lambda}r_w}}{8\pi r_w} \cdot \frac{\sin^2(\theta_w + \frac{2\pi}{N_{rot}}n)}{\cos(\theta_w + \frac{2\pi}{N_{rot}}n)} \cdot \left(\sum_{q=-\infty}^{\infty} e^{j\frac{\pi q}{2}} J_q(2\frac{2\pi}{\lambda}l_w) e^{j(\theta_w + \frac{2\pi}{N_{rot}}n)q} - 1\right) \cdot e^{-j\frac{2\pi}{N}nm} \\ m &= 0, 1, ..., N-1 \end{aligned} \tag{3.11}$$

where symbol $\mathscr{F}$ indicates the Fourier Transform. Parameter N is the number of sampled points of the signal within a single CPI, and parameter $N_{rot} = \frac{2\pi}{\Omega t_s}$ is the number of sampled points of the signal within a rotation period.

Equation 3.11 illustrates that, for a given rotating thin wire of specific length, the micro-Doppler spectrum is a function of the CPI length in terms of the number of sampled signal points N, of the original angle of the thin wire θ_w, and of the angular rotation velocity of the thin wire Ω, or, in other terms, of the number of sam-
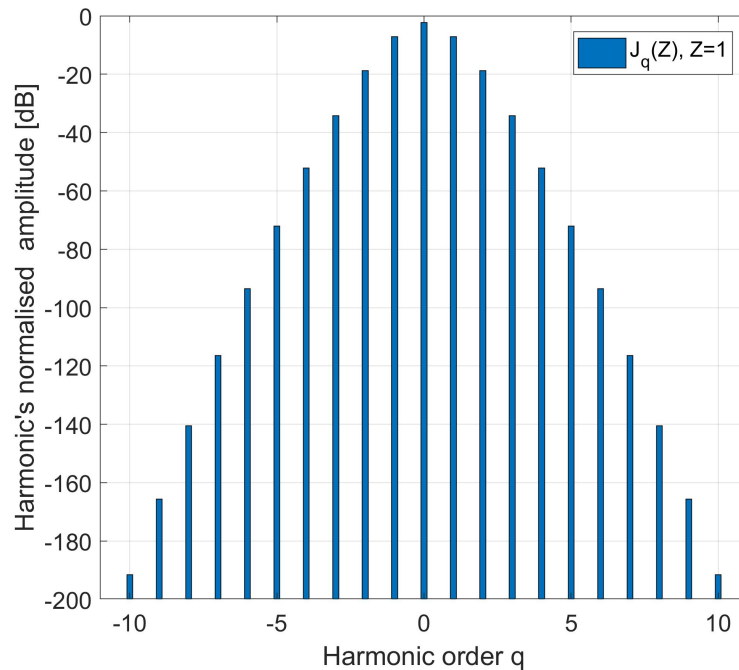
Figure 3.5: The amplitude of the harmonic component as a function of the harmonic order $J_q(Z)$ (see Eq.3.10). The first harmonic components with normalised amplitude above -200 dB are given as examples.

pled signal points N_{rot} during one rotation period. The intuitive interpretation of the micro-Doppler spectrum is given as follows. This spectrum is a superimposition of multiple harmonic frequency components appearing at different frequencies that are separated with the gap equals to the angular rotation velocity of the thin wire Ω. The amplitude or power of the harmonic frequency components are modulated by the Bessel functions, with an extra amplitude modulation performed on the 1st order harmonic frequency component by the $\sin^2/\cos$ terms.

3.3.2. Periodic Flushes and Linear Spectral Patterns

It is shown in Equation 3.11 that the micro-Doppler pattern is influenced by the relation between the radar CPI and the thin wire rotation frequency in terms of the number of sampled signal points N and N_{rot}. Initially this influence has been demonstarted in [18] with application to wind turbines radar observation. For the drones this two situations of $N \ll N_{rot}$ and $N \gg N_{rot}$, i.e. $CPI \ll 1/\Omega$ and $CPI \gg 1/\Omega$ are discussed below.

If $N \ll N_{rot}$, the coherent processing over a CPI only spreads over a small portion of the rotation period, and the radial rotation velocity is clearly estimated at this time point. In this situation, the superimposition of the amplitude modulated harmonic frequency components reduces into a sinusoidal function in the time-frequency representation whose amplitude or power periodically oscillates as time goes by. If $N \gg N_{rot}$, the coherent processing over a CPI covers across several rotation periods, and the radial rotation velocity at each time point cannot be estimated anymore. In this situation, the superimposition of the amplitude modulated harmonic frequency components stays separate with the gap that equals to the angular rotation velocity Ω. Figure 3.6 gives examples of the micro-Doppler patterns of a rotating thin wire over several CPI's as a function

of the relation between the radar CPI and rotation period $T_{rot} = 1/\Omega$. In following sections, a special attention is paid to the long CPI circumstances where $CPI \gg 1/\Omega$.
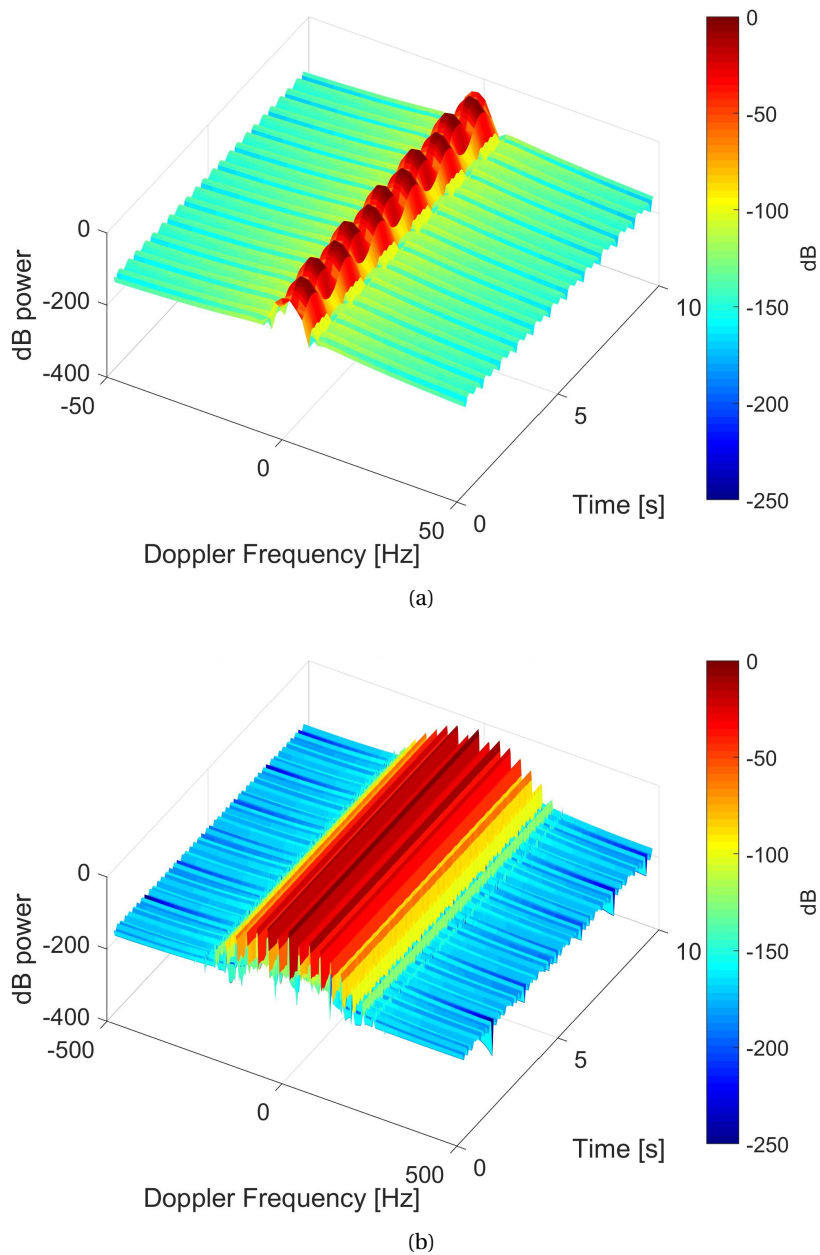
Figure 3.6: The micro-Doppler patterns of rotating thin wires as a function of the relation between the radar CPI and rotation period $T_{rot} = 1/\Omega$. Calculated for following parameters: PRF = 1 kHz, f_c = 0.06 GHz, l_w = 1 m. (a) CPI = 0.512 s, T_{rot} = 1.67 s (Only part of the Doppler frequency bandwidth where the micro-Doppler pattern appear is zoomed in for readability.), (b) CPI = 0.512 s, T_{rot} = 0.03 s

3.3.3. Multiple Rotating Thin Wires

As discussed in the previous sections, the thin-wire models of the blade, the propeller and the multi-propeller drone are all combinations of the basic thin wire models on different layers, and their backscattered electric signals are the synthesis of those of a single rotating thin wire. As a result, the micro-Doppler spectrum of a

multi-propeller drone achieved from the DFT within a single CPI is given as

$$
\begin{aligned}
S^{drone}[m] &= \mathscr{F}\{s^{drone}[n]\} \\
&\sim \sum_{n=0}^{N-1}(\sum_{p=1}^{P}\sum_{b=1}^{B}\sum_{w=1}^{W} s_{p,b,w}^{wire}[n]) \cdot e^{-j\frac{2\pi}{N}nm} \\
&= \sum_{n=0}^{N-1}(\sum_{p=1}^{P}\sum_{b=1}^{B}\sum_{w=1}^{W} \frac{\eta e^{-j\frac{2\pi}{\lambda}r_p}}{8\pi r_p} \cdot \frac{\sin^2(\theta_{p,b,w}+\Omega_p t_s n)}{\cos(\theta_{p,b,w}+\Omega_p t_s n)} \\
&\quad \cdot (\sum_{q=-\infty}^{\infty} e^{j\frac{\pi q}{2}} J_q(2\frac{2\pi}{\lambda}l_{p,b,w})e^{j(\theta_{p,b,w}+\Omega_p t_s n)q}-1)) \cdot e^{-j\frac{2\pi}{N}nm} \\
m &= 0,1,...,N-1
\end{aligned}
\tag{3.12}
$$

where all the symbols and parameters are defined as in previous sections. Equation 3.12 indicates the micro-Doppler spectrum of drone is similar to that of a single rotating thin wire, however, the location of the propeller rotation centres determined by the geometry structure design of the drone, the synchronisation of the propeller in angle and angular velocity, and the length of the blade thin wires introduce complexity to the synthetic micro-Doppler pattern.

3.4. Validation of Thin-Wire Model in RCS and Micro-Doppler Pattern

In order to validate the thin-wire model proposed in previous chapters, the RCS and micro-Doppler pattern of the propeller based on the thin-wire model are generated and compared with the results achieved from DUCAT measurement and FEKO simulation.

Figure 3.7: Simplified Thin-Wire Model of DJI 2170 propeller

To apply the precious proposed simplified thin-wire model to the DJI R2170 propeller, each blade of the propeller is represented as two thin wires, according to the blade geometry. The two thin wires are of 0.267 m and 0.253 m in length and 10° shifted in angle (Figure 3.7). Signal series of 10,000 complex values at specific frequencies of 10 GHz and 3.315 GHz are generated from the thin-wire radar signal model, assuming the propeller rotating from -180° to 180°. Figure 3.8 shows the RCS of the propeller at X-band (10GHz) and S-band (3 GHz). The RCS is the synthesis of the RCS of the two single wires. Since the simplified model only has two thin wires, there are only two maxima at 90 degrees and 100 degrees. The two thin-wire model reproduces the global maxima in DUCAT measured (Fig. 2.6) and FEKO simulated (Fig.2.10) propeller's RCS, but details related to local maxima are lost due to the simplicity of the model.

We can improve this simulation similarity to the measured and 3D-simulated dependency by the increasing of thin-wire model complexity. For example, adding two additional wires into the model as in Figure 3.9 that represent the edges of the real propeller (see Figure 2.8), the simulation results in RCS dependence that
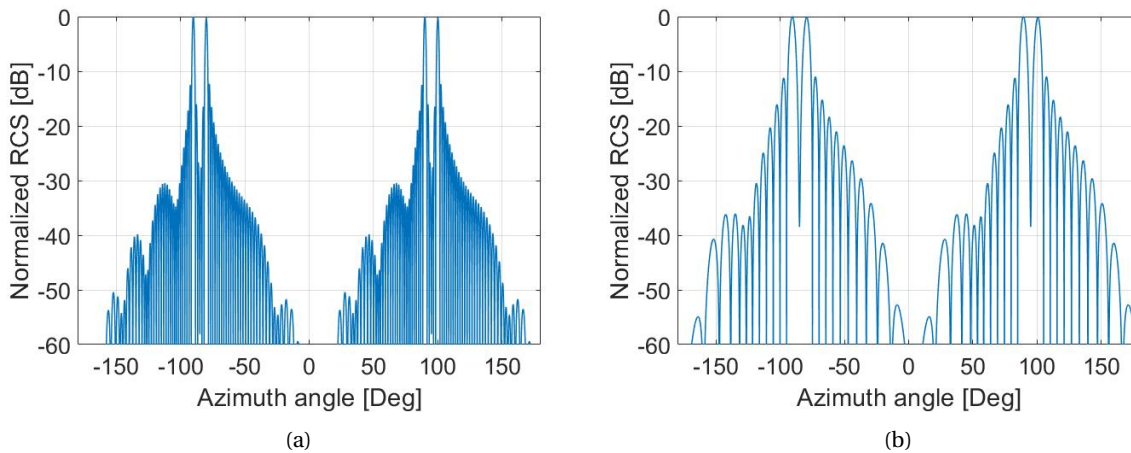
Figure 3.8: Simulated RCS of DJI R2170 propeller based-on the thin-wire model at specific frequencies: (a) 10 GHz, (b) 3.315 GHz

presented in Figure **??** reproduces more details of the local maxima at 35° and 165° in previously presented experimental and 3D-simulated RCS curves, especially at S-band (3 GHz).
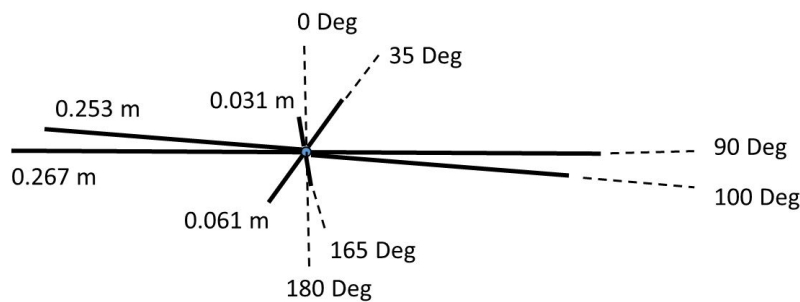
Figure 3.9: Simplified Thin-Wire Model of DJI 2170 propeller of more thin wires

The model-based micro-Doppler patterns are simulated by applying 1,024-point STFT to the model-generated series with 896 points overlapped. These variable setup combinations of propeller rotation angular velocity, radar centre frequency, PRF and CPI are the same as in the EM anechoic chamber measurements.

Figure 3.11 presents the simulated micro-Doppler patterns of the rotating propeller thin-wire model during the half of rotation period at 10 GHz and 3.315 GHz for the case when this rotation period is much longer that the CPI. The comparison of the DJI R2170 propeller's micro-Doppler patterns that are based on the simplified thin-wire model in Figure 3.11 and on the anechoic chamber measurements in Figure 2.13 with the same setup variables shows that they look quite similar. The geometry structure of the blades of the major and minor fringes are well reproduced in the simulated model-based patterns, reconfirming that the representation of the blade with a few thin-wires are valid in this circumstances. In Figure 3.11, the micro-Doppler patterns are invisible from the background when the propeller blades are approximately perpendicular to the LOS, because in the analytical model the computed backscattered signals are quite small at these moments. In Figure 2.13, the flashing micro-Doppler patterns are clearly visible due to the good dynamic range of the experimental equipment: the anechoic chamber background is below -50 dB, while the amplitude of
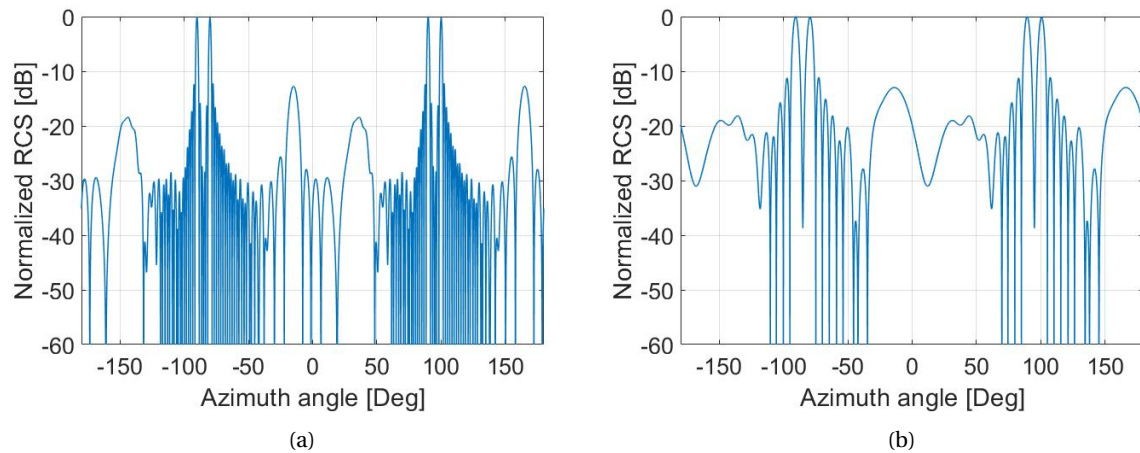
Figure 3.10: Simulated RCS of DJI R2170 propeller based-on the thin-wire model of 4 wires at specific frequencies: (a) 10 GHz, (b) 3.315 GHz

scattered by propeller signals are between -40 dB and -10 dB .
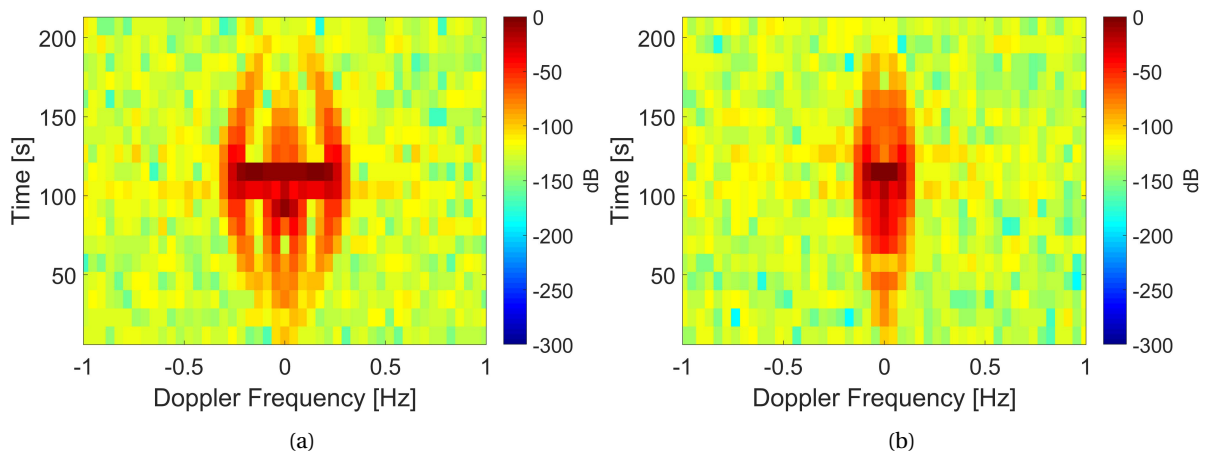
Figure 3.11: Micro-Doppler pattern of DJI 2170 propeller based on simplified thin-wire model at specific frequencies: (a) 10 GHz, (b) 3.315 GHz

Figure 3.12 gives the micro-Doppler pattern of the rotating propeller based on the thin-wire model at X-band and S-band. The comparison of the micro-Doppler pattern of the rotating propeller based on the DUCAT measurements (see Figure 2.14) and thin-wire model (see Figure 3.12) at X-band and S-band indicates that in the long CPI circumstance, the micro-Doppler pattern based on the thin-wire model does not suffer from the simplicity of the model or the loss of the detail of the geometry structure of the propeller, and well reproduce the micro-Doppler pattern measured in DUCAT anechoic chamber.

Overall, the thin-wire model reproduces valid micro-Doppler patterns at X-band and S-band, given specific variables of propeller properties and radar setups. In short CPI circumstances, the thin-wire model based simulated micro-Doppler pattern does not exactly reproduce the measured pattern in detail, due to its simplicity, but in long CPI circumstances, the micro-Doppler pattern simulated by the thin-wire model well reproduce the measured results.
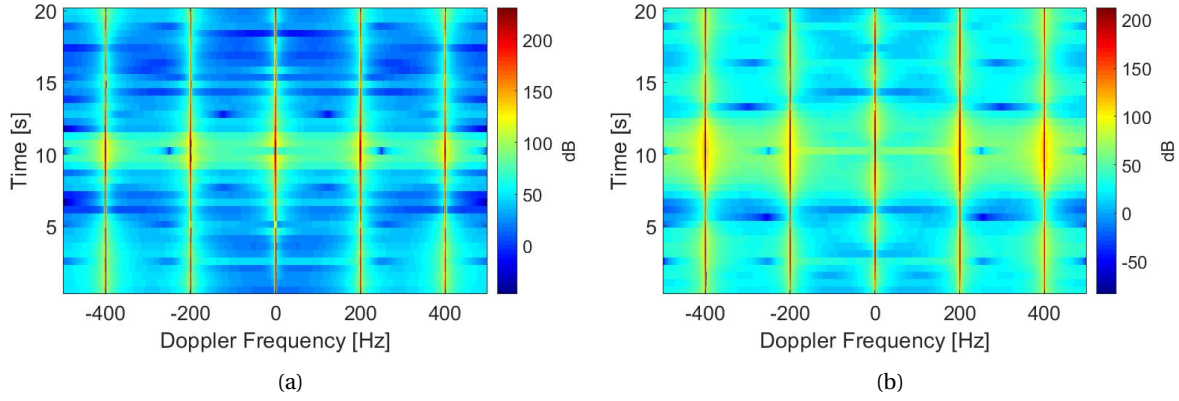
Figure 3.12: Micro-Doppler patterns of DJI 2170 propeller based on simplified thin-wire model at specific frequencies in long CPI circumstance: (a) 10 GHz, (b) 3.315 GHz

3.4.1. Micro-Doppler Pattern of Multi-Propeller Drone Based on Thin-Wire Model

In order to validate the thin-wire model of multi-propeller drones, the model is introduced here representing the hexacopter of DJI M600. The micro-Doppler patterns of the multi-propeller drone based on the thin-wire model should lead to the reflection signals which the reproduction of the micro-Doppler pattern achieved from the open air experiment measured by PARSAX radar system can be performed from.

To apply the simplified thin-wire model of multi-propeller drone to the DJI M600 hexacopter, each propeller is represented with thin wires in the same way as in previous sections, because the propellers occupied by DJI M600 are DJI R2170, exactly the one modelled before. The geometry design of the whole drone is considered here, and the specs of the drone geometry is illustrated in Figure 2.16.

A signal series of complex values is generated from the thin-wire model of DJI M600 hexacopter over the time of 2 seconds, given the same variables of radar setup in terms of PRF, centre frequency, etc, as in the above PARSAX open air measurement. In this model-based simulation, the drone is assumed to be hovering, thus with propellers synchronous in rotation velocity. Moreover, since in linear micro-Doppler pattern circumstance of low radar PRF and long CPI, the detail of propeller rotation is not clearly tracked anymore and the object of the model simulation here is to validate the model-based data of micro-Doppler pattern in general, without the loss of generality, the propellers are assumed of the same angle relative to LOS in the horizontal plane for simplicity.

Applying Doppler processing with exactly the same parameters of CPI, number of STFT points and overlap ration to the thin-wire model-generated complex signal series, the simulated micro-Doppler pattern of DJI M600 hexacopter is shown in Figure 3.13. In the same style as above, the achieved micro-Doppler pattern is first mapped into dB scale followed by rescaling between $[0, 1]$.

By the comparison between Figure 2.18 and Figure 3.13, the frequency resolution, temporal stability and SNR of the micro-Doppler pattern in the latter simulated from the thin-wire model are better than those in the first measured by PARSAX radar in open air. Possible reasons for these differences are the limited dynamic range of radar system and the far distance, the noise in the environment and the disturbance of the exact location and stable state of the hovering drone by the airflow. Besides, the main reflection at zero frequency
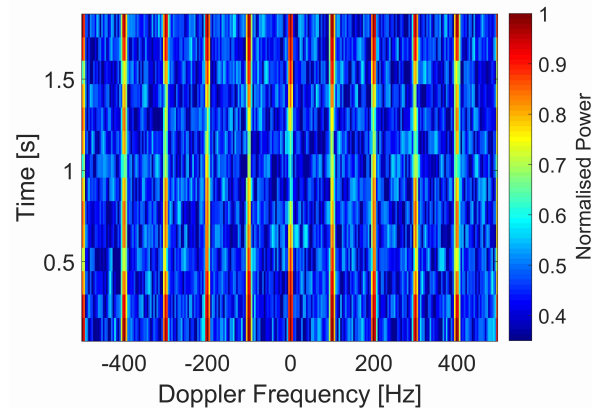
Figure 3.13: Micro-Doppler pattern of DJI M600 hexacopter simulated by thin-wire model

does not appear in 3.13, because in the simplified thin-wire model generates the backscattered EM signals of the multi-propeller drone as the synthesis of the signals backscattered from all the propellers, thus only leads to the Doppler frequency components corresponding to propeller rotation.

Overall, the linear micro-Doppler pattern based on the thin-wire model of multi-propeller drone well reproduces real data of micro-Doppler pattern achieved from S-band radar system in long CPI circumstances, in terms of the distribution of linear patterns over the Doppler bandwidth.

3.5. Conclusions

This chapter develops the EM wave scattering model and radar signal model of a multi-propeller drone. In the EM scattering model, the drone is simplified as a combination of thin wires. In the radar signal model, the phase shift in the signal scattered back from the drone is proposed as a function of the geometry structure design of the drone and the angle of the propeller blades changing in time. The radar signal model of the drone is a synthesis of the radar signal model of multiple propellers, with an extra phase shift and a negligible amplitude difference due to the radial distance between the drone's geometry centre and the rotation centre of the propellers. The radar signal reflected from a multi-propeller drone is the synthesis of that from the propellers, but with an extra phase shift and a negligible amplitude difference due to the difference between the drone's geometry centre and the propeller's rotation centre.

The micro-Doppler pattern of the drone is achieved by performing STFT on a series of the radar signal points over time. The micro-Doppler pattern may be periodic or linear, given CPI less or greater than the rotation period of the rotating propellers. In the long CPI circumstances, the angle shift between the propellers do not influence the micro-Doppler pattern much.

The thin-wire models of a single propeller and a drone are validated with the DUCAT measurements, FEKO simulations and open air radar measurements, in terms of RCS and micro-Doppler pattern. In short CPI circumstances, the accuracy of the achieved micro-Doppler pattern in detail depends on the complexity of the geometry structure in the EM wave scattering model. In long CPI circumstances, the geometry structure detail of the propeller do not influence the distribution of the micro-Doppler pattern very much, and

thus the thin-wire model gives good reproduction of measured pattern.

In the next chapter, the micro-Doppler pattern simulated from the model is analysed, and suitable features are proposed to characterise the micro-Doppler pattern.

$$4$$

Feature Proposal and Drone Classification

4.1. Analysis of Micro-Doppler Patterns

The micro-Doppler pattern simulation model is developed and validated in previous chapters. In this section, an analysis is performed on the model-simulated micro-Doppler pattern of a rotating thin wire, in order to investigate the influence of various factors on the micro-Doppler pattern. Then the analysis is expanded to multiple rotating thin wire situation. In these simulations and analysis, a special attention is paid to the linear micro-Doppler pattern in the long CPI circumstances where $CPI \gg \frac{1}{\Omega}$.

For convenience, the micro-Doppler spectrum of a rotating thin wire achieved by DFT is copied from the previous chapters as (see Equation 3.11)

$$
\begin{aligned}
S^{wire}[m] &= \mathcal{F}\{s^{wire}[n]\} \\
&\sim \sum_{n=0}^{N-1} s^{wire}[n] \cdot e^{-j\frac{2\pi}{N}nm} \\
&= \sum_{n=0}^{N-1} \frac{\eta e^{-j\frac{2\pi}{\lambda}r_w}}{8\pi r_w} \cdot \frac{\sin^2(\theta_w + \Omega t_s n)}{\cos(\theta_w + \Omega t_s n)} \cdot \left(\sum_{q=-\infty}^{\infty} e^{j\frac{\pi q}{2}} J_q(2\frac{2\pi}{\lambda}l_w) e^{j(\theta_w + \Omega t_s n)q} - 1 \right) \cdot e^{-j\frac{2\pi}{N}nm} \\
&= \sum_{n=0}^{N-1} \frac{\eta e^{-j\frac{2\pi}{\lambda}r_w}}{8\pi r_w} \cdot \frac{\sin^2(\theta_w + \frac{2\pi}{N_{rot}}n)}{\cos(\theta_w + \frac{2\pi}{N_{rot}}n)} \cdot \left(\sum_{q=-\infty}^{\infty} e^{j\frac{\pi q}{2}} J_q(2\frac{2\pi}{\lambda}l_w) e^{j(\theta_w + \frac{2\pi}{N_{rot}}n)q} - 1 \right) \cdot e^{-j\frac{2\pi}{N}nm}
\end{aligned}
\tag{4.1}
$$

$$m = 0, 1, ..., N-1$$

4.1.1. Amplitude Modulation

In the long CPI circumstances, the micro-Doppler patterns of a rotating thin wire is a combination of the harmonic frequency components. As discussed in previous Chapters2 and shown in Equation 4.1, the amplitude of the harmonic frequency components is influenced by the Bessel functions taking the wavelength λ of the

EM signal and the length of the thin wire l_w as inputs. Besides, an extra amplitude modulation is performed on the 1st order harmonic frequency component. Figure 4.1 gives an example of the micro-Doppler spectrum influenced by the amplitude modulation.

The comparison between the subfigures shows that given all the other simulation variables the same, changing only the wavelength λ (carrier centre frequency) and the length of the thin wire 1^s, the amplitudes of the harmonic frequency components changes as well. As the input of the Bessel functions $J_q(2\frac{2\pi}{\lambda}l_w)$ changes, the amplitude of each harmonic frequency component changes, while the frequency of the harmonic components stay at the same frequency point on the Doppler frequency axis. It should be noticed that given some input value, the values of the harmonic components at some specific orders decreases much that can hardly be visible anymore. This indicates the invisibility of some linear patterns in the micro-Doppler patterns, especially in the noisy circumstances. Besides, there is an extra amplitude modulation introduced by the second term in Equation 4.1.

4.1.2. The Influence of Rotation Period

Equation 4.1 indicates that the angular rotation velocity (rotation period) of the thin wire influences two properties of the micro-Doppler spectrum – The distribution of the harmonic components over the Doppler frequency axis and an extra amplitude modulation on the 1st order harmonic component. Figure 4.2 gives an example of the micro-Doppler spectrum influenced by the angular rotation velocity.

It is shown by the comparison between the subfigures that, given all the other simulation variables the same, the frequency distribution of the harmonic components is determined by the angular rotation velocity – The gap between neighbouring harmonic components along the Doppler frequency is exactly the thin wire's rotation frequency, which agrees with the physical facts.

4.1.3. The Influence of Radar PRF

In Equation 4.1, the sampling time is equal to the radar PRI $t_s = PRI$, and the sampling frequency f_s is just the radar PRF. In previous examples and discussions on the micro-Doppler spectrum, all the visible harmonic components spread within the Doppler frequency bandwidth determined by $\pm\frac{PRF}{2}$. In the cases when the high-order harmonic components appears beyond the PRF-determined Doppler frequency axis interval, aliasing/folding phenomenon happens to the high-order harmonic components, introducing the Doppler ambiguity. Figure 4.3 gives an example of the micro-Doppler spectrum of a rotating thin wire observed at different radar PRF's. In Figure 4.3b, the red dashed line illustrates the aliasing/folding, while the blue line is the final observed micro-Doppler spectrum..

Figure 4.3 illustrates that a higher radar PRF enables the higher order harmonic components in the micro-Doppler spectrum without aliasing/folding. However, in some cases with aliasing/folding, it is possible to observe the high order harmonic components, and these folded harmonic components follows the rules of amplitude modulation by the Bessel functions and the frequency gap determined by the angular rotation velocity.
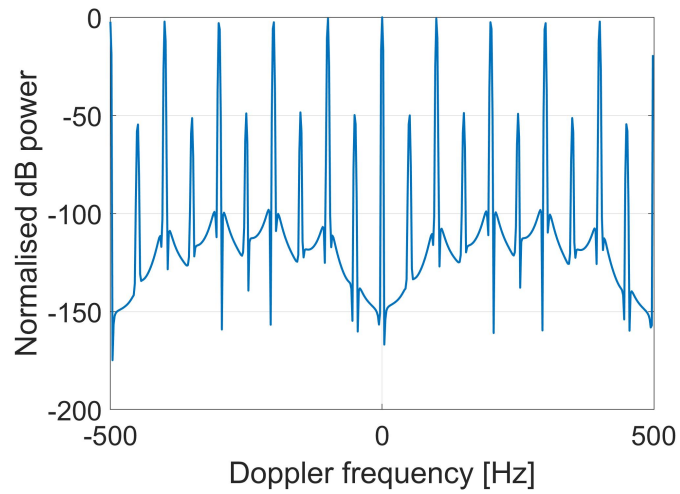
(a)
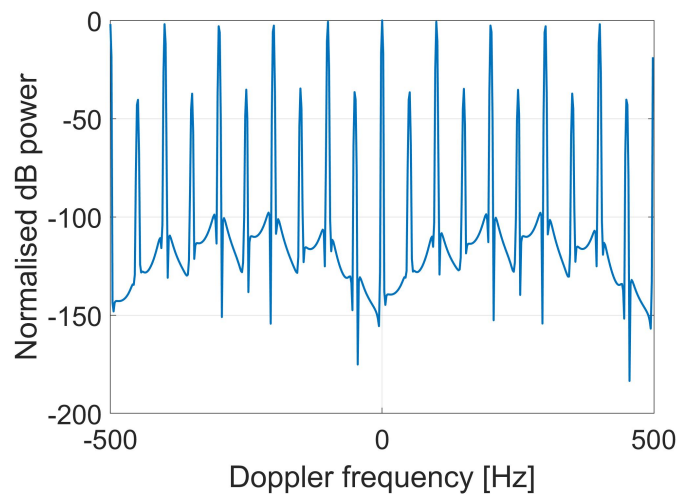
(b)
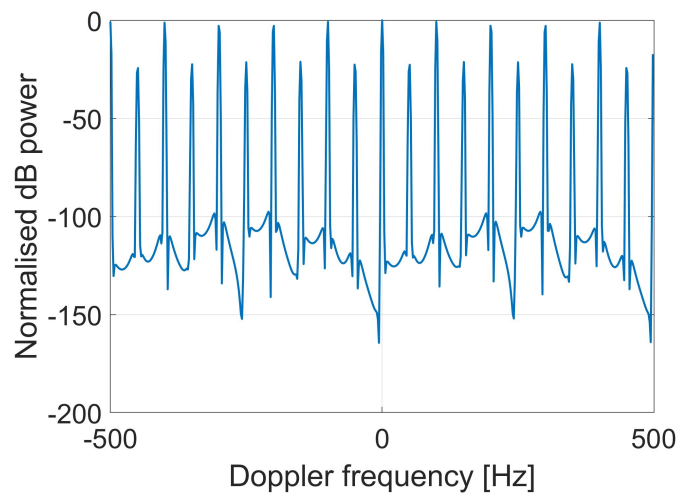
(c)

Figure 4.1: The micro-Doppler spectrum of a rotating thin wires as a function of the input variables of the Bessel functions. Parameters CPI = 0.512 s, PRF = 1 kHz, T_{rot} = 0.02 s: (a) f_c = 1.5 GHz, l_m = 1 m, (b) f_c = 1.5 GHz, l_m = 2 m, (c) f_c = 3 GHz, l_m = 2 m
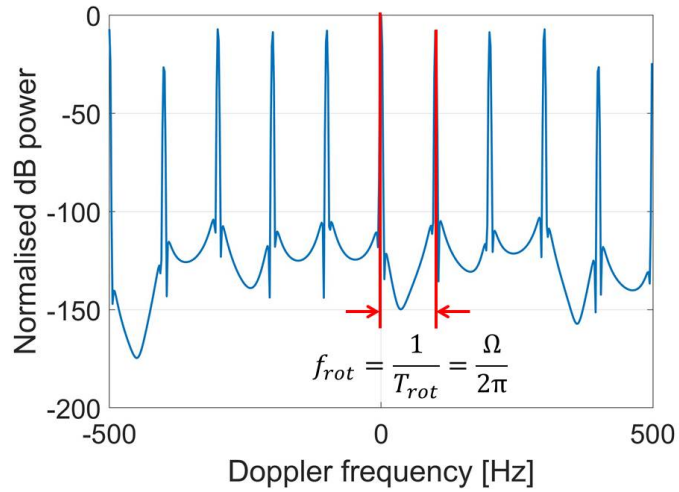
(a)
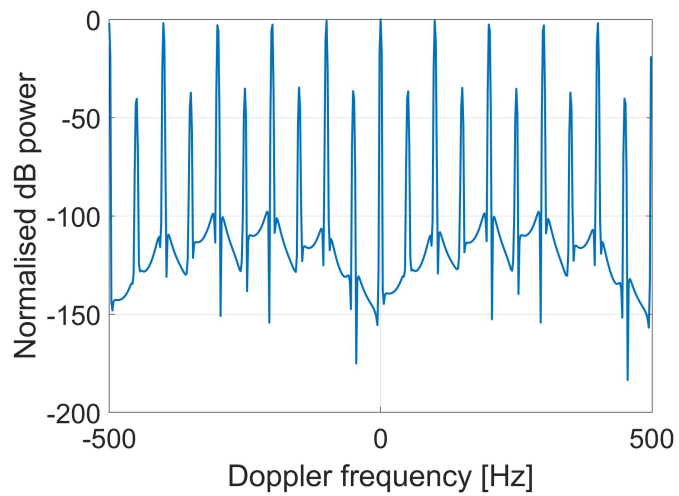
(b)

Figure 4.2: The micro-Doppler spectrum of a rotating thin wires as a function of the angular rotation velocity. Parameters CPI = 0.512 s, PRF = 1 kHz, f_c = 3 GHz, l_m = 1 m: (a) T_{rot} = 0.01 s, (b) T_{rot} = 0.02 s
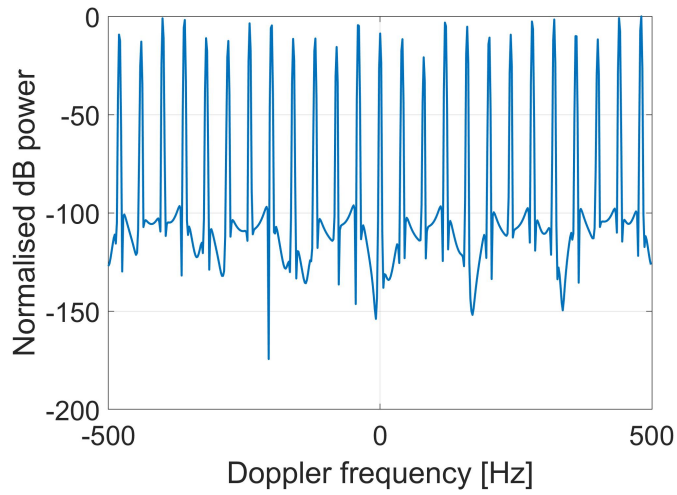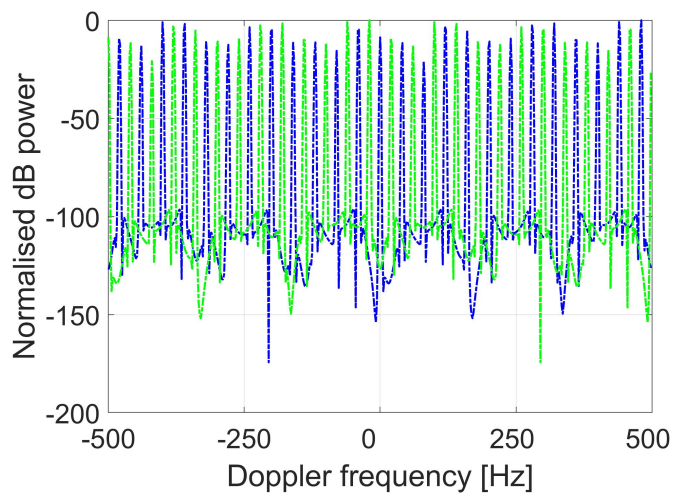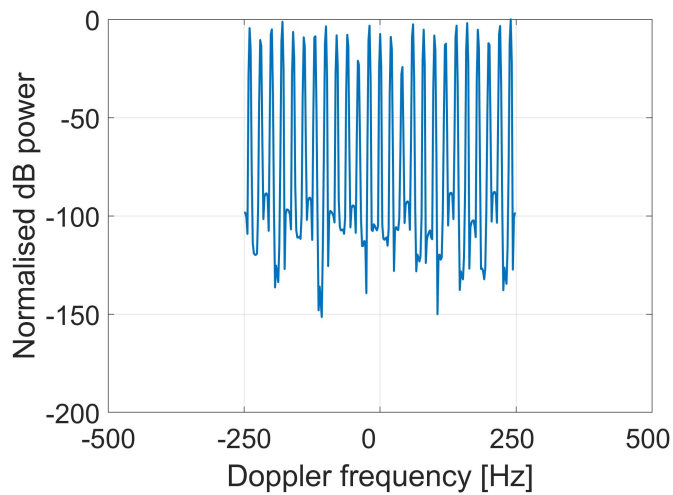
Figure 4.3: The micro-Doppler spectrum of a rotating thin wires observed at different radar PRF's. Parameters CPI = 0.512 s, T_{rot} = 0.0125 s, f_c = 3 GHz, l_m = 1 m: (a) PRF = 1 kHz, (b) PRF = 0.5 kHz, before aliasing/folding (Blue dashed line illustrates the spectrum without aliasing/folding within the Doppler frequency interval of [-250, 250] Hz, while green dashed lines illustrate the spectrum from other Doppler frequency intervals), (c) PRF = 0.5 kHz, with aliasing/folding

4.1.4. Asynchronous Rotation of Propellers

As discussed in precious chapters2, the micro-Doppler spectrum of a multi-propeller drone is similar to that of a single rotating thin wire, but of more complexity due to the drone geometry, blade length and propeller synchronisation. Figure 4.4 gives an example of the micro-Doppler patterns of two thin wires of the same length simultaneously rotating around the same centre point with different rotation periods.

The micro-Doppler spectrum of the two thin wires of the same length simultaneously rotating at different angular velocity is the synthesis of the micro-Doppler spectrum of the thin wires rotating at their own angular velocity individually. Specially, the amplitude and the frequency of the harmonic components in the synthetic micro-Doppler spectrum still follows the analysis for each of the single wire in terms of the amplitude modulation of Bessel functions and the frequency gap determined by the angular rotation velocity. This agrees well with the mathematical description of the drone's micro-Doppler pattern in previous chapters (see Equation 3.12). In the long CPI circumstances, the micro-Doppler pattern of a drone is linear where the synchronisation of propellers in angle and the geometry structure design of the drone are negligible. So the asynchronous angular rotation velocity of the propellers is the principal factor which introduces further complexity to the micro-Doppler spectrum in terms of harmonic components.

4.2. Feature Proposal

Based upon the analysis on the influence of the variables on the micro-Doppler spectrum, the linear micro-Doppler pattern of a multi-propeller drone in long CPI circumstances can be written – as a function of the geometry structure design and the flight attitude of the drone and the radar setups, or a function of the amplitude modulation and the frequency distribution – as follows

$$
\begin{aligned}
S^{drone}[m] &= f(m, N, P, B, W, \lambda, r_p, \theta_{p,b,w}, \Omega_p, PRF, l_{p,b,w}) \\
&= f_i(m, f_{drone}(r_p, \theta_{p,b,w}, P, B, W, l_{p,b,w}, \Omega_p), f_{radar}(N, \lambda, PRF)) \\
&= f_{ii}(m, f_{amplitude}(\theta_{p,b,w}, \lambda, l_{p,b,w}, \Omega_p), f_{frequency}(PRF, \Omega_p, N)) \\
m &= 0, 1, ..., N-1
\end{aligned}
\tag{4.2}
$$

Equation 4.2 indicates that characterising the micro-Doppler spectrum in terms of amplitude modulation and frequency distribution is equivalent to characterising the drone's geometry structure design, flight attitude and radar setups. So it is a natural choice to propose features characterising these two properties of the micro-Doppler spectrum – As long as these properties of the micro-Doppler spectrum is well characterised by the features under given radar setups, the drone's geometry structure design and flight attitude properties are characterised, which relates to the specific model type of the drone.

In theory, there are many possible combinations of features can be used for further drone classification, as long as the proposed features illustrate the micro-Doppler spectrum's property in terms of amplitude modulation and frequency distribution. In this section, two specific categories of features are proposed, frequency distribution features and statistic amplitude features. The first correspond to the frequency distribution or
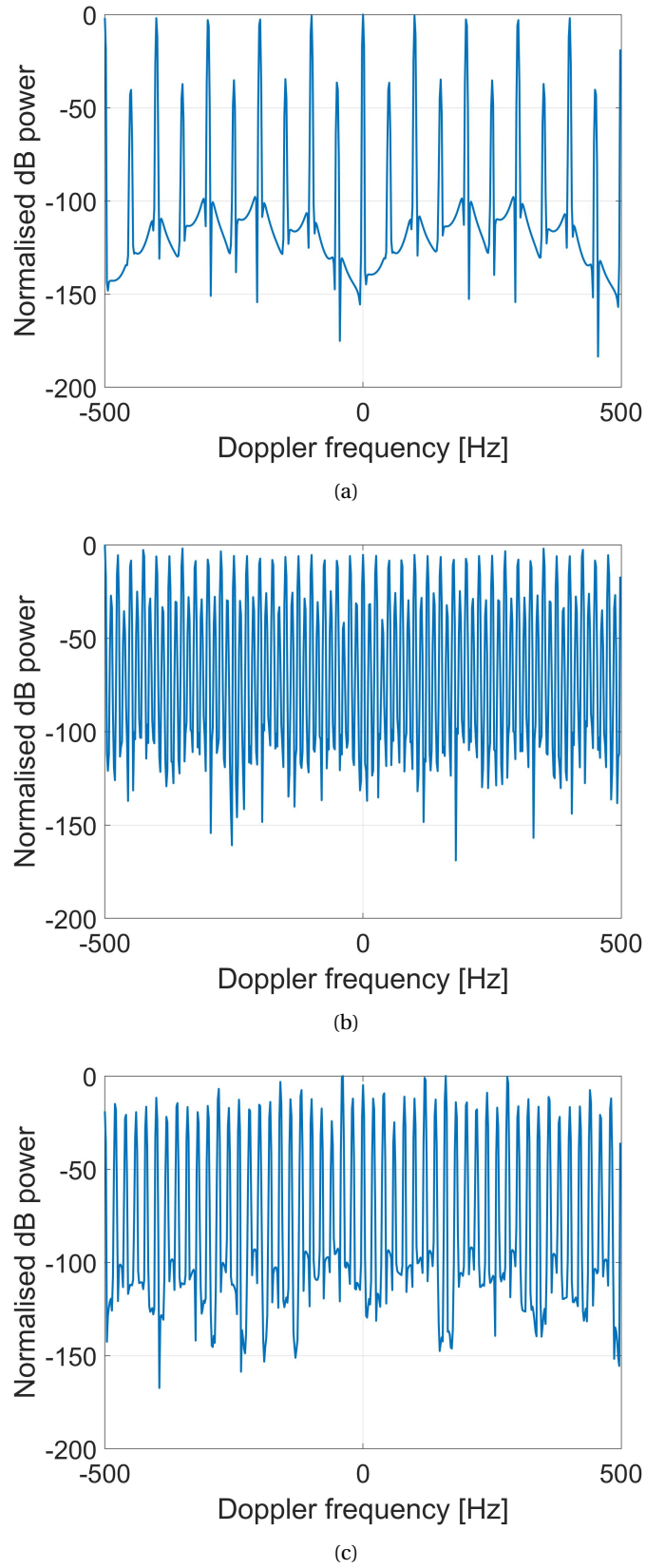
Figure 4.4: The micro-Doppler spectrum of two rotating thin wires with different rotation periods. Parameters CPI = 0.512 s, PRF = 1 kHz, f_c = 3 GHz, l_w = 1: (a) T_{rot} = 0.02 s, (b) T_{rot} = 0.0267s, (c) $T_{rot1,2}$ = 0.02 and 0.0267 s

frequency gap of the harmonic components over the Doppler frequency harmonic components in the statistic way.

4.2.1. Amplitude Features and Frequency Features

This section proposes features corresponding to the amplitude modulation and frequency distribution. The micro-Doppler spectrum is referred to a vector V_o as follows

$$V_o = [V_o^{(1)}, V_o^{(2)}, ..., V_o^{(N_f)}]^T \tag{4.3}$$

where symbol T indicates transpose operator. The spectrum vector V_o is of N_f dimensions, i.e. containing N_f entries. Parameter N_f is the number of frequency sampling points, determined by the length of STFT window in the Doppler processing. The subscript o indicates the vector V_o together with its entry $V_o^{(i)}$ is the original spectrum directly achieved by averaging the micro-Doppler over time. Intuitively, the spectrum vector V_o illustrate the value of the normalised dB power at each frequency point in the micro-Doppler spectrum.

The spectrum vector V_o contains both the micro-Doppler spectrum corresponding to the drone and the background noise. In order to filter out the background noise, a threshold is selected, below which the spectrum value is regarded as the background noise and set zero, above which the spectrum value is kept as micro-Doppler information. A hard threshold may not be the best choice in any circumstance, but works well in the simulations as in previous sections, since the noise floor is set by ourselves 0.4 lower than the micro-Doppler spectrum in the normalised dB spectrum figure. The noise threshold is set as follows

$$\bar{V}_o = \frac{1}{N_f} \sum_{i=1}^{N_f} V_o^{(i)} \tag{4.4}$$

where symbol ⁻ indicates arithmetic mean. The noise threshold can be rewritten in vector fashion as follow

$$T_{BG} = [0, ..., 1, 0, ..., 1, ..., 0]^T \tag{4.5}$$

where the threshold vector T_{BG} is a N_f-dimension vector with only one and zero entries. Each one entry indicates the value of the original micro-Doppler spectrum $V_o^{(i)}$ at the ith frequency point is larger than the threshold, while zero entry smaller.

The background noise is filtered out by the comparison of the original spectrum vector V_o and the noise threshold $\bar{V}_o$. Each entry $V_{o(i)}$ of the spectrum vector V_o larger than the noise threshold $\bar{V}_o$ remains, while each smaller is replaced by zero entry. The background-filtered spectrum vector is given as follow

$$\begin{aligned} V_{NBG} &= D_{BG} \cdot V_o \\ &= [0, ..., V_o^{(i_1)}, 0, ..., V_o^{(i_2)}, ..., 0]^T \end{aligned} \tag{4.6}$$

where D_{BG} is a diagonal matrix with $diag(D) = T_{BG}$. The non-zero entries $V_o^{(i_1)}$, $V_o^{(i_2)}$, etc., in the background-filtered spectrum vector V_{NBG} are of the same index as the one entries in the threshold vector T_{BG}. The

intuitive interpretation of this background filtering operation is taking the value of the normalised dB power above the threshold level at each frequency point the same in the micro-Doppler spectrum, while suppressing the rest spectrum to zero power.

Further, the amplitude and frequency values corresponding to the harmonic components in the micro-Doppler spectrum is found. The amplitude V_p of the harmonic components and the frequency difference between neighbouring harmonic frequency components F_{diff} are give as

$$V_p = [V_p^{(1)}, V_p^{(2)}, V_p^{(N_p)}]^T \tag{4.7}$$

$$F_{diff} = [f_{diff_1}, f_{diff_2}, ..., f_{diff(N_p-1)}]^T \tag{4.8}$$

where the superscript (1), (2), etc. indicates the 1st, 2nd, etc. local maximum, each corresponding to a harmonic component in the micro-Doppler spectrum, and the total number of local maxima is N_p. The vector F_{diff} can be also interpreted as the frequency difference of the spectruml peaks corresponding to the harmonic components in Equation 4.1, containing the information of the frequency distribution of the micro-Doppler modulated by the propeller's angular rotation velocity.

The overall feature vector proposed for the normalised dB power micro-Doppler spectrum is formed as follows

$$f_e = [V_p^T, F_{diff}^T]^T \tag{4.9}$$

where the first feature V_p^T is the amplitude feature defined as in Equation 4.7, and the latter featureis the frequency feature defined as in Equation 4.8.

4.2.2. Feature Matrix

The proposal and extraction of features introduced above is for a single observation, i.e., the micro-Doppler spectrum at one time point. This single observation is achieved by averaging the linear micro-Doppler patterns over time in previous sections, but can also be achieved by cutting the linear micro-Doppler patterns into slices at each time point. For a number of observations, the proposed feature list can be extracted for each one observation, and by forming the extracted feature lists of all observations in to a matrix, the feature matrix F_e for the whole observation data set is achieved as follows

$$F_e = [f_e^{(1)}, f_e^{(2)}, ..., f_e^{(N_o)}] \tag{4.10}$$

where feature list vector $f_e^{(i)}$ indicates the feature list extracted from the ith observation, and the variable N_o is the number of all observations in the data set. Each column in the feature matrix F_e corresponds to an observation, and each row corresponds to a feature variable defined in previous sections, thus the larger the data set of observations is, the more columns the feature matrix contains, and the more number of frequency points achieved from the Doppler processing, the more rows the feature matrix contains.

In following sections and chapters, such feature matrix is formed for each data set of several observations

of the micro-Doppler spectrum of multi-propeller drones, and then the feature matrix is used in the following classification algorithms.

4.2.3. Feature Standardisation

The mathematical operation of feature standardisation is to eliminate the effect of the different absolute values of different feature entries. The feature matrix F_e defined in Equation 4.10 is rewritten given as expansion as follows

$$F_e = [f_e^{(1)}, f_e^{(2)}, ..., f_e^{(N_o)}]$$

$$= \begin{bmatrix} V_p^{(1)} & V_p^{(2)} & ... & V_p^{(N_o)} \\ \mu^{(1)} & \mu^{(2)} & ... & \mu^{(N_o)} \\ \sigma^{(1)} & \sigma^{(2)} & ... & \sigma^{(N_o)} \\ s^{(1)} & s^{(2)} & ... & s^{(N_o)} \\ k^{(1)} & k^{(2)} & ... & k^{(N_o)} \\ e_n^{(1)} & e_n^{(2)} & ... & e_n^{(N_o)} \end{bmatrix}$$

$$= \begin{bmatrix} f_e^{(1,1)} & f_e^{(1,2)} & ... & f_e^{(1,n)} \\ f_e^{(2,1)} & f_e^{(2,2)} & ... & f_e^{(2,n)} \\ ... & ... & ... & ... \\ f_e^{(m,1)} & f_e^{(m,2)} & ... & f_e^{(m,n)} \end{bmatrix} \tag{4.11}$$

where parameter m and n indicate the number of rows and columns in the feature matrix. All the other parameters are defined as in Equation 4.10 and Equation 4.9. In the feature matrix F_e, every column corresponds to all the features extracted from an observation, and every row corresponds to a feature extracted from all the observations. In the same observation column, the absolute values of the features may vary much – in some circumstances are even of different orders of magnitude, since these features are of different mathematical and physical meanings. It is the relative values of the feature entries of different observations in the same feature row illustrate the properties of the observations in this feature dimension. So if several feature entries in the same row resemble to each others, the observations contain similar information and property in terms of this feature. The n by m standardised feature matrix F_{stan}, maintaining the similarity and difference in each row and stretching the entry values into the same scale in each column, is developed from Equation 4.11 as follows

$$F_{stan} = \begin{bmatrix} f_{stan}^{(1,1)} & f_{stan}^{(1,2)} & ... & f_{stan}^{(1,n)} \\ f_{stan}^{(2,1)} & f_{stan}^{(2,2)} & ... & f_{stan}^{(2,n)} \\ ... & ... & ... & ... \\ f_{stan}^{(m,1)} & f_{stan}^{(m,2)} & ... & f_{stan}^{(m,n)} \end{bmatrix} \tag{4.12}$$

where each entry of $f_{stan}^{(i,j)}$ is defined as follows

$$
\begin{aligned}
f_{stan}^{(i,j)} &= \frac{f_e^{(i,j)} - \mu_{f_e^{(i)}}}{\sigma_{f_e^{(i)}}} \\
&= \frac{f_e^{(i,j)} - \frac{1}{n}\sum_{j=1}^{n} f_e^{(i,j)}}{\sqrt{\frac{1}{n-1}\sum_{j=1}^{n}\left| f_e^{(i,j)} - \frac{1}{n}\sum_{j=1}^{n} f_e^{(i,j)} \right|^2}}
\end{aligned}
\tag{4.13}
$$

where parameter $\mu_{f_e^{(i)}}$ and $\sigma_{f_e^{(i)}}$ indicate the arithmetic mean and standard deviation of the entry values in the ith row in the feature matrix F_e, corresponding to the ith feature dimension. By performing standardisation, the arithmetic mean $\mu_{f_{stan}^{(i)}}$ and standard deviation $\sigma_{f_{stan}^{(i)}}$ of the entry values in the ith row in the standardised feature matrix F_{stan} is 0 and 1, respectively.

This property of the standardised feature matrix F_{stan} can be interpreted as follows. In the ith feature dimension, corresponding to the ith row in the standardised feature matrix $f_{stan}^{(i,j)}$, the feature values of all the observations $[f_{stan}^{(i,1)}, f_{stan}^{(i,2)}, ..., f_{stan}^{(i,n)}]$ are spread around the coordinate origin along this dimension (arithmetic mean $\mu_{f_{stan}^{(i)}} = 0$), and for any feature dimension $i^{th} = 1, 2, ..., m$, the feature values are spread in neighbouring intervals of almost the same distance from the coordinate origin (standard deviation $\sigma_{f_{stan}^{(i)}} = 1$). In this way, the absolute values of different features extracted from a single observation, varying a lot due to the physical meanings, are unweighted and thus the physically small values are not submerged by the physically overwhelmingly large values, and different features from the single observation equally characterise the observation's property.

4.3. Feature-Based Drone Classification on Simulated Data

In this section, simulation observation data is acquired using the thin-wire model. A few observation data is randomly selected as the training data set, while the rest most as the test data set. Feature extraction and standardisation are performed on the training data set, and drone classification is performed on the test data set.

4.3.1. Simulated Data Acquisition

In order to generate data sets of micro-Doppler patterns of multi-propeller drones, the thin-wire model is used, considering different drone model types and different drone flight attitudes. Table 4.1 gives different combinations of input variables to simulate the micro-Doppler patterns of the quadcopter, hexacopter and octocopter. For each drone model type, two flight attitudes are simulated, the hovering scenario and the cross range maneuvering scenario. In both these flight attitudes, the drones are of no radial velocity along LOS towards or away from the observation point. In the hovering scenario, all the drone propellers are of the same angular rotation velocity, while in the maneuvering scenario, half of the propellers rotate faster or slower than the the standard angular rotation velocity.

Using each combination of input variables shown in Table 4.1, several observations are simulated using

Table 4.1: Variables in Thin-Wire Model of Drones in Flight Attitudes

Combination of Input Variables	Drones & Flight Attitudes	Blade Length l [m]	Arm Length d_p [m]	Propeller Angular Velocity Ω [rpm]
(a)	quadcopter hover	0.114	0.175	$2200 * [1, -1, 1, -1]$
(b)	quadcopter cross range			$2200 * [1, -v_{asyn}, v_{asyn}, -1]$ $v_{asyn} = 1.5$
(c)	hexacopter hover	0.267	0.567	$1800 * [1, -1, 1, -1]$
(d)	hexacopter cross range			$1800 * [1, -v_{asyn}, v_{asyn}, -1]$ $v_{asyn} = 1.5$
(e)	octocopter hover	0.267	0.567	$1500 * [1, -1, 1, -1]$
(f)	octocopter cross range			$1500 * [1, -v_{asyn}, v_{asyn}, -1]$ $v_{asyn} = 1.5$

the thin-wire model. The number of simulated observations corresponding to each input variable combination is given as follows

- Combination (a) quadcopter hovering – 665 observations,

- Combination (b) quadcopter cross range maneuvering – 683 observations,

- Combination (c) hexacopter hovering – 661 observations,

- Combination (d) hexacopter cross range maneuvering – 672 observations.

- Combination (c) octocopter hovering – 674 observations,

- Combination (f) octocopter cross range maneuvering – 645 observations.

which a feature list can be extracted from by the means given in Equation 4.9 for each observation, and a feature matrix can be formed up combining several feature lists. The extracted feature matrix is further used as data sets of different drones in different flight attitudes in following drone classifications.

4.3.2. Feature Extraction on Simulated Data

An example of micro-Doppler spectrum consisting of the harmonic components with amplitude modulation is shown here, in order to illustrate the specific operations of feature proposal and extraction. Figure 4.5 shows the original micro-Doppler spectrum, the first 4 harmonic components and the amplitude and frequency features extracted from each harmonic component. The amplitude of each harmonic component is written as $A_{q(+/-)}$ where parameter q indicates the qth harmonic component from 0 order harmonic component at 0 Hz and symbol $+/-$ indicates the harmonic component in the positive or negative frequency interval. The frequency difference between the qth harmonic component and the $(q-1)^{th}$ harmonic component is written as $\Delta f_{n(+/-)}$.

Different from the feature proposal scheme introduced in previous sections, the amplitude and frequency features are only extracted from the first 4 harmonic components here. The selection of the first 4 harmonic around 0 Hz does not harm the generality for following reasons. According to the Bessel expansion of the
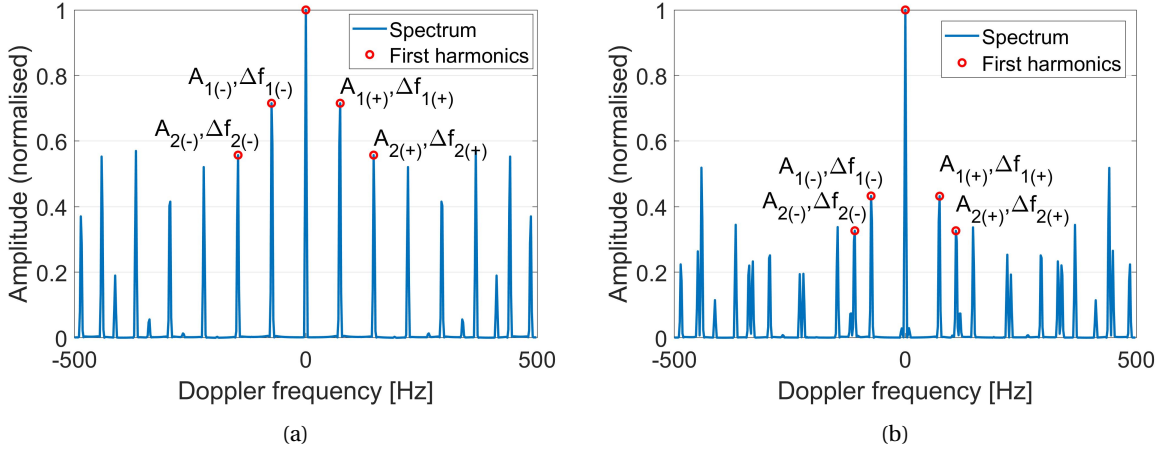
Figure 4.5: Examples of simulated micro-Doppler spectra with red circles indicate the first harmonic components around 0 Hz: (a) hovering quadcopter, (b) cross range maneuvering quadcopter

radar signal model, given the values of the first two Bessel functions, the whole series of the Bessel values are determined, which influence the amplitude of the harmonic components. Besides, in the hovering scenario, the frequency difference between high-order harmonic components is equal to that between the first 2 harmonic components, thus do not introduce extra information. In the maneuvering scenario, the frequency difference between high-order harmonic components differs from that between the first 2 harmonic components, as a result of the staggering angular rotation velocity of the propellers, but still do not introduce extra information. Moreover, the high-order harmonics usually suffer from the folding due to the PRF limit (1 kHz/2 in this case) and contaminate each other. The folding happens in the real measurements, too. Apart from the folding, the amplitude of the high-order harmonic components are smaller than the low-order ones, in the real measurements, the high-order harmonic components usually submerge in the background.

4.3.3. Principal Component Analysis and Feature Space

Feature matrices are formed up, in the hovering scenario and maneuvering scenario, from the simulated observation of micro-Doppler spectra achieved as in Table 4.1, by extracting the amplitude and frequency feature pairs for the first 4 harmonic components. The feature matrices are taken as examples to implement the feature standardisation and PCA. The observation data is divided into two scenario groups, the hovering scenario of Combination (a), (c) and (e), and the cross range maneuvering scenario of Combination (b), (d) and (f). In each scenario group, a feature matrix is extracted from all the data observation, standardised and performed SVD. The final feature matrix for each scenario group F_h, F_c is shown as follows

$$F_h = U_h \Sigma_h V_h^T \tag{4.14}$$

$$F_c == U_c \Sigma_c V_c^t \tag{4.15}$$

where the subscript h and c indicate hovering scenario and cross range maneuvering scenario. Then SVD is performed to these two feature matrices.

Figure 4.6 gives the singular values normalised to the maximum singular value for both feature matrices. In the hovering scenario, the first three singular values are relatively large compared with the rest, meaning in the corresponding vector space much information about the dispersion of the observation data is illustrated (see Figure 4.6a). It is possible to map the original amplitude and frequency feature vectors for all observations into a 3 dimensional vector space corresponding to the first 3 singular values, and these 3 new features deliver most information contained in the original features. In the maneuvering scenario, the first 3 singular values are not dominantly greater than the rest, meaning if mapping the original feature vectors of the first harmonic components' amplitude and frequency into the 3D space, more information contained in the original features is lost than in the hovering scenario (see Figure 4.6b). In theory, in order to characterise the data in the maneuvering scenario on the same accuracy level as in the hovering scenario, more singular components, i.e., higher space dimensions, are required.

(a)   (b)
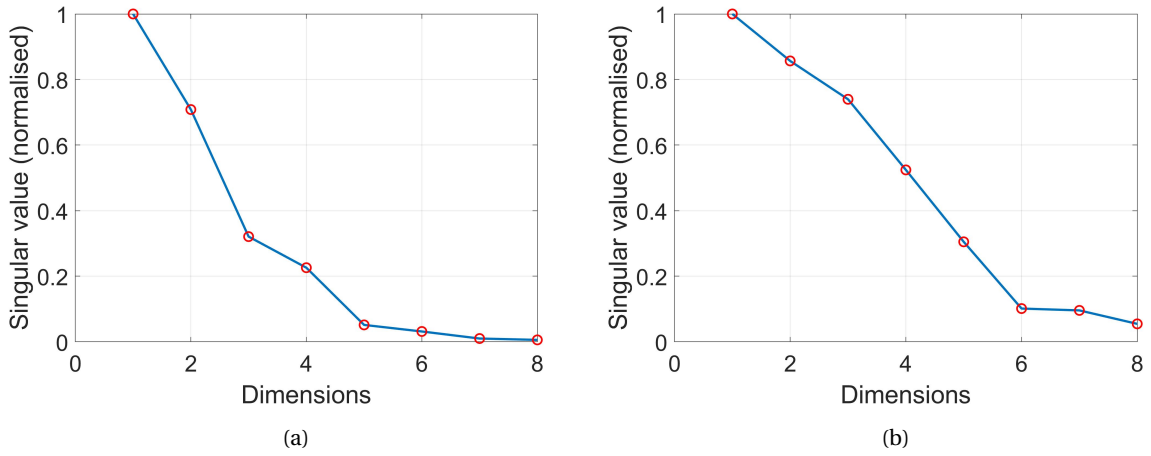
Figure 4.6: Examples of the feature matrix's singular values as a function of feature space dimensions for the simulated observation data. Simulated scenarios: (a) Hovering scenario, (b) Maneuvering scenario

The PCA is performed to the feature matrices $F_h^{(3d)}$ and $F_c^{(3d)}$ using the first three feature vectors as follows

$$F_h^{(3d)} = \begin{bmatrix} u_h^{(1)} & u_h^{(2)} & u_h^{(3)} \end{bmatrix}^T F_h \tag{4.16}$$

$$F_c^{(3d)} = \begin{bmatrix} u_c^{(1)} & u_c^{(2)} & u_c^{(3)} \end{bmatrix}^T F_c \tag{4.17}$$

where the superscript $(3d)$ indicate the 3-dimension (3D) vector space after PCA corresponding to the 3 greatest singular values. Figure 4.7 illustrates the simulated observation data of the three drones in the post-PCA vector space.

For the specific simulated data in these examples, the relation between the 3 new features and the original 8 features (4 amplitude features and 4 frequency features) are given as follows

$$F_{h,1}^{(3d)} = -0.24 A_{2(-)} - 0.38 A_{1(-)} - 0.38 A_{1(+)} - 0.24 A_{2(+)} - 0.38 f_{2(-)} - 0.39 f_{1(-)} - 0.38 f_{1(+)} - 0.39 f_{2(+)} \tag{4.18}$$

$$F_{h,2}^{(3d)} = +0.51 A_{2(-)} + 0.26 A_{1(-)} + 0.26 A_{1(+)} + 0.51 A_{2(+)} - 0.31 f_{2(-)} - 0.27 f_{1(-)} - 0.27 f_{1(+)} - 0.31 f_{2(+)} \tag{4.19}$$
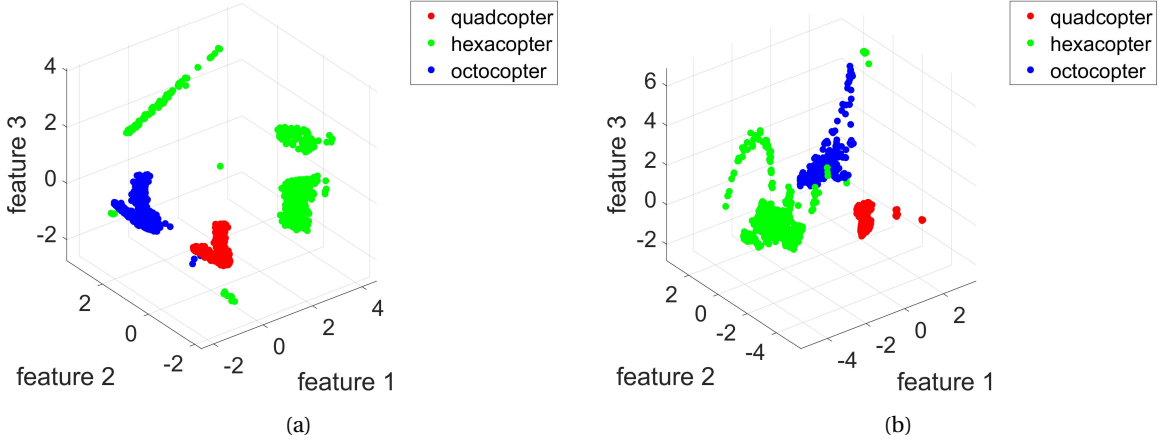
Figure 4.7: Post-PCA feature space for the simulated observation data. Simulated scenarios: (a) Hovering scenario with all observations, (b) Maneuvering scenario with all observations

$$F_{h,3}^{(3d)} = +0.4A_{2(-)} - 0.52A_{1(-)} - 0.52A_{1(+)} + 0.4A_{2(+)} + 0f_{2(-)} + 0.24f_{1(-)} + 0.24f_{1(+)} + 0f_{2(+)} \qquad (4.20)$$

$$F_{c,1}^{(3d)} = -0.42A_{2(-)} + 0.34A_{1(-)} + 0.34A_{1(+)} - 0.42A_{2(+)} - 0.06f_{2(-)} + 0.45f_{1(-)} + 0.45f_{1(+)} - 0.06f_{2(+)} \qquad (4.21)$$

$$F_{c,2}^{(3d)} = +0.08A_{2(-)} + 0.22A_{1(-)} + 0.22A_{1(+)} + 0.07A_{2(+)} - 0.59f_{2(-)} - 0.31f_{1(-)} - 0.31f_{1(+)} - 0.59f_{2(+)} \qquad (4.22)$$

$$F_{c,3}^{(3d)} = +0.39A_{2(-)} + 0.57A_{1(-)} + 0.57A_{1(+)} + 0.35A_{2(+)} + 0.21f_{2(-)} - 0.05f_{1(-)} - 0.06f_{1(+)} + 0.17f_{2(+)} \qquad (4.23)$$

where the subscript i indicates the ith new feature vector in the 3D vector space. The coefficients multiplied by the 8 original features giving the ith new feature vector are the entries of the ith greatest singular vector, and they can be interpreted as the weights of the original features in the ith dimension in the post-PCA feature space. In Equation 4.18, none of the 8 weights are negligible, thus all 8 original features contribute in this dimension. The weights of the 4 frequency features are almost the same, agreeing with the fact that in the hovering scenario, the frequency difference between neighbouring harmonic components is the same, determined by the propeller rotation speed. In Equation 4.19, the weights of the 2nd positive and negative harmonic components' amplitudes dominate, meaning that in this dimension, the separation of different drones is most made by the amplitude of the 2nd positive and negative harmonic components. In Equation 4.20, all the amplitude features contribute a lot to separate the drones. The small weights of the frequency features indicate that in this dimension, the frequency features do not contribute much. In Equation 4.21, most of the 8 original features are of the same weights, meaning they are not negligible. In Equation 4.22, the frequency differences of the 2nd positive and negative harmonic components are dominantly great, meaning in this dimension these frequency features are very important to separate the drones. This agrees with the analysis based on the mathematical radar signal model – In the maneuvering scenario, different propellers are of different rotation speed, thus the asynchronisation of these propellers is an important feature characterising the drone. In Equation 4.23, all the amplitude features contribute a lot to separate the drones, just as in the hovering scenario.

More simulations are performed with different setup variables, the weights of each feature may vary for

different simulations, but there are some general rules. In the hovering scenarios, all the amplitude and frequency features contribute to the separation (They are all not negligible in the 1st dimension), but introducing more frequency features do not help much in classification accuracy (In some dimensions, they become small to 0, when the amplitudes still play an important role). In the manoeuvring scenarios, the frequency features illustrating the asynchronisation of multiple propellers make an extra contribution (They dominate the separation of the drones in their own dimensions). In the simulation examples, only 8 features are extracted from the 4 harmonic components around 0 frequency, resulting in good classification accuracy. In real measurements, due to the background noise and the wind turbulence, both the amplitude and the frequency of each harmonic component are not so reliable. Then it is worthy to extract the amplitude and frequency features from more harmonic components. For the same reason, averaging the m-D spectrum over several seconds may be needed.

Over all, the PCA applied on the original amplitude and frequency features and the post-PCA 3D feature space intuitively illustrates the feasibility to classify different drones using the original proposed features or even new features further extracted from these original features.

4.3.4. Support Vector Machine Classification

Support Vector Machine (SVM) is a common tool in binary classification problem. SVM gives a hyperplane to separate the clusters of data points of different classes with the maximum margin between them. The idea of SVM can be written as follows

$$
\begin{aligned}
&min_{\boldsymbol{\omega},\gamma} \quad \frac{1}{2}||\boldsymbol{\omega}||^2 \\
&s.t. \quad y_i(\boldsymbol{\omega}^T\boldsymbol{x_i}+\gamma) \geq 1, \quad i=1,2,...,m
\end{aligned}
\tag{4.24}
$$

where symbol $s.t.$ is the abbreviation of subject to, parameter m indicates the number of data points, parameter $\boldsymbol{\omega}$ and γ determine the separating hyperplane, parameter $\boldsymbol{x_i}$ is the proposed feature vector for the ith data point, parameter y_i is the classification label of the ith data point, and symbol min indicates this is an optimisation problem for a quadratic form function under the inequality constraint.

To solve such an SVM problem, several algorithms have been developed. In following sections, an off-the-shell model of SVM is occupied to perform the classification on the simulated micro-Doppler spectra of the quadcopter and hexacopter. In this case, the label of the data points y_i is 1 or -1 corresponding to the quadcopter or hexacopter, the input data points $\boldsymbol{x_i}$ can be the 3 new features in the post-PCA vector space, or the original 8 features illustrating the harmonic component's amplitude and frequency or even the original micro-Doppler spectrum after 512-point FFT.

4.3.5. Classification Results on Simulated Data

This section performs SVM classification on the simulated data of the micro-Doppler spectra of the quadcopter and hexacopter. In each scenario, the 5-fold cross validation L1 SVM is occupied, with the linear kernel of kernel scale 1. Figure 4.8 gives the curves of the classification error probability in both drone flight atti-

tude scenarios. In each scenario, apart from the classification based on the proposed features, the simulated micro-Doppler spectra are also directly used in the SVM classification, as a reference of the best classification performance can be achieved on the simulated data.
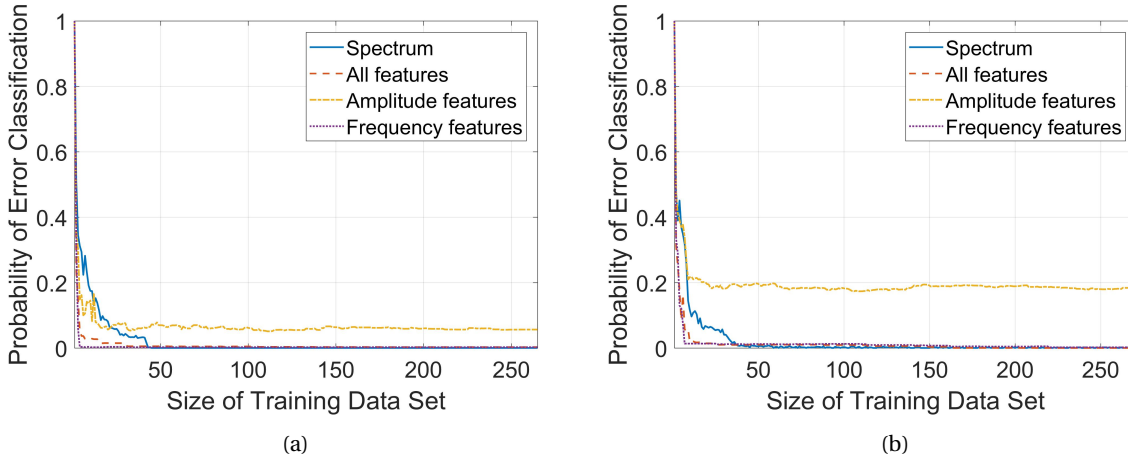
Figure 4.8: The classification error probability as function of training dataset size. Red lines correspond to the classification results based on the proposed features, while blue dashed lines correspond to the classification results based on the spectra. Simulated scenarios: (a) Hovering scenario with 1 to about 250 observations in the training dataset, (b) Maneuvering scenario with 1 to about 250 observations in the training dataset

The results in Figure 4.8 demonstrates the proposed features well characterise the original micro-Doppler spectrum in both scenarios. When the original micro-Doppler spectra containing all the information about the spectra is directly used in the SVM classification, and gives a correct classification. When only the features illustrating the amplitude modulation and frequency distribution of the harmonic components in the micro-Doppler spectra, the probability of error classification is very close to zero in both scenarios.

The convergent error probability in the hovering scenario is lower than its counterpart in the maneuvering scenario, meaning the specific features extracted in this section deliver more information about the original micro-Doppler spectrum in the hovering scenario. Since in the maneuvering scenario, the complexity of the harmonic components increases, thus the proposed features do not extract as much information contained in the original micro-Doppler spectra as in the hovering scenario.

In the hovering scenario, both the amplitude and frequency features contribute much to the classification accuracy, and the error probability is below 10% when only the amplitude or frequency features are used. In the maneuvering scenario, the amplitude features alone do not achieve a good classification accuracy, which reconfirms the analysis in precious section that in the maneuvering scenario, the frequency features play an important role in the classification.

4.4. Conclusions

This chapter makes an analysis on the drone micro-Doppler spectrum as a superimposition of harmonic frequency components in long CPI circumstances, and investigates the influence of factors, such as radar PRF, centre carrier frequency, drone propeller rotation period, length of propeller blade and the asynchronisation

of the propellers in angular velocity. These factors influence the micro-Doppler spectrum in terms of amplitude modulation and frequency distribution. The frequency distribution of the harmonic components in the micro-Doppler spectrum is influenced by the radar PRF, the angular rotation velocity of the propeller and the relation between CPI and propeller rotation period. The amplitude modulation is influenced by the centre carrier frequency of the radar, length of the propeller blade and propeller rotation period, through Bessel functions. It is demonstrated that, given the radar setups, characterising the micro-Doppler spectrum in terms of amplitude modulation and frequency distribution is equivalent to characterising the drone's geometry structure and flight attitudes. This gives an analytical description of the drone's micro-Doppler spectrum, and gives a guideline for feature selection from drone's micro-Doppler spectrum, generally applicable to various radar systems, in long CPI circumstances.

Specific features, namely, the first harmonic components' amplitude and the frequency difference between neighbouring harmonic components, are proposed as an example to characterise the drone micro-Doppler spectrum. SVM based on these features from the simulated micro-Doppler spectra gives good accuracy classifying different drones in various flight attitude scenarios. In both hovering and maneuvering scenarios, the probability of classification error converges to about 0, meaning the specific features used in this chapter most characterise the original micro-Doppler spectrum. PCA on the features shows that in both scenarios, the amplitude and frequency features contribute much to the correct classification. In the maneuvering scenario, the features illustrating the frequency difference between harmonic components make an dominantly contribution, which agrees with the fact that in the maneuvering scenario, the asynchronisation of the propellers in angular rotation velocity strongly characterises the drones.

It is noticed that, in the SVM classification, the training dataset should include enough number of micro-Doppler spectra from both the quadcopter and hexacopter. This is a property of SVM classifiers. Overall, the SVM reconfirms the proposed general feature selection scheme characterising the amplitude modulation and frequency distribution of the harmonic components, validates the specific extracted features of the first harmonic components' amplitude and frequency, reveals the contribution of different features in various scenarios, and successfully classify the quadcopter and hexacopter in hovering and maneuvring flight modes using the simulated micro-Doppler spectra.

In the next chapter, the feature selection scheme is applied to real drone's micro-Doppler patterns measured by PARSAX radar system.

Application to Real Data

5.1. PARSAX Measurements of Real Drone

The measurements of several multi-propeller drones in various flight attitudes are performed by PARSAX radar system. The experimental setups are introduced in detail in this section.

As illustrated in previous Chapter 3, the radar antennas are set pointing to the open air above the field where the drone flight experiments take place. The antennas elevate a bit to avoid ground clutter, but cover the altitude and area which the drones fly in. The radar system operates full-polarimetric measurements in FMCW mode at the centre frequency f_c = 3.315 GHz with a bandwidth BW = 50 MHz and PRF = 1 kHz. With these setup parameters, the range resolution of the radar is about 3 m, and observation is recorded in 4 horizontal-vertical channels for each experiment, while only the data in HH polarimetric channel is extracted and further analysed.

The multi-propeller drones of DJJ M200 [3] and DJI M600 [4] are occupied in the experiments. These drones are selected as representative of the quadcopters and hexacopters containing two-blade propellers common on market. These drones are of different geometry structure designs in terms of the whole drone and the propellers, different standard propeller angular rotation velocity under hovering flight attitude and different asynchronous propeller angular rotation velocity under maneuvering flight attitude. Table 5.1 gives the specifics of some of the differences of the drones in geometry structure design. According to the analysis of in previous Chapter 4, these variables have an influence on the drone micro-Doppler patterns, given all the other conditions the same.

For each drone model type, three flight attitudes are considered in the experiments, hovering, along range maneuvering and cross range maneuvering. The open air area in the experiments is in Poeldijk, the same as in previous Chapter 3. Figure 5.1 illustrates the motion paths of the drones in the experiments. In the measure-

Table 5.1: Specs of drones' geometry structure designs

Drone Model Type	Propeller Number	Arm Length / [m]	Blade Length / [m]
DJI M200	4	0.322	0.216
DJI M600	6	0.567	0.267

ment of hovering flight attitude, the drone is hovering stably at the spot of $Poeldijk\_p1$ for several minutes, indicated by the orange spot in the figure. In the measurements of along range and cross range maneuvering flight attitudes, the drone flies for the distance of 80 m along the red line $Poeldijk\_p1$ - $Poeldijk\_p2$ and yellow dashed line $Poeldijk\_p3$ - $Poeldijk\_p4$ radially and tangentially towards the antenna LOS, shown as the white line in the figure. In each of the maneuvering measurements, the drone repeatedly moves along the trajectory for 5 round-trips of several minutes in total.

Figure 5.1: Motion paths of the drones in the experiment field: (a) Orange spot – Hovering, (b) Red line – Along range maneuvering, (c) Yellow dashed line – Cross range maneuvering

In total, 6 experiments are performed for both 2 drones in all 3 flight attitudes

- Experiment (a) quadcopter M200 hovering,

- Experiment (b) quadcopter M200 along range maneuvering,

- Experiment (c) quadcopter M200 cross range maneuvering,

- Experiment (d) hexacopter M600 hovering,

- Experiment (e) hexacopter M600 along range maneuvering,

- Experiment (f) hexacopter M600 cross range maneuvering.

besides, an extra experiment is performed for the background of the empty sky in the same area as Experiment (g).

5.2. Signal Processing

This section gives the results of the open air experiments, introduces the Doppler processing and filtering together with the achieved data cube containing the micro-Doppler spectra, and extracts the final low-dimension feature matrix ready for the SVM classifier.

5.2.1. Range-Doppler Images and Data Cube

In the measurements, the output of the analogue-to-digital converter (ADC) is a series of complex values. Applying Fourier Transform to a single section of the complex value series over to the time interval of a PRI gives the range profile of the targets. By applying the second Fourier Transform in a single range cell across multiple PRIs gives the Doppler frequency information, and the total time interval occupied to achieve the Doppler information is a CPI. Figure 5.2 gives an example of the achieved data matrix after the second Fourier Transform in the range-Doppler coordinate in a single CPI for the quadcopter of DJI 200 at the distance of about 9 km observed by PARSAX radar system. Only tens of range cells around the range cells containing the target drone are shown in the figure, tough 5200 range cells in total are observed by PARSAX radar with a range resolution of 3 m. Besides, in the Doppler processing, 512-point Fourier Transform is performed, thus the Doppler frequency axis is devided into 512 points.
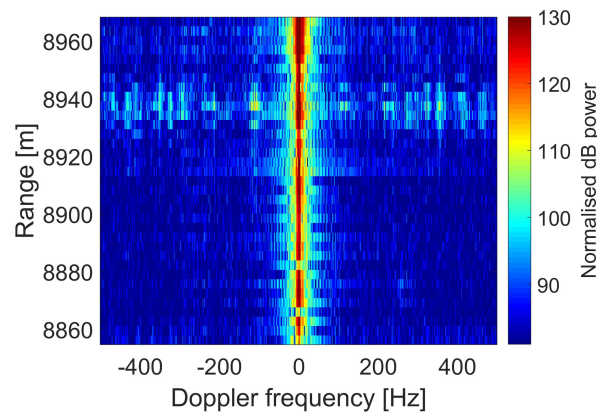
Figure 5.2: Example of range-Doppler image of drone measured by PARSAX radar system within a single CPI (only the neighbouring range cells around the target drone are shown)

Figure 5.2 shows the drone micro-Doppler patter in a single CPI. By stacking the micro-Doppler images across several CPIs one after another, the variation of the drone micro-Doppler over several CPIs is illustrated. If the drone is hovering in the same range cell over several CPIs, the micro-Doppler pattern stays in the same range cell of the same spectra shape from one CPI to another. If the drone maneuvers tangentially towards the LOS within the same range cell, the micro-Doppler pattern stays still in the same range cell of the same spectra, but the spectra varies from its counterpart in the hovering scenario. If the drone maneuvers radially towards the LOS across several range cells, the micro-Doppler pattern moves across various range cells from one CPI to another of the spectra shifting away from zero frequency. Figure 5.3 gives an example of the sequence of micro-Doppler images over several CPIs. In this figure, the drone is maneuvering along range, and

thus the micro-Doppler patterns are off zero Doppler frequency and in different range cells.
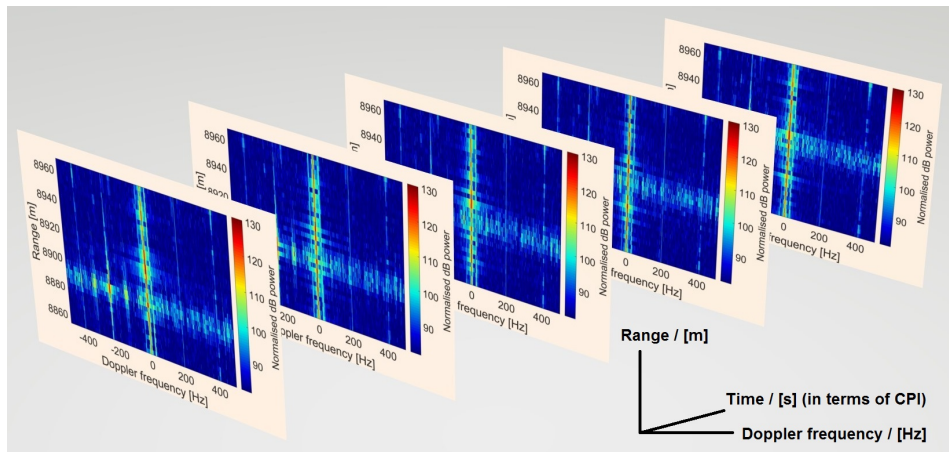
Figure 5.3: Example of range-Doppler images of drone measured by PARSAX radar system over several CPIs (only the neighbouring range cells around the target drone are shown)

In the same fashion as in Figure 5.3, a 3D data cube of complex values is formed up for a section of signal series over several CPIs (see Figure 5.4). The size of the data cube is determined by the range interval which the drone moves within, the Doppler bandwidth indicated by the PRI and the total observation time in terms of several CPIs. It should be noticed that, along the time axis, the time step is just one CPI. In this work, the range cells that drones move within are the range cells covering the distance of 80 m at about 9 km from the radar antennas.
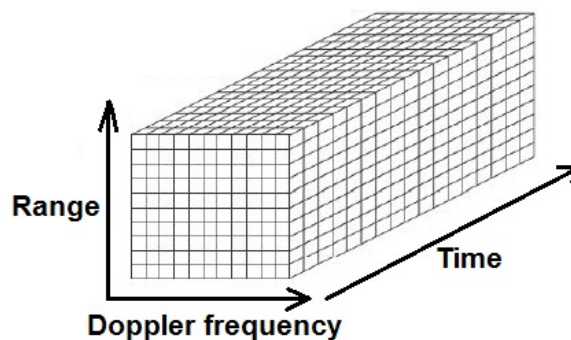
Figure 5.4: Data cube of drone micro-Doppler pattern over several CPIs, in the coordinate of range, Doppler frequency and time

Figure 5.5 illustrates the data cube of micro-Doppler patterns for either a drone staying within the same range cell or crossing several range cells. In the figure, the micro-Doppler patterns of a drone staying in the same range cell over time are shown in red dashed line, the micro-Doppler patterns of a drone crossing several range cells over time are shown in blue line, and the green lines indicate the motion along range axis of each drone.

So far, six data cubes are formed up corresponding to the six measurements introduced in previous sections. For the data of the quadcopter and hexacopter hovering in the sky, the micro-Doppler patterns appear only within a single range cell and of constant micro-Doppler spectra over time. For the data of the quadcopter and hexacopter maneuvering cross range, the micro-Doppler spectra shifts away from zero Doppler
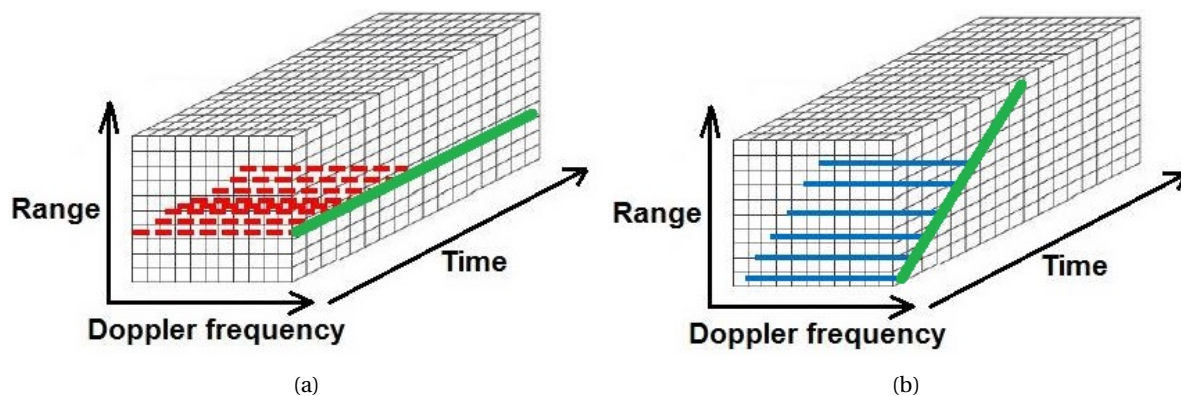
Figure 5.5: Data cube of drone micro-Doppler pattern over several CPIs, in the coordinate of range, Doppler frequency and time. Green line - Drone's motion along range over time: (a) Within a single range cell, (b) Across several range cells

frequency and may vary over time due to the asynchronous angular rotation velocity of propellers, but the patterns appear within or around the same range cell at different time points. For the data of the quadcopter and hexacopter maneuvering along range, the micro-Doppler patterns may move from range cell to range cell at different time points over CPIs.

In this work, the sizes of 6 data cubes corresponding to the 6 experiments are shown as follows

- Data cube for Experiment (a): 37 by 512 by 369,

- Data cube for Experiment (b): 37 by 512 by 350,

- Data cube for Experiment (c): 37 by 512 by 388,

- Data cube for Experiment (d): 37 by 512 by 337,

- Data cube for Experiment (e): 37 by 512 by 350,

- Data cube for Experiment (f): 37 by 512 by 390.

where the sizes of the three dimensions correspond to the number of range cells where the drones appear and move in, the number of Fourier points in the Doppler processing, and the total observation time in terms of several CPIs. Besides, an extra data cube for the background of the empty sky in the same area as in Experiment (g) is of the size of 37 by 512 by 100 – covering the 37 range cells where the drones move within from about 8979 m to 9098 m with each range cell of 3.3 m, achieved from 512-point Doppler processing, and observed over 100 CPIs of about 1 minute in time.

5.2.2. Drone Detection and Tracking

In the data cubes for either the hovering or maneuvering drones, most units in the data cubes do not contain micro-Doppler patterns, but only the background. In theory, at a specific time point corresponding to a single CPI, the drone micro-Doppler pattern appears only in a single range cell. In order to detect and track the drone in various range cells, the data cubes are processed as follow.

First, the normalised histogram of the data cube for the empty sky background is calculated and shown in Figure 5.6. In the calculation of the histogram, the data cube is treated as a whole in all range cells and time intervals, based on the assumption that the Doppler property of the empty sky background is homogeneous in range and consistent in time. It is shown that the histogram, as an alternative of the real probability density function (PDF), of the sky background data cube is approximately Gaussian distributed with the mean $\mu =$ 79.11 dB and standard deviation $\sigma = 7.08$.
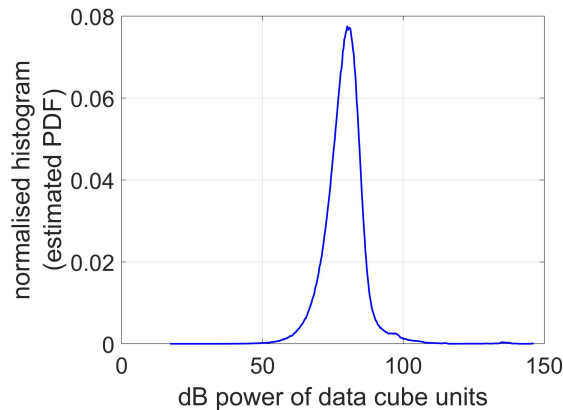
Figure 5.6: Normalised histogram of the dB power of the data cube of the sky background

For the data cubes corresponding to the hovering drones, since the drone stays in the same range cell, the micro-Doppler patterns always appear in the same range cell. A histogram is calculated for all the data cube units within each single range cell, and all the histograms corresponding to different range cells are compared with their counterpart for the empty sky background data cube. The range cell whose histogram varies most from the background histogram is selected as the one which the drone hovers in. The distance between histograms is measured by mean squared error (MSE) here. Figure 5.7 gives an example of the histograms for two range cells similar and different to the background histogram. In this figure, the histogram for the range cell corresponding to 8938 m shown as the blue curve varies from the background histogram most and thus selected as the one where the drone hovers.

For the data cubes corresponding to the cross range maneuvering drones, the same operation as for the data cubes corresponding to the hovering drones are performed to detect the data cube units containing the drone micro-Doppler patterns. This same detection method is valid, since for a drone moves tangentially to the LOS of radar antennas at the distance of about 9 km, the motion trajectory of 40 m away from the LOS is in the same range cell.

For the data cubes corresponding to the along range maneuvering drones, further operations are in need to detect and track the drones in various range cells. At each time point corresponding to the CPI time interval, the histogram achieved from the data cube units in each range cell is compared with the background histogram, and the most different one is selected as the one which the drone appears in at this moment.

The data cube units within the range cells selected as above are assumed to contain the micro-Doppler patterns of the drone, and the data cubes in the same range cell and time interval form up the micro-Doppler
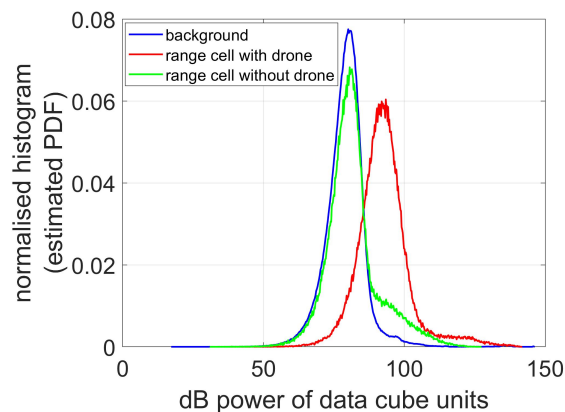
Figure 5.7: Example of normalised histograms of the dB power of the data cube for the quadcopter hovering in different range cells, similar and different from the background histogram. Curves: blue - background, green - range cell of 8869 m in the quadcopter hovering experiment, red - range cell of 8941 m in the quadcopter hovering experiment

spectra of the drone. These data units of micro-Doppler spectra are concatenated together as a matrix of observations. The size of the observation matrix is determined by the number of frequency points over the spectra bandwidth and the number of observations corresponding to the observation time in terms of the number of CPIs. Figure 5.8 illustrates the extracted observation matrix for the drones in various flight attitudes.

So far, the 6 observation matrices containing the drones' micro-Doppler patterns are extracted. The size of each observation matrix is given as follows

- Observation matrix (a): 512 by 369,

- Observation matrix (b): 512 by 350,

- Observation matrix (c): 512 by 388,

- Observation matrix (d): 512 by 337,

- Observation matrix (e): 512 by 350,

- Observation matrix (f): 512 by 390.

corresponding to the data cubes given in previous sections.

Several comments are made for the drone detection and tracking schemes introduced above. Since a number of Doppler observations in different range cells and time intervals are achieved, and the histogram of each measurement is calculated as an alternative of the real PDF, several more advanced detection and tracking techniques are available [15]. For simplicity, only the very preliminary hard threshold is set up here, but this simple and direct detection and tracking scheme gives good results.

5.3. Feature Extraction and Drone Classification

In this section, 4 scenarios are considered in total to perform the drone classification, hovering scenario, cross range maneuvering scenario, along range maneuvering scenario and mixed scenario which has no a priori
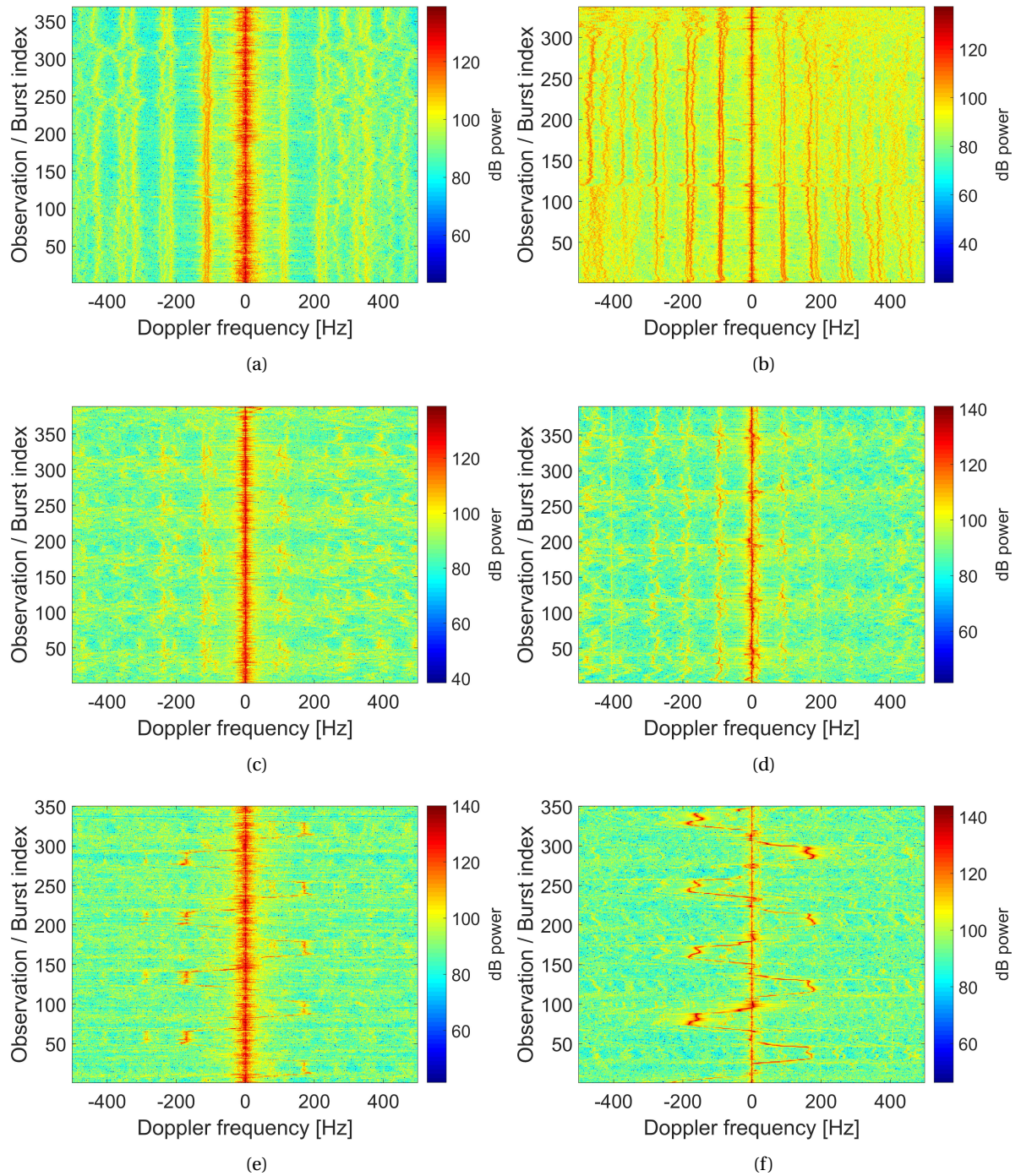
Figure 5.8: Observations of detected drone micro-Doppler patterns: (a) quadcopter, hovering, (b) hexacopter, hovering, (c) quadcopter, cross range maneuvering, (d) hexacopter, cross range maneuvering, (e) quadcopter, along range maneuvering, (f) hexacopter, along range maneuvering

knowledge about the drones' flight attitudes. In each scenario, the observations are selected from the corresponding observation matrices and shuffled, forming up the data sets. The aim of this section is to classify different model types of drones, i.e., quadcopter DJI M200 and hexacopter DJI M600 in various scenarios.

Feature extraction and feature standardisation are performed to the data sets, as introduced in previous chapters. The first 5 harmonic components around the main Doppler component are considered. In the hovering and cross-range maneuvering scenario, the main Doppler component is at 0 Hz, while in the along-range maneuvering scenario, the main Doppler component, together with the whole micro-Doppler pattern shifts away from 0 Hz due to the radial velocity. The frequency difference between the 1st order harmonic component and the main harmonic component, between the 2nd order harmonic component and the 1st order harmonic component, the amplitude of the 1st and 2nd order harmonic components normalised to the maximal main Doppler component are extracted as the feature vector for each observation of drone micro-Doppler pattern. In each scenario, the 5-fold cross validation L1 SVM is occupied, with the linear kernel of kernel scale 1.

Figure 5.9 gives the curves of the classification error probability in all 4 drone flight attitude scenarios, based on the proposed features and the original micro-Doppler spectra. The results based on the original micro-Doppler spectra indicates the best performance can be achieved on these measured data. Several comments are made from the comparison of the sub-figures. In all scenarios, the SVM classifier using the proposed amplitude and frequency features gives good classification results, indicating that these features characterise the original micro-Doppler spectra well. In the hovering scenario, both the original micro-Doppler spectra and the proposed features lead to lower than 3% classification error probability, meaning in this scenario, the quadcopter and hexacopter can be well classified, and the proposed features characterise almost all the information contained in the original micro-Doppler spectra. In the along range maneuvering scenario, the original micro-Doppler spectra give the classification error probability of 10%, meaning in this scenario, the complexity of the micro-Doppler spectra increases a lot than in the hovering scenario. By analysing the incorrectly classified observations, the error most appears when the drone has radial acceleration. The radial acceleration introduces further complexity to the micro-Doppler spectra. However, the acceleration motion usually only happens in a short time interval during the flight of the drone. In the along range maneuvering scenario, the proposed features give the classification error probability 10% higher than the original micro-Doppler spectra, meaning the extracted features do not characterise the original micro-Doppler spectra so well as in the hovering scenario. In the cross range maneuvering scenario, the classification error probability achieved from the original spectra is about 2%, meaning in this scenario, the two drones can be successfully classified. However, the proposed features result in the classification error probability of 20%, meaning these features do not work well characterising the micro-Doppler spectra in this scenario. Because in this scenario, the cross range motion introduces subtle flutter into the micro-Doppler spectra along the frequency axis, and it is difficult to separate the main Doppler component from the 0 Hz component, thus the frequency difference between harmonic components is smeared and incorrectly estimated. Besides, in the cross range maneuvering scenario, the micro-Doppler pattern appears like cloud, instead of linear patterns, thus the features proposed for the linear patterns do not work well anymore.
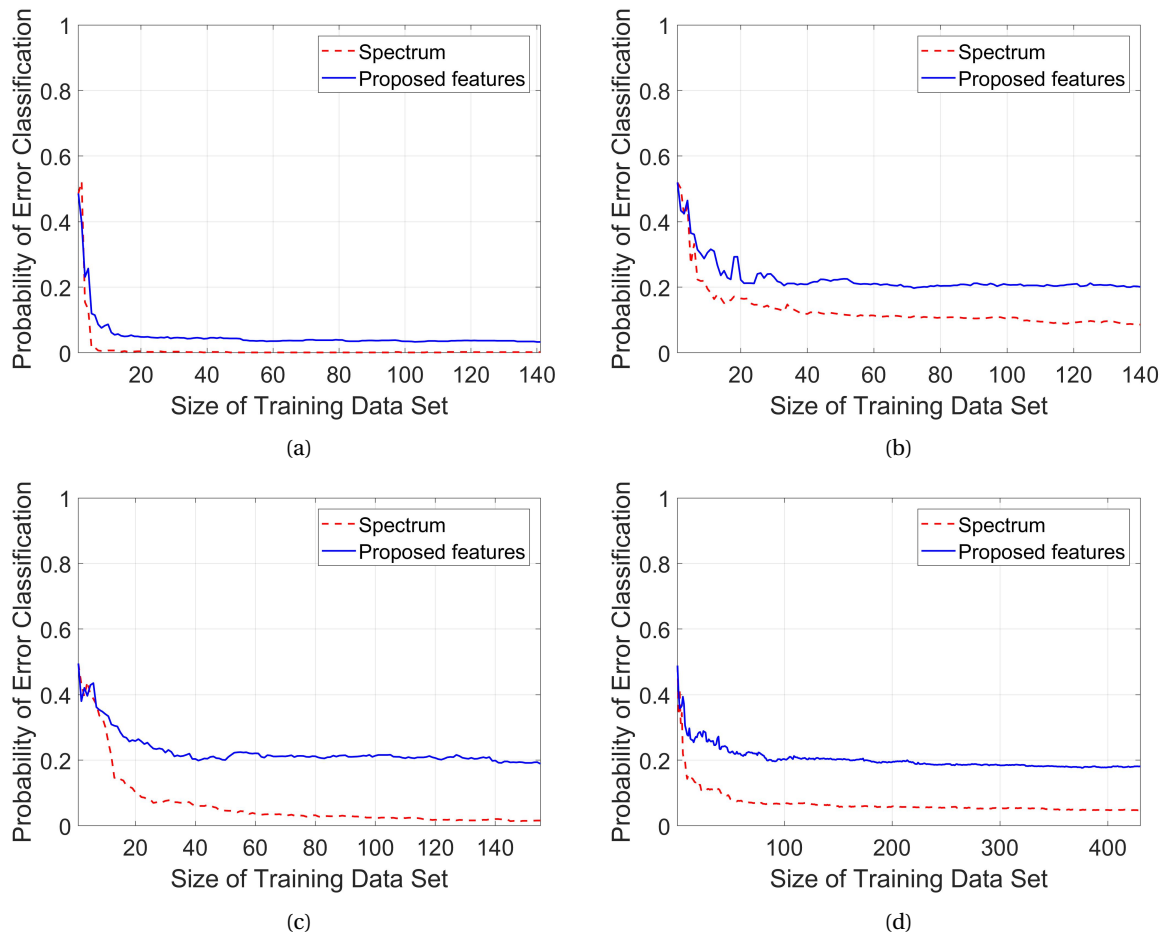
Figure 5.9: The classification error probability as function of training dataset size for the real observation data. Experimental scenarios: (a) Hovering scenario, (b) Along range maneuvering scenario, (c) Cross range maneuvering scenario, (d) Mixed scenario

5.4. Summary

In this chapter, the above proposed feature extraction and drone classification method are applied to the real data of the drone micro-Doppler pattern.

First, the setups of the real measurement of the EM reflection from two drones, the quadcopter DJI M200 and the hexacopter DJI M600 by the PARSAX radar system in the open air at the distance of about 9 km are introduced. There are 3 experiment scenarios performed for each drone, the hovering scenario, the along range maneuvering scenario and the cross range maneuvering scenario.

Then the measured data is processed, in order to prepare suitable data set for the further drone classification. The drone is detected in a range cell as each time point of a single CPI and tracked in the along range maneuvering scenario, based on its range-Doppler images over time. The drone micro-Doppler patterns in the observations are extracted from the appropriate range cells. Feature extraction and drone classification are performed to the observation data sets, similar to the processing in previous chapters. Good classification accuracy is achieved for the hovering, cross range maneuvering, along range maneuvering and mixed scenarios, validating the proposed features in general. However, the proposed features characterise the micro-Doppler spectra best in the hovering scenario. In the maneuvering scenario, due to the acceleration and the loss of the linear shape of the micro-Doppler pattern, the proposed features do not offer so good classification results.

6

Conclusion

6.1. Results and significance

Several results corresponding to the multi-propeller drone classification based on micro-Doppler patterns are achieved from this work. These results help in a) the development of a flexible model for drone micro-Doppler pattern data collection, b) the characterisation and feature proposal of drone micro-Doppler pattern in long CPI circumstances, and c) the drone classification under real conditions at large range with different flight attitudes.

A thin-wire model is developed for the EM signal backscattered from a multi-propeller drone – A new kit to generate a large number of drone micro-Doppler patterns, flexibly taking multiple variables into consideration and efficiently performing the simulation in seconds. The thin-wire model generates the HH polarimetric reflection signal of the drone, given the radar centre frequency, sampling frequency, propeller property, drone geometry structure design and drone flight attitude, from which the drone's micro-Doppler pattern can be achieved by Doppler processing. The thin-wire model is validated in the bandwidth from X-band to S-band, in terms on micro-Doppler pattern, by experiments in EM anechoic chamber, simulation in electromagnetic software and experiments in the open air.

The influence of various factors on the final micro-Doppler patterns in the long CPI circumstance is analysed, and related features are proposed characterising the drone micro-Doppler pattern – An exploration of drone micro-Doppler feature selection in long CPI field. Concentrating on the drone itself, the geometry structure design of the drone, the number of propellers, the number and length of blades per propeller, and the synchronisation of the propellers in rotation angle and angular velocity together influence the drone's micro-Doppler spectra in terms of the frequency where the spectra peaks appear and the normalised dB power of the peaks. Corresponding to the above influence, statistics features and frequency features are pro-

73

posed for the drone micro-Doppler pattern. These feature well characterise the original drone variables and their influence reflected on the drone micro-Doppler pattern.

The classification on the real data of drones in various flight attitudes measured in the far open air shows good performance – An expansion of micro-Doppler-based drone classification from ideal short range non-dynamic scenarios to large range dynamic scenarios. By applying preliminary processing of target detection, background filtering and pattern enhancement to the real data of drones measured by X-band radar system at several km, the proposed as above features together with SVM classifiers give good classification accuracy of more than 90% in hovering and maneuvering scenarios. This is a good starting point and demonstrates the feasibility to develop more advanced drone classification procedures for real world scenarios.

6.2. Shortcomings

There are many shortcomings in this work, such as the rough simplification and assumptions. Several short-comings are introduced in detail in this section, correspondingly related to the model development, the simulation and experiments, and the implementation of data processing and drone classifications.

The thin-wire model of multi-propeller drone is validated in X-band and S-band, but its validity in other frequency bands is not demonstrated. As the frequency increases, it is possible that the simple thin-wire structure does not well reproduce the real EM scattering phenomena take place on the drone and its propellers.

In the simulation and open air experiments, only the data achieved from the HH polarimetric channel is occupied for further processing, while the information contained in other polarimetric channels are totally lost. In some scenarios, especially when the drone is maneuvering or hovering at altitude off the horizontal plane where the radar antennas stay, the reflected signal received in the HH polarimetric channel decreases and much micro-Doppler pattern information is contained in the vertical polarimetric plane.

In the implementation of data processing and drone classification, only the most preliminary strategies are occupied. In more complicated scenarios or noisy environment, the performance of drone detection, tracking and classification based on these preliminary schemes may drop down.

6.3. Recommendations for future work

In order to improve the results from this work and eliminate the shortcomings, much work can be done in further researches. Several recommendations for future work are given as follows.

The thin-wire model can be developed to the horizontal plane, and be validated by indoor and outdoor experiments. By introducing roll and pitch degrees of freedom into the thin-wire model, the EM reflection from the multi-propeller drone in the vertical plane can be simulated as well. This further-developed model can be validated by outdoor experiments of drones continuously approaching the radar antennas along the LOS, or by indoor experiments of propellers fixed at specific attitude angles in the anechoic chamber.

The real propeller rotation velocity can be measured. In the simulation of drone micro-Doppler patterns, most of the model variables are set according to the specifics of real drones, but the angular rotation velocity

of drone propeller is assumed as a reasonable value, although this assumption does not contaminate the validity of the related analysis and conclusions. In order to measure the real propeller rotation speed, new measurements using staggered PRI modulation and other techniques can be performed with PARSAX radar system, to cover the possible drone micro-Doppler frequency from several hundreds to thousands Hz.

The data processing methods of drone tracking and background filtering can be improved. The histogram of the dB power of the drone micro-Doppler observation at each time point of a single CPI, as an alternative of the true PDF, is achieved from the open air measurement. Based on the histograms, several statistical detection and tracking techniques are available to better extract the data of drone micro-Doppler patterns.

The implementation of drone classification can be further investigated. As a demonstration of the validity and feasibility of proposed feature in real open air scenarios, the SVM classifiers used in this work are effective. However, from the rigor and performance point of view, better tuning the SVM classifier and the application of more classification schemes are worthy investigations.

Bibliography

[1] DUCAT layout. `http://radar.ewi.tudelft.nl/Facilities/ducat.php`, 2018. [Online; accessed 19-September-2018].

[2] DJI products. `https://www.dji.com`, 2018. [Online; accessed 13-September-2018].

[3] DJI Matrice 200 drone. User Manual. on-line `https://www.dji.com/nl/matrice-200-series`, 2019.

[4] DJI Matrice 600 drone. User Manual. on-line `https://www.dji.com/nl/matrice600`, 2019.

[5] PARSAX. on-line `http://radar.ewi.tudelft.nl/Facilities/parsax.php`, 2019.

[6] DJI R2170. `https://store.dji.com/product/2170-carbon-fiber-reinforced-folding-propeller-ccw-set`, 2019.

[7] DJI E 1200 propeller. CAD Model. on-line `https://grabcad.com/library/dji-e1200-folding-propeller-1`, 2019.

[8] Google Earth locations. PARSAX and Drone. on-line `https://earth.google.com/web/@52.01797957,4.31368301,-0.09081941a,15012.46560444d,35y,-0h,0t,0r`, 2019.

[9] Constantine A Balanis. *Antenna theory: analysis and design*. John wiley & sons, 2016.

[10] Svante Björklund. Target detection and classification of small drones by boosting on radar micro-doppler. In *2018 15th European Radar Conference (EuRAD)*, pages 182–185. IEEE, 2018.

[11] Svante Björklund, Henrik Petersson, and Gustaf Hendeby. Features for micro-doppler based activity classification. *IET radar, sonar & navigation*, 9(9):1181–1187, 2015.

[12] Victor C Chen, Fayin Li, S-S Ho, and Harry Wechsler. Micro-doppler effect in radar: phenomenon, model, and simulation study. *IEEE Transactions on Aerospace and electronic systems*, 42(1):2–21, 2006.

[13] Jacco J M De Wit, Ronny I A Harmanny, and Pavlo Molchanov. Radar micro-doppler feature extraction using the singular value decomposition. In *2014 International Radar Conference*, pages 1–6. IEEE, 2014.

[14] Jerry Eaves and Edward Reedy. *Principles of modern radar*. Springer Science & Business Media, 2012.

[15] Fulvio Gini and Muralidhar Rangaswamy. *Knowledge based radar detection, tracking and classification*, volume 52. John Wiley & Sons, 2008.

[16] Byung Kwan Kim, Hyun-Seong Kang, and Seong-Ook Park. Drone classification using convolutional neural networks with merged doppler images. *IEEE Geoscience and Remote Sensing Letters*, 14(1):38–42, 2017.

[17] Youngwook Kim and Hao Ling. Human activity classification based on micro-doppler signatures using a support vector machine. *IEEE Transactions on Geoscience and Remote Sensing*, 47(5):1328–1337, 2009.

[18] Oleg A Krasnov and Alexander G Yarovoy. Radar micro-doppler of wind turbines: simulation and analysis using rotating linear wire structures. *International Journal of Microwave and Wireless Technologies*, 7(3-4):459–467, 2015.

[19] Oleg A Krasnov, Leo P Ligthart, Zhijian Li, Pidio Lys, and Fred van der Zwan. The parsax-full polarimetric fmcw radar with dual-orthogonal signals. In *2008 European Radar Conference*, pages 84–87. IEEE, 2008.

[20] Bassem R. Mahafza. *Radar Systems Analysis and Design Using MATLAB Second Edition*. Chapman and Hall/CRC, 2005.

[21] Beom-Seok Oh, Xin Guo, Fangyuan Wan, Kar-Ann Toh, and Zhiping Lin. Micro-doppler mini-uav classification using empirical-mode decomposition features. *IEEE Geoscience and Remote Sensing Letters*, 15 (2):227–231, 2018.

[22] Alan V. Oppenheim, Alan S. Willsky, and S. Nawab. Signals and systems. 1996.

[23] Jarez S Patel, Francesco Fioranelli, and David Anderson. Review of radar classification and rcs characterisation techniques for small uavs ordrones. *IET Radar, Sonar & Navigation*, 12(9):911–919, 2018.

[24] S Pisa, E Piuzzi, E Pittella, P Lombardo, A Genovese, D Bloisi, D Nardi, P d'Atanasio, and A Zambotti. Numerical and experimental evaluation of the radar cross section of a drone. In *2018 15th European Radar Conference (EuRAD)*, pages 309–312. IEEE, 2018.

[25] Nir Regev, Ilia Yoffe, and Dov Wulich. Classification of single and multi propelled miniature drones using multilayer perceptron artificial neural network. 2017.

[26] Mark A Richards, Jim Scheer, William A Holm, and William L Melvin. *Principles of modern radar*. Citeseer, 2010.

[27] Matthew Ritchie, Francesco Fioranelli, Hugh Griffiths, and Borge Torvik. Micro-drone rcs analysis. In *2015 IEEE Radar Conference*, pages 452–456. IEEE, 2015.

[28] Merrill I. Skolnik. Introduction to radar systems. *New York, McGraw Hill Book Co., 1980. 590 p.*, 1980.

[29] Peter J Speirs, Arne Schröder, Matthias Renker, Peter Wellig, and Axel Murk. Comparisons between simulated and measured x-band signatures of quad-, hexa-and octocopters. In *2018 15th European Radar Conference (EuRAD)*, pages 325–328. IEEE, 2018.

[30] Roger Tan, Hock Siong Lim, Adriaan B Smits, Ronny IA Harmanny, and Lorenzo Cifola. Improved micro-doppler features extraction using smoothed-pseudo wigner-ville distribution. In *2016 IEEE Region 10 Conference (TENCON)*, pages 730–733. IEEE, 2016.

[31] Pengfei Zhang, Le Yang, Gao Chen, and Gang Li. Classification of drones based on micro-doppler signatures with dual-band radar sensors. In *2017 Progress in Electromagnetics Research Symposium-Fall (PIERS-FALL)*, pages 638–643. IEEE, 2017.